THE APPLICATION OF TERRAIN CLASSIFICATION TECHNIQUES TO VISIBLE, NEAR INFRA-RED AND THERMAL INFRA-RED IMAGERY.

N.D.E. CUSTANCE.

ABSTRACT

The research presented in this thesis was sponsored by the Ministry of Technology and carried out in the Physics Department of Bedford College, University of London, under the supervision of Dr. E.S. Owen Jones. The work was concerned with the 'Physics' aspect of Remote Sensing of the terrain whilst parallel, co-ordinated research into the ground-related aspects of the project were investigated by a Research Student in the Geography Department and supervised by Professor M.M. Cole.

Photographic emulsions were used to sense the visible and near infra-red radiation reflected by the terrain and an infra-red line-scanner detected the longer wave infra-red (3.5 - 5.5μm) radiation emitted from the ground.

The research studied two particular aspects in detail; Data Acquisition and Data Analysis.

The investigations into data acquisition required an examination into the factors affecting the various types of radiation as well as equipment calibration procedures.

The analysis of the data obtained with cameras was treated quantitatively whilst the imagery derived from the line-scanner was of degraded quality and only visual interpretation techniques were applied.

The research carried out has made contributions in two areas. Firstly it has provided greater understanding of the manner in which remote sensing exercises should be undertaken in order to reduce experimental errors. Secondly, the difficulties associated with the analysis of remotely sensed data were studied and several useful unsupervised cluster analysis strategies have been proposed and investigated.

INDEX

1 INTRODUCTION

Remote Sensing was evolved during the second World War when reconnaissance/surveillance techniques were developed from straightforward aerial photography. In particular the use of colour and infra-red 'camouflage detection' films showed that a considerable amount of information relating to the terrain could be inferred from the photographs.

Little use was made of these techniques until the early 1960's, when the non-military benefits of these and other more recently developed systems such as infra-red thermal imaging and radar were appreciated. The primary areas of interest were then in agriculture and forestry although the subject now encompasses all aspects of the environment, with special reference to earth resources and pollution.

In general terms Remote Sensing refers to the remote monitoring of the earth, typical current projects being Weather Satellites, ERTS (Earth Resources Technology Satellite), Skylab, Skylark (the British remote sensing system based on sounding rockets), together with more than 160 different European experimental programmes (1).

The Ministry of Technology (later the Ministry of Aviation, Supply and currently the Ministry of Defence) instigated a remote sensing programme jointly with the Physics and Geography Departments of Bedford College (University of London). The study, which lasted three years from September 1970 until September 1973, was an investigation into remote sensing techniques using multi-spectral photography and thermal infra-red linescanner imagery, the main area of interest being in Queensland, Australia, with trials in Wales and Derbyshire beforehand.

The study was considered as a feasibility exercise, the methods of analysis and overall objectives being left to the research groups but were based primarily on the work carried out by previous workers in remote sensing (2).

The environment of Western Queensland, Australia, selected for study was the semi-arid desert near to the mineral deposits

exploited in the late 19th and early 20th centuries to the east of Mount Isa and close to Mary Kathleen and Cloncurry. Two areas were delineated for the project, totalling some 1800 square kilometres, consisting in the main of land completely unaffected by man and with sparse vegetation. However, the vegetation although sparse was changed when different moisture conditions, soil and rock types were encountered. Similarly the presence or absence of mineralisation at or near to the earth's surface influenced the vegetation in several ways. High levels of mineral deficiencies led to the vegetation being stunted or even to only the survival of hardier species, whilst more moderate deficiencies only became similarly apparent when the environment was particularly harsh, e.g. in a year of relatively low rainfall. Toxic levels of minerals tended to favour the more hardy species but above a certain concentration the background plants did not survive and completely different plants grew. These latter plants are referred to as 'indicators', a term which is also applied to those plants which change their colours when subjected to different mineral levels (3).

The project workload was arranged such that in Spring/Summer 1971 when the team went to Australia and the imagery was obtained, the Geography group (4 persons) undertook the bulk of the ground truth work whilst the Physics group (2 persons) attended to the calibration of the imagery.

The Geography Department ground truth programme was centered on regions selected because of their geobotanical features and, in particular, on anomalous areas of vegetation occurring as a result of toxic mineral levels. Vegetational, geological and soil analyses were carried out along a transect line which in most cases intersected at right angles the 'strike' of the narrow mineralised region whilst a vegetation/surface soils map of the immediate areas (1,000 x 1,000m.) was also sketched out. The ground truth programme was continued in 1972, when the Geography group checked out geobotanical features tentatively identified on the processed imagery.

The multi-spectral photography, using four 70 mm. cameras containing true colour, 'false' colour infra-red, and two filtered black-and-white films, together with the thermal infra-red linescanner imagery

was obtained under contract with Fairey Surveys Ltd., of Maidenhead, Berkshire. Processing of the infra-red linescan imagery was sub-contracted to E.M.I. Ltd., who also provided the equipment and operator.

The infra-red linescan imagery was of low quality and only qualitative analysis was eventually undertaken. Several frames of the photographic imagery were digitised with a Joyce Loebl Microdensitometer (later updated to the Autodensidater version) and a cluster analysis approach was used to process the data. This method, which did not require a priori information relating to the terrain, was chosen after considerable difficulties were encountered in attempting to relate particular data sets to specific ground truth features.

Cluster analysis techniques have not been commonly used in the field of remote sensing where supervised learning routines appeared to be an almost standard procedure. However, the approach and modifications evolved during the study offered several advantages over the accepted methods although the real-time analsyis of the bulk data was not achieved. Nevertheless the analysis techniques were developed to a level of acceptability as a viable approach and several areas of interest in which further research is required were revealed. A section of the thesis devoted to suggested further work is included.

References

(1) E.S.R.O. : Directory of European activities in the Remote Sensing of earth resources. Neuilly, 1973.

(2) See 'Proceedings of the symposia on remote sensing of the environment' , Ann Arbor, Michigan.

(3) PETERSON : Science Progress, 59, 505, 1971

2 FIELD AND LABORATORY PROGRAMMES THROUGHOUT THE STUDY

2.1 Activities Prior to the Australian Field Study

The formal commencement of the project in September 1970 coincided with the completion of a pilot flying programme carried out by Fairey Surveys Ltd., over areas in Derbyshire and Mid-Wales. The survey used an EMI 'Airscan' infra-red linescanner and a multi-spectral camera package, its purpose being to determine the operational characteristics of the instrumentation prior to the Australian study.

The infra-red linescanner used a cooled indium antimonide detector sensitive to the 3.5 - 5.5 micron waveband, the output from the detector being recorded on a video tape-recorder. Operation of the linescanner was accompanied by that of the multi-spectral camera package comprising four Vinten F 95, 10.2 cm. (4 inch) focal length electrically operated cameras, fired simultaneously, each with cassettes holding 33 metres of 70 mm. film giving approximately 400 frames without reloading. The films, filters and other related data are shown in Table 2.1 whilst Figures 2.1 and 2.2 show the sensitivity of the false-colour film and the dye transmission factors for the two colour films respectively. The processed infra-red linescan data together with the multi-spectral imagery in the form of either colour transparencies or black and white negatives was then examined in order to define the operational requirements for the Australian exercise. These observations and the resultant recommendations are summarised below.

(i) Infra-Red Linescanner (See figure3.5 for example)

The spatial resolution of the system was within the predicted limits as both the limestone walls about 0.5 metres wide and the tracks made by herds of animals passing through the gates between fields could be clearly seen. (The altitude of the aircraft above the ground was approximately 1,200 metres (4,000 ft.) and thus a system resolution of 1.5 milli-radians would imply resolution of objects on the ground about 1.8 metres in diameter).

TABLE 2.1 The films, their characteristics and the filters used

FILM TYPE	RELATIVE SPEED	RESOLUTION (Lines/mm. for a 1.6:1 contrast target)	FILTER/S USED (Wratten numbers)
Ilford PAN F+	64	63	12 and 58
Kodak TRI X+	64	63	12 and 58
Kodak EKTACHROME AEROGRAPHIC (8442 & 2448)+	32	40	1A
Kodak AEROCHROME INFRA-RED (8443 & 2443)+	40	32	12

+U.K. Pilot study TRI X, 8442 and 8443

Australian PAN F, 2448 and 2443

The changes were the result of film availability in the case of TRI-X and changes in the film bases of 8442 and 8443.

In some areas the imagery showed phenomena such as large scale textural patterns which extended over many fields and were believed to be due to variations in surface/sub-surface soil moisture levels. However, no temperature readings were available to indicate the thermal resolution of the system.

By far the most dominant parameter seen on the imagery was terrain relief. This resulted from solar radiation being both reflected and re-emitted (after absorption) by the terrain facing the sun, thereby giving it a pronounced topographic-type appearance.

In order to reduce the effects of terrain relief to a minimum, operation of the linescanner was requested for night-time and, preferably, just prior to dawn. A 4.5 - 5.5 micron band-pass filter was fitted so that any post-dawn imagery that might be obtained as a result of prolonged flying periods would contain solar heating effects rather than reflected solar radiation (see Section 4.1).

(ii) Panchromatic TRI-X Films

This, as with the other three films, exhibited surface blemishes due to careless handling but, more importantly, the overall densities of the films varied due to either different exposure or development times. This latter fault was rectified by the insertion of step wedges at the start of each spool. Development times of 8 minutes at 70°F with full strength Kodak D19 developer were chosen as they produced a gamma value between 1.2 and 1.4, this being normally considered necessary for aerial photography.

(iii) False-Colour Infra-Red Film (Type 8443)

The intensity of reds throughout the imagery appeared near saturation level and test exposures would need to be taken in Australia before routine photography was commenced. The susceptibility of the false-colour film to variations in solar radiation intensity resulted in the hours between which photography was possible without changes in aperture being from 10.00 to 14.00 local time. Uneven development resulted in colour distortions on a few frames. This is discussed below.

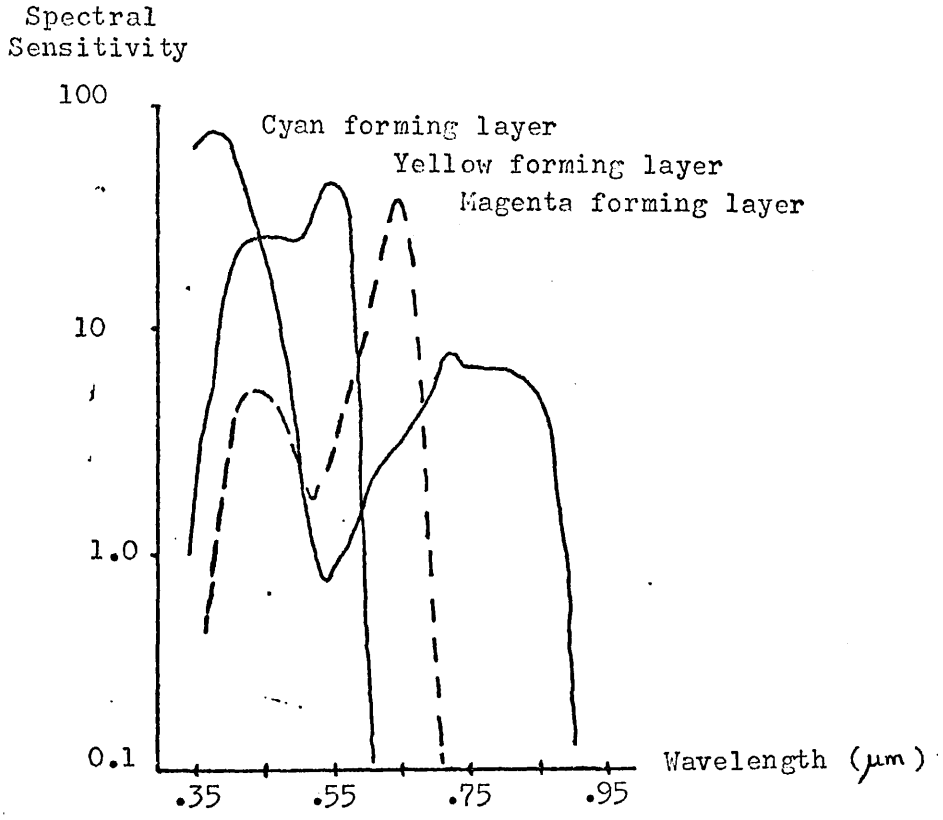

FIGURE 2.1 SHOWING THE SPECTRAL SENSITIVITY OF THE "FALSE COLOUR" INFRA-RED FILM LAYERS

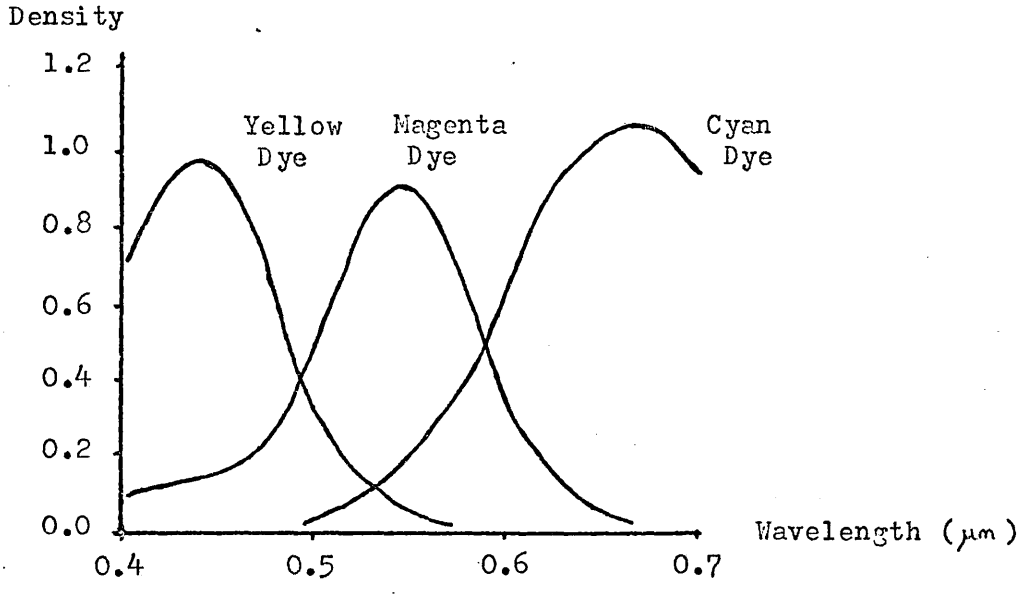

FIGURE 2.2 SHOWING THE DYE LAYER SPECTRAL DENSITY CURVES FOR KODAK COLOUR FILM EMULSIONS

(iv) True Colour film (Type 8442)

The transparencies were very thin (i.e. lacking density) and consequently had generally low contrast due to the failure to use the 1A haze filter which had been specified. Distortions of the colours within a few frames were also seen and were due to the rewind method of development. This effect, also present on the false-colour film, was subsequently rectified by the use of a spiral development method. The development times and temperatures of the films were to be within $\pm$ 10 seconds and $\pm$ 0.5°F respectively.

(v) The general requirements for the photography were for the areas concerned to be flown such that adjacent flight lines resulted in no lateral overlap of the imagery but with a 60% forward overlap on consecutive frames to allow stereoscopic viewing.

The stringent requirements placed on the processing of the colour films required that they be returned to England where equipment of sufficiently high precision existed and only the TRI-X film with the yellow filter and the infra-red linescan data were processed in the field. In both cases this was done primarily to ascertain that complete coverage of the flying blocks had been obtained.

The direction of view of each of the cameras was slightly different and re-alignment by the contractors of the camera mountings was undertaken.

The conclusions drawn from the pilot exercise were that the imagery had shown variations in the systems which could not be tolerated if quantitative measurements were to form the basis of any analysis. Although the above recommendations should have eliminated or at least greatly reduced some of these variations, external calibrations of the imagery would nevertheless be required, not only to check the performance of the systems but also to enable corrections to be made for any errors which might inadvertently arise. It was then possible to make density scans on the Derbyshire imagery and to investigate different analysis techniques prior to the collection of the large amount of imagery in Australia.

One particular frame (number 147 Derbyshire) was chosen which contained several different field types and it was scanned using a Joyce Loebl Microdensitometer Mk III CS (1). The data content of the density scan was however too high for manual extraction from the graphical output and, in order to digitise the data, a potentiometer was fitted to enable a voltage proportional to the position of the graph-pen to be obtained.

2.2 The Australian Field Programme

Calibration of the infra-red linescanner was considered essential and a grass oval and a swimming pool in a recreation complex at Mt. Isa, the town at which the survey aircraft was based, were of appropriate dimensions for calibration targets. The photographic system was more difficult to calibrate as, during a given sortie, the film cassettes would need to be changed and thus the placing of any colour targets at (for example) the airport would be ruled out. Consequently it was decided to use portable calibration boards which would be moved along tracks within the areas being photographed so as to intercept the path of the aircraft. As each film cassette would suffice for at least two flight lines the boards would appear once or possibly twice on each film. Calibration targets were constructed of hardboard sheets each 2m. x 1.3m. (6' x 4') with 4 or 6 boards for each of the colours, red, green, blue, white and a grey, representative of the spectrum of the films. Additionally light grey, dark grey and Dayglow plastic sheetings were obtained and are detailed below.

Extensive logistic support was provided by the Bureau of Mineral Resources and accommodation at Mary Kathleen was arranged by courtesy of Consolidated Zinc Rio Tinto Associates.

The final set of moveable calibration targets was as follows:-

Blue: (3.9 x 3.9) m (12' x 12') array of boards:
British Paints Ltd., Nu-Plastic Velvet Flat

Red: (3.9 x 2.6) m (12' x 8') array of boards:
Glowmaster Fluorescent

Dayglow (3.9 x 1.6) m (12' x 5') canvas backed canopy

Light-Grey: GY0283 50/2/26 3 off (3.9 x 1.3) m (12' x 4')
Plastic sheeting, Nylex Corporation Ltd.

Dark-Grey: GY0314 50/2/26 3 off (3.9 x 1.3) m (12' x 4')
Plastic sheeting, Nylex Corporation Ltd.

The areas delineated for study and denoted by A, B, and C in figures 4.10 and 4.31 were reconnoitred with regard to the accessibility of the regions of interest, and for the purpose of locating tracks suitable for laying down calibration boards. Since the flight lines would run N - S in Blocks A and B and E - W in Block C, the tracks needed to be E - W and N - S respectively. The nominal flying altitude for Block A was 980m.(3,000 ft., 1:5,000 scale) and for Blocks B and C, 1,900m.(5,850ft., 1:15,000 scale). Consequently a camera field of view of $\pm$ 20° from the nadir resulted in a line spacing for adjacent flight lines of 275m. (0.17 miles) for Block A and 800m. (0.5 miles) for Blocks B and C. Suitable tracks were located and mapped.

The temperature of the top four millimetres of the water in the swimming pool was sampled at 10 points over its surface and readings within $\pm$ 0.1°C of each other indicated that the water was being adequately circulated. The size and temperature uniformity of the pool made it suitable as a linescan calibration target as did four adjacent tennis courts with concrete surfaces. The grass oval was large enough to satisfy the spatial requirements for a calibration target but the intermittent and partial watering of it carried out at 08.00 could have produced temperature differences due to different levels of moisture. Test readings were therefore taken of the grass and the surface layer of ground between 06.30 and 08.30, the times between which the aircraft was expected to be flying, and the variations found to be $\pm$ 1.5°C. This resulted in a decision to monitor the grass canopy and ground temperatures at three different locations.

The temperature of the concrete surface of the tennis courts was obtained by means of a calibrated thermistor embedded in a small quantity of "Bostik" sealer stuck to the surface. Table 2.2 shows the exceptionally heavy rainfall of February and March but, by

mid-April, targets were placed in the field to delineate areas on the imagery of particular interest. At the same time an additional set of calibration boards was prepared and laid down outside the main flying blocks so that it could be photographed as the aircraft was turning between successive flight-lines. This was done as a precaution lest the ground team could not position the moveable boards.

On 24th April two flights were made, at 07.30 and 10.30, to test the infra-red linescanner and multi-spectral camera arrays respectively. The former equipment developed an apparent fault which required the detector to be replaced and the system to be refocussed.

Navigational difficulties resulted in this and all subsequent linescanning activities taking place after first light and, as a consequence, the terrain underwent solar heating as the flight progressed.

Linescanning operations were carried out on 24th April to 4th May and 7th to 13th May whilst the multi-spectral photography took from 24th April to 24th May. Throughout the period of the operations the temperatures of the linescan calibration targets were continuously monitored from 06.30 to 08.20. The calibration boards were moved along the tracks for all blocks except A, where the separation of flight lines made the number of aborted attempts by the pilot and, consequently, the number of mis-located boards too great.

TABLE 2.2 Rainfall measurements in 100th's of inches from Mount Isa Airport for February, March and April 1971

DATE:	1	2	3	4	5	6	7	8	9	10	11	12	13	14	15
FEB:	0	0	0	21	0	0	48	0	90	74	0	0	0	0	0
MAR:	0	0	175	141	304	-	12	0	0	0	2	12	-	0	0
APR:	39	2	0	0	0	0	0	0	0	0	10	110	94	21	136

DATE:	16	17	18	19	20	21	22	23	24	25	26	27	28	29	30	31
FEB:	7	0	1	0	0	0	16	0	0	0	18	0	1			
MAR:	0	0	107	-	-	0	0	0	0	0	45	1	1	20	16	37
APR:	39	0	0	0	0	0	0	0	0	0	0	0	0	0	0	0

The readings from the linescan calibration targets showed that the rate of heating of the terrain would radically affect the thermal contrasts between objects on the ground. As a result a set of measurements over a 24 hour period was made in the field of the temperatures of typical targets to provide some data on the magnitude and rate of these effects.

2.3 Laboratory Programme from June 1971 to August 1973

The processing of all the imagery from Australia took about two months and, despite the precautions taken, some faults still occurred. The exposure of the false-colour film was uneven with a darker coloured band towards and parallel to the edge of quite a few frames. This was most probably due to an intermittent fault with the focal plane shutter mechanism. In addition to this areas of the frames appeared to be bleached out, bare areas of ground seeming to be white or completely transparent on the photography. Initially this was thought to have been caused by over-exposure but densitometric measurements on the film showed that the density variations within the infra-red sensitive emulsion layer were twice as great as those within the other layers and it was a lack of colour balance rather than incorrect exposure which caused the effect. There were also considerable differences between the test exposures made and developed in Australia and those of the same area processed in England, due no doubt to the particular sensitivity of the infra-red film to processing conditions.

A fault of greater consequence was the imperfectly focussed optics system of the infra-red linescanner. Although the data from the video-tape recorder was replayed in Australia to check the cover of the areas flown, it was not until enlarged copies were examined that the serious degradation of the system was appreciated. The degradation is clearly demonstrated in Figures 4.13 and 4.16 where imagery over Mt. Isa at 850 metres (2,600 ft.) above the ground is compared with that over Derbyshire at an altitude of 1700 metres (5,250 ft.) above the ground. The resolution was estimated to have degraded by a factor of about 5.

2.4 Analysis

Analysis of the photographic imagery was mainly quantitative whilst that of the linescan was more easily performed qualitatively because of the distortion due to the constant angular velocity of

the scanning mirror, the method of replay and the lack of resolution.

Two other projects allied to Remote Sensing were engaged upon during the analysis period; one involved the quantitative analysis of Skylark Rocket imagery over Australia and Argentina whilst the other investigated the effects of phosphate deficiencies on tree growth vigour in conjunction with the Forestry Commission.

The quantitative analysis of the imagery formed the basis for the involvement of the physics discipline with the project and consequently the methods used are dealt with in some detail (See 2.5, also Chapters 6 and 7).

2.5 Densitometry

In order to extract the information content from a photograph, several methods such as television cameras, Agfa Contour 'Equi-density film', flying spot scanners and microdensitometers can be used. A Joyce Loebl Mk III CS microdensitometer (1) had been chosen on the basis of cost and performance whilst the 'feasibility study' nature of the project justified this relatively slow method of digitisation of the imagery.

Modifications were made to the instrument which allowed the single scan made across a specimen to be digitised. Both the density reading and its position on the specimen were sampled; alternate density and position readings were digitised and stored in a 400 channel analyser before being output on paper tape.

Further modifications, carried out by Joyce Loebl Ltd., in 1973 permitted the raster scanning of specimens, the density readings being directly punched on to paper tape.

2.6 Sampling criteria and procedures

Sampling theory shows that for a given signal to be sampled satisfactorily the sampling frequency needs to be greater than

or equal to twice that of the highest signal frequency; this is referred to as the Nyquist criterion.

In relation to the scanning of photographs, the frequency concept is replaced by one of dimensions; the criterion demanding that for objects with a diameter d, an aperture with diameter D which is stepped across the scene containing the object, so that consecutive samples are adjacent, must be such that $D = {}^{d}/_{2}$. This is illustrated in Figure 2.3 to Figure 2.6.

Thus for all apertures greater than d the output is less than that of the object as the dark object is sampled along with a portion of the lighter background. For an aperture equal to d (2.5) there is a unique position when the output equals that of the object. Since the aperture is stepped across the scene such that each area sampled is adjacent to the preceeding one, the chances of the aperture centre being at the unique position are small. When the aperture is of diameter d/2 (2.6) its centre need only fall within $\pm$ d/4 of the centre of the object for an output signal equal to the input to be obtained. But, as $\pm$ d/4 is equal to the distance stepped between successive samples, there must be one 'true' sample and possibly two, should the first sample centre be at - d/2.

Although the above discussion considered object and aperture diameters in one dimension the same agrument can be applied to square apertures scanning a two dimensional image, the diameter being equivalent to the length of the square area sampled.

This criterion forms a basis for the sampling procedure outlined below which sets out the manner in which a line on a photograph was scanned.

(i) A line across the frame of interest was chosen.

(ii) The diameter of the smallest feature revelant to the study was determined and the aperture set equal to one half of it.

(iii) The frame was aligned so that the desired line is scanned and a distinctive feature was chosen to mark the start of the scan.

Fig 2.3

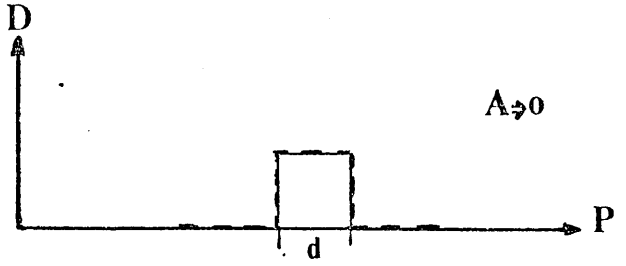

Fig 2.4

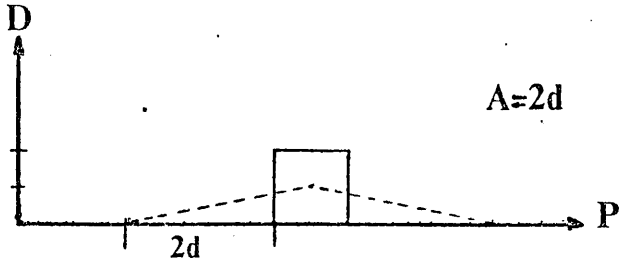

Fig 2.5

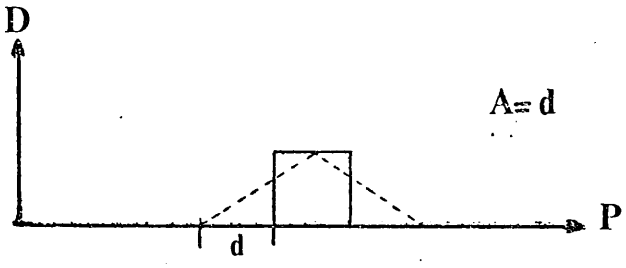

Fig 2.6

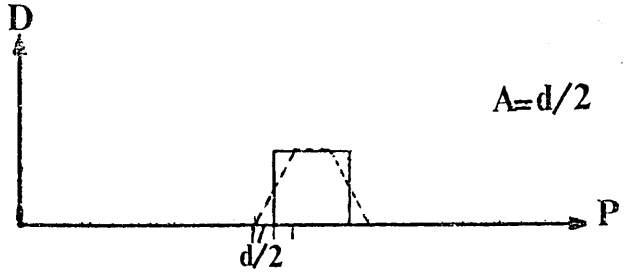

Figures 2.3 to 2.6 Showing the apparent density (D) of an object with diameter d as sampled by an aperature of diameter A centered at P. Sampled density shown dotted.

(iv) The ratio arm, colour separation filter, density biases and wedges were optimised for the scan.

(v) The scene was scanned and the speed of the table adjusted using the potentiometer so as to retain the fine detail of the scan.

(vi) The sampling rate of the pulser was set so that consecutive samples were adjacent on the photograph (i.e. 200 scanning aperture diameters = length of scan travelled in time to digitise 200 density readings).

(vii) The line was scanned and the data stored.

(viii) The stored data was ouput on to paper tape.

(ix) All the variables associated with the system were measured so as to enable the scan to be calibrated.

(x) The next colour separation filter was inserted and the process repeated from step (vii) after changes of biases and wedges etc., were made.

The procedure was time consuming in that it took about 2½ hours to produce a complete set of 8 scans, i.e. 2 black and white films and the three emulsion layers of each colour film.

Each of the eight scans was different, not only because of the different reflectance of the objects photographed, but also as a result of each of the scans starting and finishing at slightly displaced points or the table moving at a different speed. (Although for a given scan the speed was uniform to within the resolution of the system). The part of the eight scans common to each was found by comparison of lineprinter fascimilies of the digitised scans, the first and last points noted in the form of density reading and position reading and the scan/card identified and this information punched on to a single card for each scan.

The data, together with the above mentioned card and a calibration card, were fed into the computer along with a programme which

extracted the common scans, calibrated them and stored the revised data on magnetic tape along with appropriate identification.

The analysis of the calibrated data formed the bulk of the laboratory work from July 1970 onwards and is discussed theoretically in Chapter 6 with the results presented in Chapter 7.

2.7 References

(1) Supplied by JOYCE LOEBL LTD., TEAM VALLEY, GATESHEAD-ON-TYNE.

3 THEORETICAL CONSIDERATION OF THE THERMALLY EMITTED INFRA-RED RADIATION FROM THE TERRAIN

3.1 Introduction

A fundamental property of matter is that it emits electromagnetic radiation with wavelength in the region of 0.1 to 50 microns (μm), the intensity of the radiation being a function of the absolute temperature of the matter.

This radiation is termed infra-red radiation and, for a given body, the total amount of energy radiated per square metre was related by Stefan to its absolute temperature by the equation:

$$W = \sigma T^4 \qquad 3.1$$

Where: The body is a black-body
T is the absolute temperature of the body in ^{o}K
σ is Stefan's constant $(5.7 \times 10^{-8}\ W.m^{-2}.{}^{o}K^{-4})$

Planck showed that at a wavelength λ the spectral emittance (W_λ, power radiated per unit area per unit wavelength) of a black body could be described by the equation:

$$W_\lambda = \frac{c_1}{\lambda^5} \cdot \frac{1}{(e^{c_2/\lambda T} - 1)} \qquad 3.2$$

Where: $c_1 = 3.74 \times 10^{8}\ W.m^2$
$c_2 = 1438\ m.{}^{o}K$

The emitted radiation obeys Lambert law, thus the radiance of a surface is independent of angle.

Figure 3.1 shows W_λ plotted against λ for temperatures typical of a terrestial environment. At a given temperature the maximum amount of radiation occurs at wavelength λ_{max} which is obtained from equation 3.2 and is of the form:

$$\lambda_{max} = \frac{2897}{T} \ (\mu m) \qquad 3.3$$

FIGURE 3.1 SHOWING THE VARIATION OF SPECTRAL RADIANCE WITH WAVELENGTH FOR A BLACK-BODY AT TYPICAL TERRESTIAL TEMPERATURES.

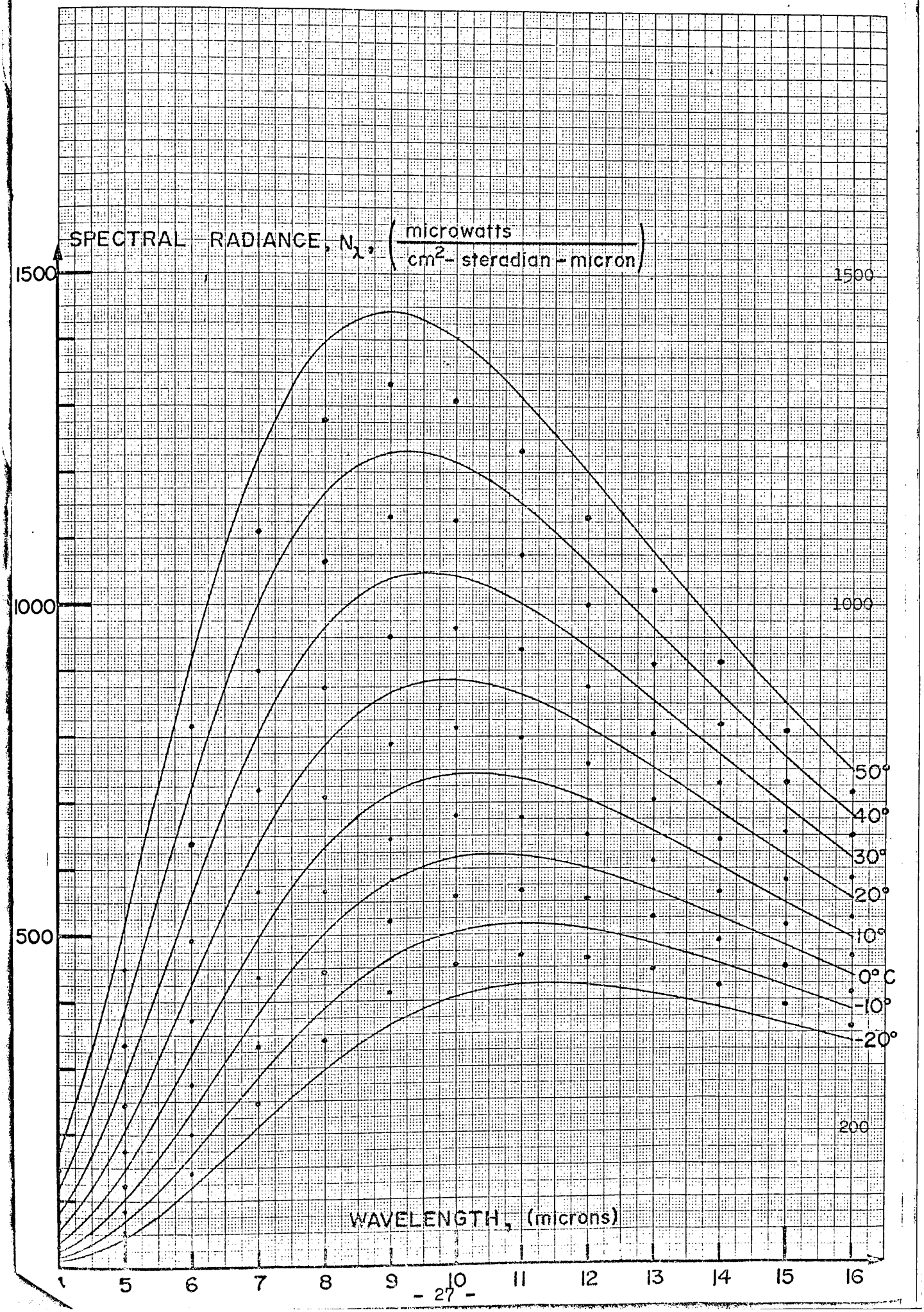

Equation 3.3 is referred to as Wien's displacement law.

It is shown later (section 3.2) that the temperature of a natural object is not directly related to its reflectance properties and, as a consequence, the information obtained from "measuring" its effective radiant temperature (indirectly by monitoring the amount of infra-red radiation emitted by it) can be used for identifying it either directly or in conjunction with observations in other regions of the electromagnetic spectrum.

3.1.1 The Solar Radiation Spectrum

The spectral radiation distribution from the sun, outside the atmosphere, at sea level and for a black body at 6,000°K are shown in Figure 3.2 (1) together with the absorption spectra of the major constituents which account for the transmission characteristics of the atmosphere, Figure 3.3 (1).

Comparison of Figures 3.1 and 3.3 shows that up to 3 microns the amount of reflected solar radiation (even from a terrestial object with a reflectance coefficient of 10%) will dominate over that radiated by the ground, and as a consequence any radiation measurements to be related entirely to the temperature of the terrain must be made at wavelengths greater than $\sim$ 3.5 μm.

The total absorption spectrum of the atmosphere (Figure 3.3) has resulted in two bands, 3.5 - 5.5 μm and 8.0 - 14.0 μm being commonly employed for infra-red devices. However, the variation in the concentration of water vapour in the atmosphere can radically affect the transmission in the 3.5 - 5.5 μm band (see 4.2.2).

3.2 Infra-Red Detectors

The range of infra-red detectors commonly available, together with their spectral detectivities is shown in Figure 3.4 (2). Two materials are in common use, Indium Antimonide (InSb) which op-

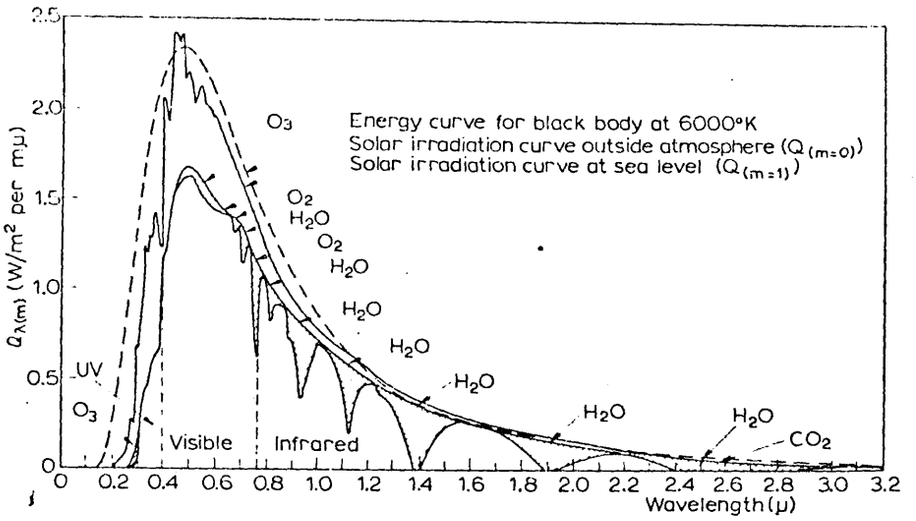

Fig. 3.2 Solar spectrum outside the atmosphere (m 0) compared with that of a black body at 6000 K and at sea level (m 1) (*Handbook of Geophysics*, Revised edition, U.S. Air Force, Macmillan, New York, 1960).

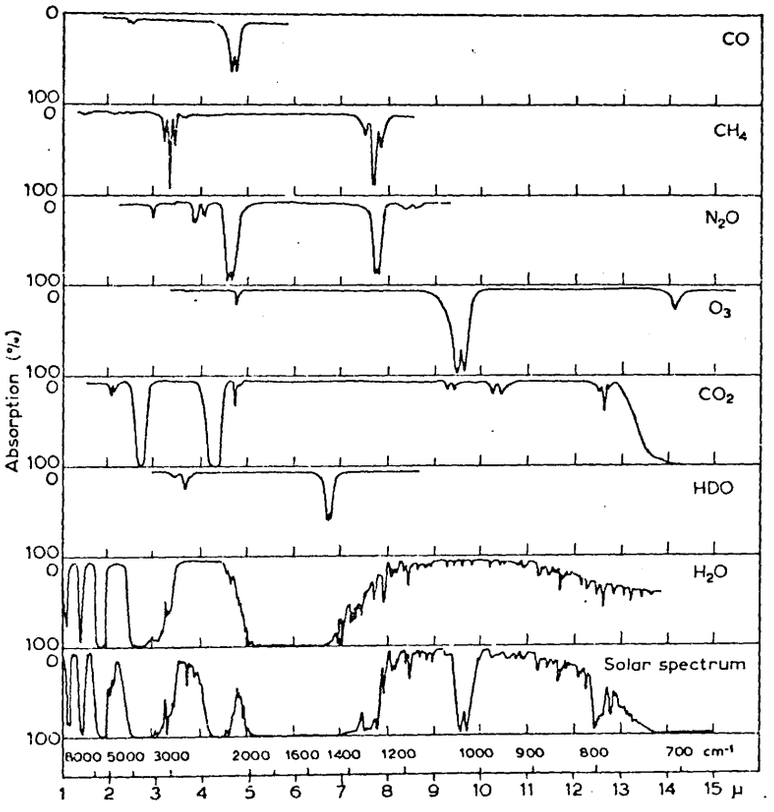

Fig. 3.3 Near-infrared solar spectrum compared with the absorption spectra of CO, CH_4, N_2O, O_3, CO_2, HDO and H_2O [53].

erates most efficiently at 77° K with a useful spectral response from 3.0 - 5.5 μm and, operating at the same temperature but over the range 8.0 - 14 μm, Cadmium Mercury Telluride (CdHeTe). The boiling point of liquid nitrogen is 77°K and it is a convenient detector coolant when used in a Lidenfrost liquid transfer system. However, precautions need to be taken to prevent the bubbling of coolant inducing spurious detector signals by microphonic effects.

3.3 Line Scanning Devices

The cost of fast-reacting infra-red sensitive detectors eliminates any kind of directly displayed airborne infra-red system. Slow-speed devices using arrays of tri-glycine sulphate detectors at room temperature connected to gallium phosphide lamps providing a 'picture' which can be cycled at a rate of 30 times per second are typical of the state-of-the art (3).

Currently, a commonly used method is for the field of view (F.O.V.) of a single detector to be swept laterally across a scene whilst forward movement of the sensing platform results in a raster type scan being created. The device is referred to as a linescanner and an object-space linescanner is shown pictorially in Figure 3.5.

The speed V of the sensing platform, assumed to be in a direction parallel to the ground plane, is related to the angular velocity, Ω, of the mirror and the F.O.V. of the detector, θ, by the requirement that consecutive swathes swept out by the F.O.V. be contiguous.

Let the detector be a distance H from the ground plane. Thus the diameter D of the detector field of view on the ground is:

$$D = H.\theta \qquad 3.4$$

Where typically units of H and D are metres and of θ are radians.

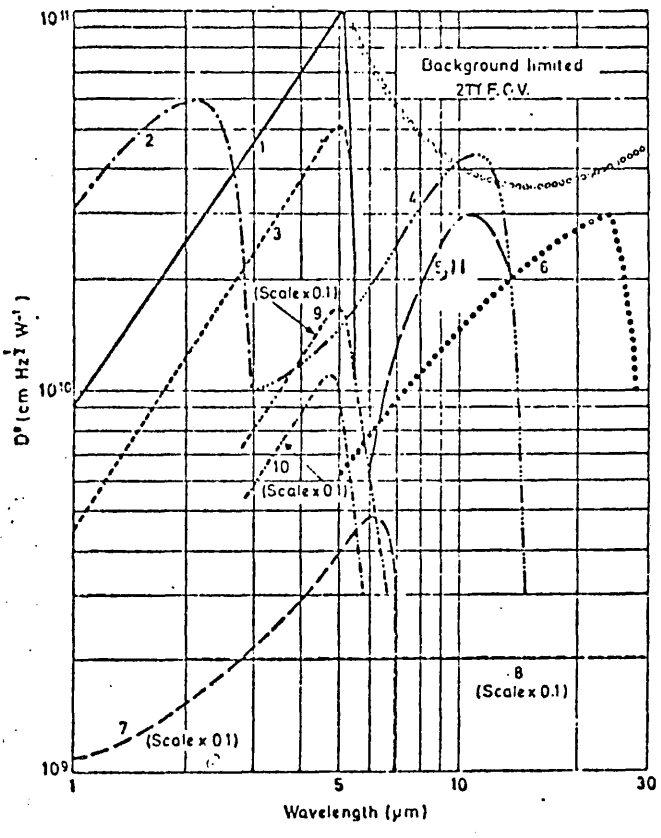

1)	InSb 77K, 60 ° FOV	6)	Ge: Cu 4·2K, 60 ° FOV
2)	Pbs 300K, 2π FOV	7)*	InSb 300K, 2π FOV
3)	InSb 77K, 2π FOV	8)*	TGS bolometer
4)	Cd Hg Te 77K, 60 ° FOV	9)*	Cd Hg Te -80 °C
5)	Ge: Hg 35K, 60 ° FOV	10)*	Cd Hg Te 295K
11)	PbSnTe 30°K 2π FOV	* scale ×0.1	

FIG3.4 TYPICAL DETECTOR SPECTRAL DETECTIVITIES

from:- Application of Infra Red Detectors
Mullard (with addition)

Figure 3.5 SHOWING THE PRINCIPLES OF LINE-SCANNERS (WITH INSERT SHOWING THE ASSOCIATED GEOMETRY)

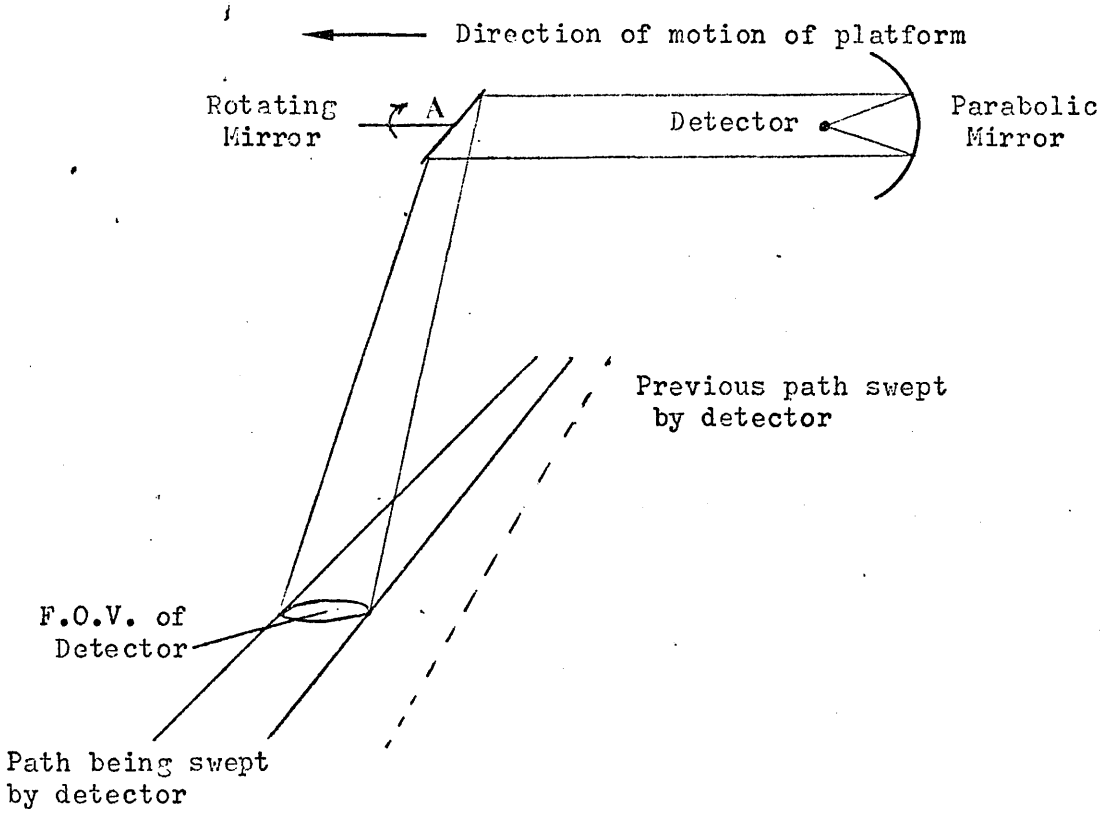

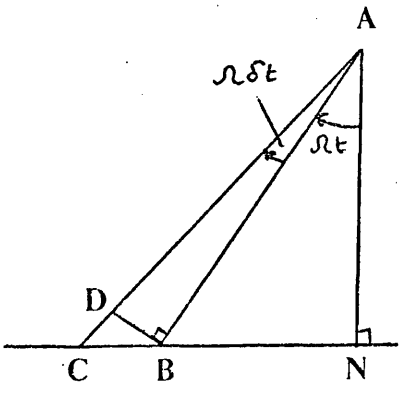

INSERT SHOWING SCANNING GEOMETRY

For consecutive detector swathes to be contiguous, after one revolution of the detector mirror, the platform is required to move D metres. Thus:

$$V = D \cdot \frac{\Omega}{2\pi} \qquad 3.5$$

Where V is in metres/sec.
Ω is in radians/sec.

Thus from 3.4 and 3.5

$$V = \frac{H.\theta.\Omega}{2\pi} \qquad 3.6$$

Typically, M = 1000 metres; $\theta = 1.5 \times 10^{-3}$ radians;

$\Omega = 100\pi$ radians/sec. $\therefore$ V = 75 m/sec.

The cross-track velocity of the F.O.V. of the detector is derived from Fig. 3.5

If the projected centre of the F.O.V. moves from B to C in time δt, where the angle BAN is Ωt radians, the following steps are easily derived;

$$AB = AN \text{ Sec. } (\Omega t)$$
$$\therefore BD = \Omega . \delta t . AN \text{ Sec } (\Omega t)$$
$$\text{But } A\hat{B}N = 90^{\circ} - \Omega t$$
$$\therefore DBC = \Omega t$$
$$\text{Hence } CB = BD \text{ Sec. } (\Omega t) \qquad 3.7$$
$$\text{Thus } \frac{CB}{\delta t} = \Omega H . \text{Sec}^2 (\Omega t)$$

$\frac{CB}{\delta t}$ is the cross track velocity of the F.O.V. of the detector on the ground plane and its non-linear variation with time causes considerable distortion with the conventional image reconstruction systems.

The relationship between V and H is usually fixed for a given linescanner but lower altitudes can be flown using multi-facetted mirrors or multi-bank detector arrays.

The operation of linescanners is not restricted to the thermal infra-red spectrum and multi-spectral devices scanning simultaneously in 12 wavebands are already in operation (4).

3.3.1 Restrictions on the Scanner Platform

Equation 3.6 demonstrated the relationship between V and H which is required for contiguous scanning. Consequently any variation in V, H, θ or Ω can produce distortions in the system. θ is a constant for a given detector but although Ω may be constant in the aircraft reference frame, aircraft roll will effectively alter Ω in the ground plane and consequently distort the scans. Similarly changes in aircraft pitch will alter V and H in the ground plane whilst aircraft yaw will also distort the image. The effect of aircraft yaw is shown in Chapter 4.

These effects can be overcome to some extent by stabilising the scanning platform in the pitch and roll axes whilst yaw and forward speed changes are corrected for on replay (see 3.5) by means of recorded in-flight data.

3.3.2 The Effects of Restricting the Waveband Sensed by the Detector

The spectral emittance at a wavelength λ was given by equation 4.2 as:

$$W_\lambda = \frac{c_1}{\lambda^5} \cdot \frac{1}{\left(e^{c_2/\lambda T} - 1\right)} \qquad 4.2$$

However, although the total radiated energy per unit area is related to the temperature of the body (assumed to be black) by:

$$W = \sigma T^4 \qquad 4.1$$

the relationship does not hold when a narrow waveband is sensed.

Numerical integration of 4.2 over three particular wavebands W_B enables the theoretical exponents of T, (X), to be determined and W_B to be expressed as $W_B \propto T^X$

W_B:	3.5 - 4.5 μm	4.5 - 5.5 μm	8 - 14 μm
X:	10.2	9.7	4.7

Further modifications are required to correct for the non-linear detector spectral response (see Figure 3.4) and the variation of emissivity with wavelength for the target being sensed (e.g. Figure 3.7 (6)). The latter effects can only be compensated for if the target composition is known whilst the detector response was found to be of considerably less significance than that caused by restricting the waveband sensed. Use of the variation of emissivity with waveband has been exploited by ratioing the detector output from two different infra-red wavebands and it appears that basic rock types can be classified (7).

3.4 Calibration of Linescanners

In general, multi-spectral scanners require at least three calibration inputs. One, applicable only to sensors operating below 3 μm is the solar radiation at the altitude of the sensor which gives an estimate of the radiation incident on the scene being scanned. The two other inputs are reference sources, representing the extremes of the radiation levels to be detected. The sources may be incorporated into the linescanner (e.g. two 'black-bodies' for I.R. or incandescent sources for visible sensors) but if this is not possible then ground plane references need to be used. Internal references are usually sensed when the detector is looking away from the ground plane.

3.5 Signal Recording, Processing and Replay

The signals from the detector are a function of the scene radiance and are normally recorded on film (see 3.6) or on to a video tape-

recorder in FM form which accommodates a considerably greater dynamic range of signals (~ 40dB). The recorded video signal is then available for replaying, digitisation etc. at a later date. Whichever form of recording is used, very little pre-processing of the signals is carried out except for the method of coupling signals to the recording media where A.C. or D.C. modes may be chosen. The benefit of A.C. coupling is to enable long term radiance variations - lasting the order of tenths of seconds - to be smoothed out, whilst retaining the full dynamic range of the recording medium for short term changes. A typical example would be a flight over sea and then land, both objects having a large temperature difference between them, but of more direct interest is the temperature differences within the sea-scape and within the landscape. A.C. coupling effectively allows each target to occupy the full dynamic range of the recording medium despite the large difference in temperature between them.

In many cases A.C. coupling satisfies the researchers' needs; however, it does not permit relative comparison or absolute determination of temperatures/emittance along the flight line. D.C. coupling permits the system to be calibrated but at the same time restricts the sensitivity of the system, and makes it highly susceptable to fluctuations (noise) in the aircraft electrical system.

3.6 Film Recording/Replay

Film medium is used both as a recording medium and in the case of video recorded signals, for displaying the replayed information. In both cases the system used (see Fig. 3.6) is identical and imitates in reverse the original scanning procedure.

The signal modulates the intensity of an oscilloscope spot being swept across the screen (Fig 3.6). The focussed image of the spot is recorded on slowly moving film. The width of the film W (cms.), film speed U (cms./sec.), aircraft speed V (metres/sec.) and amount of 'ground' replayed S (metres) are related by 3.8:

FIGURE 3.6 SHOWING THE FILM REPLAY SYSTEM USED IN CONJUNCTION WITH THE INFRA-RED LINE-SCANNER.

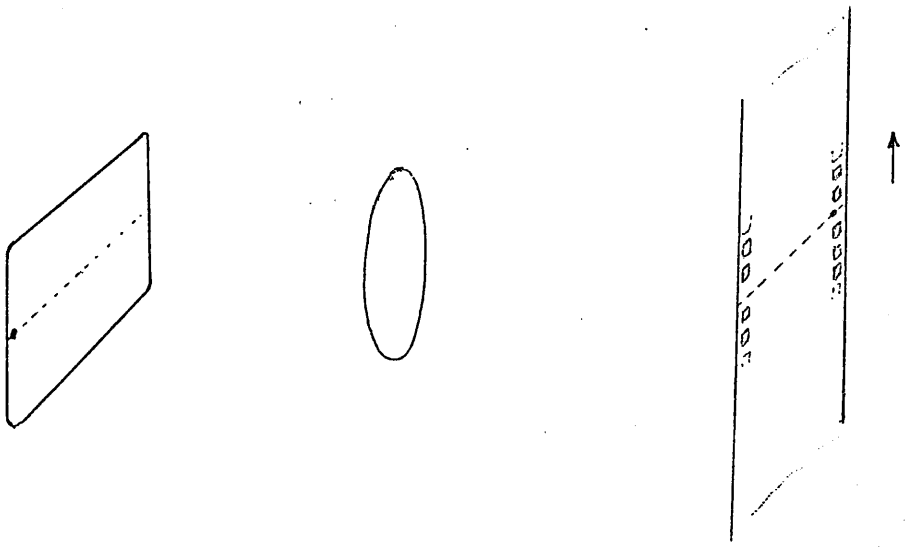

C.R.T. WITH INTENSITY MODULATED SPOT SWEPT HORIZONTALLY ACROSS THE SCREEN.

FOCUSSING LENS.

FILM DRAWN VERTICALLY AT A CONSTANT RATE TO SIMULATE THE SCALED AIRCRAFT MOTION.

FIGURE 3.7 SHOWING TYPICAL SPECTRAL REFLECTANCE CURVES (REF. 6).

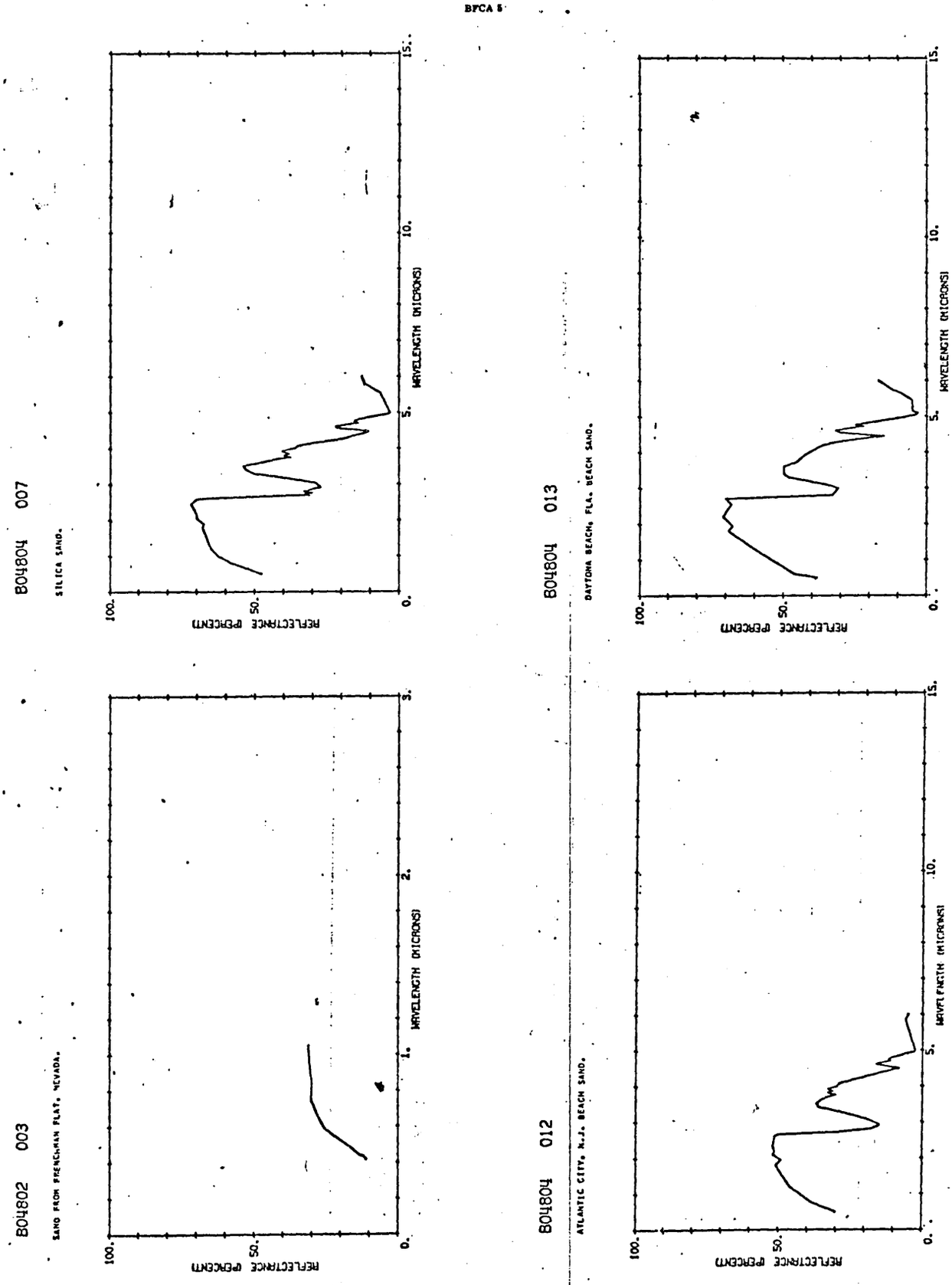

$$\frac{U}{V} = \frac{W}{S} \qquad 3.8$$

Thus for a typical flight at 8,000 metres with forward velocity 400 m/sec replaying $\pm 45^{\circ}$ from the nadir on to 35mm film (24mm useful width):

$$U = 0.12 \text{ cms./sec.}$$

The sweep speed of the spot across the oscilloscope is usually constant but this results in severe distortions of the scan due to its non-linear recording (see equation 3.7) although a matched sweep can be constructed.

The limiting factor in replay systems is the spot size. From the parameters of usable film width W, spatial resolution of the detector θ , and total scan angle from nadir used for replay, the desired spot size can be derived.

For a useful scan angle of $\pm \alpha$ radians from the nadir, the number of picture elements is:

$$\frac{2\alpha}{\theta} \qquad 3.10$$

Consequently both the C.R.T and the film must be capable of resolving at least twice this number. Typical values for a 10 cms. laboratory oscilloscope imply a 0.05mm spot. Consequently television-type cathode ray tubes are preferred where the effective spot size is smaller.

Similar considerations show that for 35mm film with a useable emulsion width of 24mm, the required resolving power is 80 lines/mm (c.f. 75 lines/mm for low contrast targets with Ilford FP3).

Commercial replay systems are available which draw the film either across the cathode ray tube or over a line of fibre optic light guides linked to the tube (5). However the resolution of such systems is below that shown to be necessary.

3.7 System Performance Parameters

The system discussed below was supplied on hire from E.M.I.

The basic parameters of the EMI 'Airscan' system are:

Collection Aperture: 100mm diameter

Scanner Rate: 3,000 revs/min. (fixed)

Maximum useful cross-track sweep: $\pm 70^{\circ}$ from the nadir

Detector: Indium Antimonide at $77^{\circ}K$. Sensitivity maximum in 3.5 - 5.5 μm waveband.

Recording medium: Sony Video tape-recorder

Table 3.1 shows the relationship between the detector element size and the angular and thermal resolution.

A spatial resolution of 1.3 milli-radians with a 0.2mm sq. element is only obtained under optimum conditions and for calibration purposes the manufacturers recommend 1.5 milli-radians.

The aircraft used for the study, a Dakota, was typical of survey aircraft being able to cruise under stable conditions at 45 metres/sec. and over. Consequently, the minimum altitude for satisfactory line scanning is 600 metres (derived from equation 3.6).

The data rate is related to the angular resolution of the detector (θ) and to the angular velocity of the mirror Ω. Each mirror revolution the 2π radians are equivalent to $(2\pi/\theta)$ distinct, relevant samples. Each mirror revolution takes $(2\pi/\Omega)$ seconds - where Ω is in radians/sec. and the data rate, D (H_z) is given by 3.12.

$$D = \frac{2\pi}{\theta} \cdot \frac{\Omega}{2\pi} = \frac{\Omega}{\theta} \ (H_z) \qquad 3.12$$

The values of Ω and θ for the EMI system were $100.\pi$ radians/sec. and 1.5×10^{-3} radians respectively and hence:

$$D \approx 200 \ KH_z$$

TABLE 3.1 Detector Characteristics for EMI 'Airscan' System

Element Size (mm. sq.)	Angular Resolution (Milli-Radians)	Thermal Resolution (^{o}C)
0.2	1.3	0.2
0.5	3.3	0.075
1.0	6.7	0.021

Thus in order to record faithfully the detector output, sampling theory requires a bandwidth of at least 400 KH_z, a figure within the performance envelope of video tape-recorders.

The useful picture resolution of the system is quoted by EMI as being 500 picture points, as opposed to a value of 1,000 when derived from equation 3.10. This lack of resolution is probably due to the cathode ray tube spot size being too large even though a 21 inch tube was used.

The response of the replay equipment in terms of the relationship between video recorder output and density on the processed recording film was not given but was measured from stepped input voltages fed to the cathode ray tube prior to each tape replay. Such a step had to be taken as both during recording and replay of the "video" data the gain and bias of the detector signal amplifier circuits were adjusted so as to optimise the recorder bandwidth. In all cases the recording settings were logged.

3.8

CHAPTER 3 - REFERENCES

(1) ROBINSON, N: Solar Radiation, Elsevier, London, 1966

(2) MULLARD: Information Sheet "Application of I.R. Detectors"

(3) PLESSEY CO. LTD: Infra-Red Imager, Publication No. RSL 1179

(4) BENDIX: IEEE Transactions, No.3, July 1971

(5) HONEYWELL: Line-scan Recording Oscilloscope

(6) N.A.S.A.: Earth Resources Spectral Information System

(7) LYON, R.J.P.: J. Geophys., Res. 77, p2473-2477, 1973

4 INFRA-RED RADIATION FROM TERRESTIAL OBJECTS WITH REFERENCE TO THE 4.5 - 5.5μm BAND OF WAVELENGTHS

4.1 Introduction

It was shown earlier (Section 3.1) that in order to reduce the effects of reflected solar radiation to a negligeable level, the sensitivity of the detector must be restricted to wavelengths longer than 3.5μm The EMI Airscan equipment used in the Australian study was therefore fitted with a 4.5 - 5.5μm band-pass filter Type ITT E 5861F and it was proposed to restrict the time of line-scanner operation to pre-dawn. A departure from this proposed scheduling resulted from logistics difficulties dealt with in Section 2.3.

Measurements made at a distance of the radiation emitted from the surface of the earth cannot be entirely precise and unambiguous because of the effects of solar radiation and of the atmosphere between the earth and the detector. Observations made at wavelengths between 4.5 and 5.5μm are not directly influenced by solar radiation whether it be reflected by the ground or scattered by the atmosphere within the field of view (F.O.V.) of the detector. However, the surface temperature of the earth is a function of the solar radiation reaching the ground and in areas with relatively little cloud cover, the temperature of the ground dominates the heat exchange between the sun and the environment.

The surface temperature of the earth is a function of parameters such as emissivity, albedo, etc., but in some cases sub-surface effects manifest themselves as thermal anomalies at the surface. (The term anomaly is used to imply an effect which, although evident as a temperature different from the surroundings, was not anticipated from observations using different sensors such as conventional aerial photography.) Thermal anomalies are by definition a consequence of heat flows, the magnitude and detectability of which have been studied by Haze (1) who hypothesised

two quantities described below to indicate the magnitude of heat flows required for detection at the surface as thermal anomalies.

These were:

(i) The depth(S) of penetration of diurnal temperature variations.

(ii) The magnitude (M) of the average solar heat flow at depth S.

Typical values of S and M are 80 cms and 240 μ cal. cm^{-2} $sec.^{-1}$ respectively.

Surface heat flows less than M are considered too small to be detectable as diurnal changes will easily mask them.

The maximum solar energy absorbed by the surface of the earth is of the order of 2,000 μ cal. cm^{-2} $sec.^{-1}$ and surface heat flows between M and this figure are capable of detection under favourable situations - such as at night with a relatively uniform terrain.

Sub-surface heat flows greater than 2,000 μ cal. $cm.^{-2}$ $sec.^{-1}$ represent effects such as fires in coal tunnels, geysers and volcanoes and the causes are generally self-evident from conventional photography.

The implication of the heat flows discussed above is that effects such as oxidising ore bodies, underground pipelines (where the transported liquid is at a temperature different from that of the surroundings) and other sub-surface natural phenomena which have thermal anomalies associated with them, are undetectable due to the heating effects of solar radiation

4.2 The Effects of the Atmosphere on the Detected Signal

The factors influencing the signal at the detector are discussed in conjunction with Figure 4.1.

Figure 4.1

Factors inflencing the signal sensed by the detector.

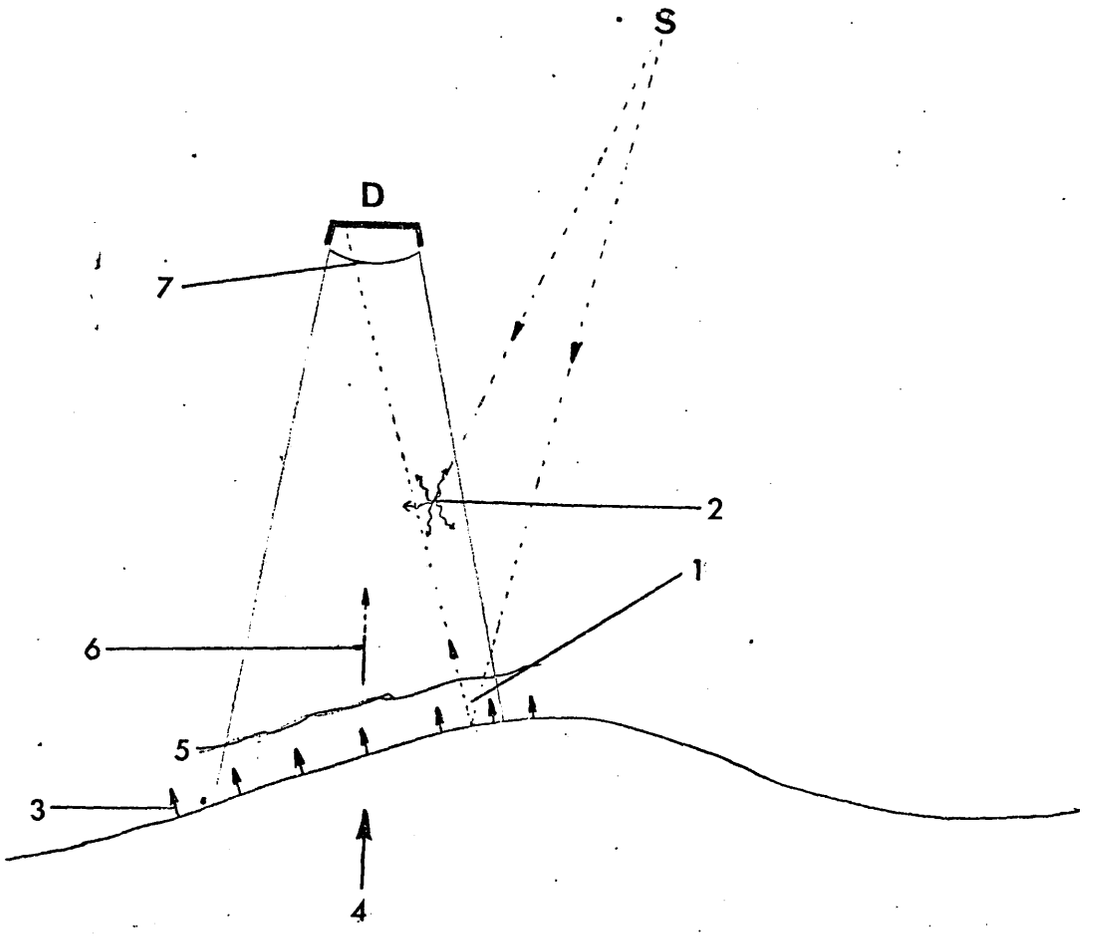

S Sun

D Detector

1 Reflected Solar Radiation

2 Scattered Solar Radiation

3 Re-emitted Solar Radiation

4 Geothermal Radiation

5 Conduction by Winds

6 Atmospheric Absorption

7 F.O.V. of Detector

4.2.1 Scattering of Infra-Red Radiation by Atmospheric Particles

The dimensions of atmospheric particles range from $10^{-3}\ \mu m$ (individual molecules) to $10^{3}\ \mu m$ (meteorites) and the dimensions determine the magnitude and form of the scattering. Of particular interest are fog, rain and mist particles with dimensions $\gg 5\mu m$ smoke particles in the range $1\text{-}10^{-2}\ \mu m$ and heavy industrial pollutants 1-3 μm. Haze, in dry regions remote from large areas of water, consists of particles of the order 0.04 - 1.0 μm in diameter (2).

Scattering of radiation between ground level and 5,000 metres is of three forms:

(i) Resonant
(ii) Rayleigh
(iii) Mie

Resonant scattering occurs when the wavelength of the incident radiation approaches that of one of the absorption lines associated with the atmospheric particle or aerosol. The incident radiation is absorbed as the particle is raised to a short lifetime excited state, and then re-emitted on its decay. The scattering cross-section of radiation at the resonant wavelength(s) is thus sharply increased. However, the width of the absorption lines is small compared with the 1 μm waveband used in the study and their effects are negligeable. (Absorption lines are exploited by examining the backscatter from tunable lasers, but such work is outside the present line of research.)

Rayleigh scattering of radiation occurs when the wavelength of the incident radiation (λ) is much greater than the diameter (d) of the individual scattering particles, e.g. $d \leqslant 0{\cdot}2\lambda$. The magnitude of the scattering is proportional to $(1/\lambda)^4$ and the scattering coefficient per unit length at wavelength λ, β_λ is given by:

$$\beta_\lambda = \frac{32\pi^3 (n_\lambda - 1)}{3 N \lambda^4} \qquad 4.1$$

where: n_λ is the refractive index of the particle at wavelength λ

N is the number of particles per unit volume

Values of σ_λ for Rayleigh scattering along a vertical path through the atmosphere are given in Table 4.1 (3), together with q_λ, the fraction of energy received at ground level with respect to that at the top of the atmosphere.

TABLE 4.1

Wavelength (μm)	σ_λ	q_λ
0.30	52×10^{-8}	0.295
0.60	8.6×10^{-8}	0.933
0.90	1.7×10^{-8}	0.987
4.00	4.2×10^{-10}	1.000

Thus the shorter, visible, wavelengths are preferentially scattered and the scattering of infra-red radiation in the 4.5 to 5.5 μm waveband is very small. Smaller in fact than the black-body radiation associated with the earth or clouds (4).

Scattering of radiation with wavelength λ when the radius of the particles, r, is of the order of λ e.g. $0.1\lambda < r < 25\lambda$ is described by Mie theory.

Thus the 4.5 - 5.5 μm waveband is particularly susceptible to particles with diameters from 0.5 to 150 μm such as heavy pollutants, smoke, weather particles and strong haze. Partly due to this the area of Western Queensland was chosen because of the absence or near minimal effects of such scattering as a consequence of the good weather and sparse industry within the region.

4.2.2 Absorption of Infra-Red Radiation by the Atmosphere

The absorption spectra in Figure 3.3 indicate the molecules which contribute most to the attenuation of radiation in the

4.5 - 5.5 μm waveband. Table 4.2 (5) details the characteristics of the absorption bands, whilst in Table 4.3 the percentage transmission through water vapour for a selection of wavebands is given.

TABLE 4.2 Atmospheric constituents and their absorption characteristics

Constituent	Band Centre (μm)	Mean Concentration (by volume)	Width of band (μm)
CO	4.8	2×10^{-5} %	0.25
N_2O	4.6	4×10^{-5} %	0.33
H_2O	6.3	Variable below 10Km	3.0

TABLE 4.3 Transmission through an atmosphere containing 1cm. of precipitable H_2O in path (6)

Band (μm)	% Transmission	(Path length ~1Km.)
0.72 - 0.94	0.91	
0.94 - 1.13	0.89	
2.70 - 4.30	0.58	
4.30 - 6.00	0.31	

The fluctuation in the concentration of water molecules, carbon dioxide and the magnitude of the resulting changes in absorption are shown in Figures 4.2.1 and 4.2.2 (7). Of particular importance is the effect which changing water vapour content (relative humidity) has on the absorption in view of the terrain in Western Queensland which was semi-arid but with heavy vegetation near to the rivers. This resulted in highly variable humidities both with geographical location and time of day.

4.3 Absorption and Reflection of Solar Radiation by the Terrain

The intensity of the infra-red radiation emitted from the surface of the earth is a function of the temperature of the surface, and

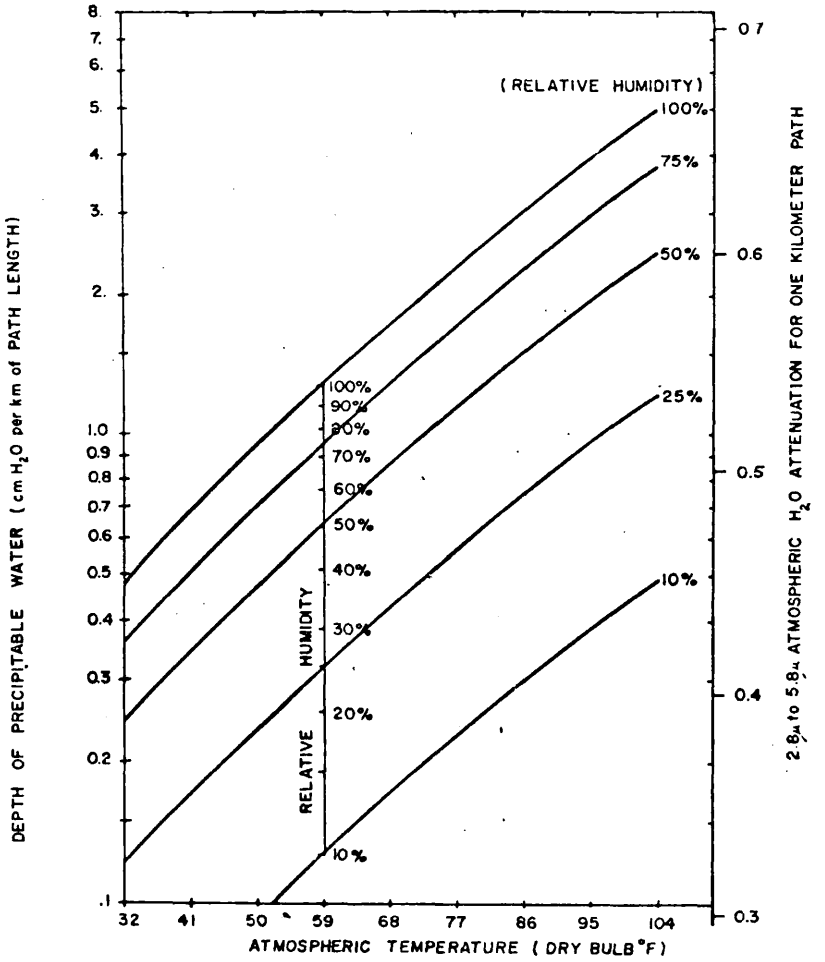

Fig.4.2.1 Atmospheric attenuation by water predicted from temperature and relative humidity measurements.

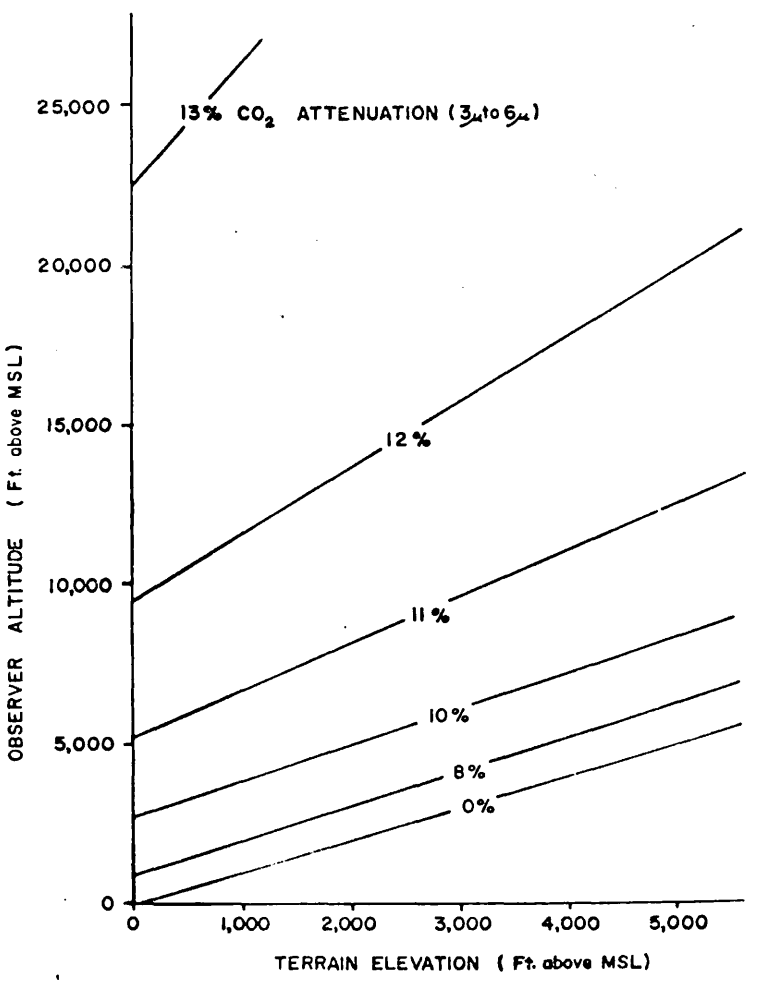

Fig.4.2.2Attenuation by atmospheric CO_2 (3 μ to 6 μ). Expected in the vertical observer-to-ground optical path.

most of the heating of the surface is due to the absorption of solar radiation in the visible and infra-red wavelengths up to 3.5 μm . A major factor affecting the absorption of radiation is the albedo of the terrain, the albedo being defined as the ratio of the total amount of radiation reflected, both specularly and diffusely, by a surface to that incident upon it.

Examination of Figure 3.3 reveals that the maximum intensity of solar radiation reaching ground level is in the visible and near infra-red wavebands and hence the albedo used for calculating the energy absorbed by the earth must refer to these wavebands.

Table 4.4 gives the percentage reflectance and wavelength of peak reflectance for representative soil, rock and vegetation samples but it was not made clear from the data (8) whether the albedo was calculated with respect to the solar spectrum or not.

TABLE 4.4 Percentage reflectances and wavelengths of Peak Reflectance for terrestial surfaces (8).

Surface	% Reflectance	Wavelength (μm) of Peak Reflectance
Water	3 - 10	0.48
Snow	70 - 86	0.48
Limestone	63	0.58
Calcareous rocks	30	0.58
Granite	12	
Sand	18 - 31	0.56
Lush grass	15 - 25	0.57
Dry grass	3 - 8	0.576
Field crops	7 - 15	0.586
Ploughed field	20 - 25	
Deciduous forest	10 - 15	0.572 - 0.586
Coniferous forest	3 - 10	0.574 - 0.576
Rich soil	7.5 - 20	0.583

The mechanisms which bring about differences in reflectances between soils, rocks and vegetation types are discussed more fully in Chapter 5, but in all cases the amount of energy absorbed will be a function not only of the albedo but also of the incident radiation intensity which is governed by the orientation of the surface with respect to the sun.

4.4 Emission of Infra-Red Radiation from the Terrain

The fundamental properties of matter relating to the electromagnetic radiation from black-bodies have been discussed earlier (Chapter 3), the relevant equations being:

Stefan-Boltzmann's law:

$$W = \sigma T^4 \qquad 4.2$$

Planck's law:

$$W_\lambda = \frac{C_1}{\lambda^5} \cdot \frac{1}{(e^{C_2/\lambda T} - 1)} \qquad 4.3$$

Equation 4.2 relates the total amount of radiation per unit area W, emitted from a black-body to its absolute temperature T. For non-black bodies the equation is modified to the form:

$$W = \epsilon \sigma T^4 \qquad 4.4$$

where ϵ is the emissivity of the body and is defined as the total amount of radiation emitted per unit area by a body compared to that emitted by a black-body at the same temperature. The emissivity varies not only from body to body but also with wavelength. Thus with infra-red detectors the radiation $W_{\lambda(a-b)}$ sensed in the waveband (a → b) μm is a function of the emissivity as defined by the equation:

$$W_{\lambda_{a\to b}} = \frac{1}{(b-a)} \int_{\lambda=a}^{\lambda=b} W_\lambda \cdot \epsilon_\lambda \cdot d\lambda \qquad 4.5$$

The absorptance, a, of a body is defined as the fraction of radiation incident upon it which is absorbed.

The principle of conservation of energy requires that for an opaque body in dynamic thermal equilibrium the energy incident upon it must equal the sum of that reflected and absorbed.

Thus if E units of energy are incident upon a body with absorptance a, and emissivity ϵ, (1-a)E units are absorbed and ϵE are emitted.

$$\therefore \quad E = \epsilon E + (1-a)E \qquad 4.6$$

i.e. $\epsilon = a$

A similar argument yields

$$\epsilon_\lambda = a_\lambda \qquad 4.7$$

If p_λ is defined as the fraction of incident radiation reflected by an opaque non-black body at wavelength λ, then by conservation principles:

$$a_\lambda + p_\lambda = 1 \qquad 4.8$$

thus, from equations 4.7 and 4.8 we find that for non-black opaque bodies:

$$\epsilon_\lambda = 1 - p_\lambda \qquad 4.9$$

The case of leaves and semi-transparent soil particles requires a modified expression for the emissivity and McMAHON (9) showed that for semi-transparent parallel sided bodies with a true transmissivity τ_λ at wavelength λ the effective emissivity ϵ_λ is given by:

$$\epsilon_\lambda = \frac{(1-\rho_\lambda)(1-\tau_\lambda)}{(1-\rho_\lambda\tau_\lambda)} \qquad 4.10$$

4.5 The Surface Temperature of the Terrain

Equation 3.12 showed that the predicted dependence of the signal at the detector on the temperature of the surface of the terrain should be of the form:

$$W = \epsilon\sigma T^{9.7}$$

The temperature of the surface is the result of the solar heating, and radiative and convective cooling processes which it has undergone. Considerations of heat flow enable a model to be built which predicts the surface temperatures for different times of day and different surface types.

The heat flow in a direction z expressed in terms of the quantity of heat (Q) flowing in a time t, through a section of thickness dz of terrain with thermal conductivity and cross-sectional area (A) at a temperature θ is given by:

$$\frac{dQ}{dt} = -kA\frac{d\theta}{dz} \qquad 4.11$$

This assumes that the heat flow is wholly in the direction z and there is no outward heat flow, the case of an infinitely wide surface bounded by a plane.

In the case of the earth, the heat flow is constantly changing due to the varying solar radiation incident upon it. (These fluctuations can be considered as temporal changes at a given depth, or spatial changes at a given time.) Considering the latter; differentiation of 4.11 gives:

$$\frac{d}{dz}\left(\frac{dQ}{dt}\right) = -kA.\frac{d^2\theta}{dz^2} - A.\frac{d\theta}{dz}.\frac{dk}{dz} \qquad 4.12$$

$\frac{dk}{dx}$ represents the change of thermal conductivity with depth of terrain. Although the constitution of surface and sub-surface layers is known to change, and hence $\frac{dk}{dz} \neq 0$ the amount of environmental ground work required to determine $\frac{dk}{dz}$ over the range $z = 0 \rightarrow 100\text{cms}$ would be excessive and for convenience $\frac{dk}{dz}$ is treated as zero.

For a section of terrain with thickness dz, cross-sectional area A, density p, and specific heat c, the heat flow rate out of it due to a rate of change of temperature $\frac{d\theta}{dt}$ is, by definition, given by:

$$\rho.dz.A.c.\frac{d\theta}{dt} \qquad 4.13$$

But this quantity is equivalent to that implied in equation 4.11. Thus from equations 4.11 and 4.13:

$$\rho.dz.A.c.\frac{d\theta}{dt} = -kA\frac{d^2\theta}{dz^2} \qquad 4.14$$

$$\therefore \quad \frac{d\theta}{dt} = -\frac{k}{\rho c}.\frac{d^2\theta}{dz^2} \qquad 4.15$$

($\frac{k}{\rho c}$ is a constant term for a given material and is known at the diffusivity) Thus from equation 4.15 if the temperature profile of the terrain with depth $\theta \rightsquigarrow z$ is known then $\frac{d^2\theta}{dz^2}$ can be determined and the night-time temperatures could be predicted.

4.6 Models for Predicting the Temperature Variation of the Terrain Surface with Time

From the considerations in the previous section models have been derived for surface temperature predictions.

A model was published in 1932 by Brunt (10) which described the surface temperature of the terrain at night as a function of time and the temperature of the terrain at sunset. The derivation, outlined below, required the empirical fitting of data to obtain certain constants (equation 4.18).

Equation 4.15 is expressed in the form:

$$\frac{d\theta}{dt} = K_1 \frac{d^2\theta}{dz^2} \qquad 4.16$$

where z is the distance below the surface of the terrain, positive being taken as downwards. (K_1 the diffusivity of the earth was taken by Brunt to have a value of (4.7×10^{-3} c.g.s. units.)

The net heat loss to the atmosphere R_N per unit volume is given by:

$$R_N = K_1 \rho_1 c_1 \cdot \left.\frac{d\theta}{dz}\right|_{z=0} \qquad 4.17$$

where ρ_1 and c_1 are the density and specific heat respectively of the terrain (cf. equation 4.13). Results of measurements showed that an empirical relationship could be derived between R_N and the surface temperature T of the form:

$$R_N = \sigma \theta^4 \left(1 - a - b\sqrt{e}\right) \qquad 4.18$$

(c.f. equation 4.2 i.e. a modified black-body radiation heat loss)

By assuming that the changes in vapour pressure and θ were small, and hence that the relative changes in θ were negligeable during the night R_N can be treated as a constant.

Thus from equation 4.17:

$$\left.\frac{d\theta}{dz}\right|_{z=0,\ \text{Sunset} < t < \text{Sunrise}} = \text{CONSTANT} \qquad 4.19$$

Thus the problem reduces to finding a solution to equation 4.16 with 4.19 as the boundary condition.

θ is known to be a function of z and t

$$f(\theta) = f(z,t)$$

Considering the relationship:

$$\theta = \frac{1}{\sqrt{t}} \cdot e^{-z^2/4K_1 t} \qquad 4.20$$

$$\frac{d\theta}{dt} = \frac{e^{-z^2/4K_1 t}}{\sqrt{t}} \cdot \frac{z^2}{4K_1 t^2} - \frac{1}{2} \cdot \frac{1}{t^{3/2}} \cdot e^{-z^2/4K_1 t}$$

$$= \frac{e^{-z^2/4K_1 t}}{2\sqrt{t}} \cdot \left[\frac{z^2}{2K_1 t^2} - \frac{1}{t} \right] \qquad 4.21$$

$$\frac{d^2\theta}{dz^2} = \frac{e^{-z^2/4K_1 t}}{2K_1 t\sqrt{t}} \cdot \left[\frac{z^2}{2K_1 t} - 1 \right] \qquad 4.22$$

From 4.21 and 4.22

$$\frac{d\theta}{dt} = K_1 \cdot \frac{d^2\theta}{dz^2}$$

Therefore $\mathcal{E}$ as defined by equation 4.20, is a particular integral solution of 4.16 and the solution

$$\theta = \frac{1}{2\sqrt{\pi K_1 t}} \cdot e^{-(z-z')^2/4K_1 t}$$

must also be a solution

In fact, the sum of a number of particular integral solutions satisfied 4.16.

Thus

$$\theta = \frac{1}{2\sqrt{\pi K_1 t}} \cdot \int_{-\infty}^{+\infty} f(z') \cdot e^{-(z-z')^2/4K_1 t} \, dz' \qquad 4.23$$

is also a solution

It can be shown ((10), p34) from 4.23 that by letting $z' = z + 2\epsilon\sqrt{K_1 t}$ the limiting value of 4.23 is:

$$\theta = f(z) \qquad 4.24$$

Thus, if the initial temperature of the ground is described by equation 4.24 the distribution at any time (t) is given by 4.23.

Thus for a constant flux at the surface for all values of t it can be shown that the surface temperature θ (o,t) is of the form:

$$\theta(0,t) = \theta(0,0) - \frac{2}{\pi} \cdot \frac{R_N \sqrt{t}}{\rho_1 c_1 \sqrt{K_1}} \qquad 4.25$$

The relationship shows the general surface temperature decay with time at night. However, it is not sufficiently developed to enable the effects of variables, such as night-time air temperatures, to be taken into account.

The above theory was developed further by Carshaw and Jaeger (11) to predict the surface temperatures throughout a 24 hour cycle.

The net radiation flow, $f(\omega)$, $(\equiv f(q,t))$ is of the form:

$$f(\omega) = -I\sin\omega - R_N \qquad \text{for } -\pi < \omega < 0 \qquad \text{i.e. daytime} \qquad 4.26$$

$$f(\omega) = -R_N \qquad \text{for } 0 < \omega < \pi \qquad \text{i.e. night-time} \qquad 4.27$$

where R_N is as defined before; I is the solar radiation intensity at the ground plane, w is the angular velocity of the earth.

Let f (w) be a fourier series of the form:

$$f(\omega) = A_0 + A_1\cos\omega + A_2\cos 2\omega + \cdots + A_n\cos n\omega + \cdots + B_1\sin\omega + B_2\sin 2\omega + \cdots + B_n\sin n\omega + \cdots \qquad 4.28$$

A fundamental theorem states that

$$A_n = \frac{1}{\pi}\cdot\int_{-\pi}^{\pi} f(\omega)\cdot\cos n\omega\, d\omega \qquad 4.29$$

and

$$B_n = \frac{1}{\pi}\cdot\int_{-\pi}^{\pi} f(\omega)\cdot\sin n\omega\, d\omega \qquad 4.30$$

Thus from equations 4.29 and 4.30

$$A_n = \frac{1}{\pi}\left[\int_{-\pi}^{0}(I\sin\omega + R_N)\cos n\omega\, d\omega - \int_{0}^{\pi} R_N\cos n\omega\, d\omega\right] \qquad 4.31$$

for odd values of n (and $n \geq 1$)

$$A_n = 0 \qquad 4.32$$

for even values of n, $n > 2$

$$A_n = \frac{-2I}{(n^2-1)\cdot\pi} \qquad 4.33$$

also

$$A_0 = \frac{I}{\pi} - R_N$$

Similarly from equations 4.29 and 4.31 the only value of Bn which is non-zero is for n = 1 and thus,

$$B_1 = -\frac{I}{2} \qquad 4.34$$

A_0 is a constant and represents the net heat flow across the surface over one complete period i.e. 24 hours. A fair approximation is for this to be zero as the variations being studied are diurnal rather than annual.

Thus from equation 4.33

$$R_N = \frac{I}{\pi} \qquad 4.35$$

Thus in terms of q and t, equation 4.20 is now of the form

$$f(q,t) = I\left\{-\tfrac{1}{2}\cdot \mathrm{Sin}qt - \frac{2}{\pi}\left(\tfrac{1}{3}\mathrm{Cos}qt + \tfrac{1}{15}\cdot \mathrm{Cos}4qt + \cdots\right)\right\} \qquad 4.36$$

Now the surface temperature variation T(t) can be regarded as a periodic function of time with period $\left(\frac{2\pi}{q}\right)$ and as the net heat loss has been assumed to be zero, T (t) can be written in the form:

$$T(t) = T_0 + P_1 \cdot \mathrm{Cos}(qt - \epsilon_1) + P_2 \mathrm{Cos}(2qt - \epsilon_2) + \cdots \qquad 4.37$$

But .. T(t) must be such as to obey the conditions implied by equations 4.16 and 4.17 and it can be shown that T(t) is of the form:

$$T(t) = T_0 + \sum_{n=1}^{\infty} P_n \cdot e^{-z\sqrt{\frac{nq}{2\kappa_1}}} \cdot \cos\left[nqt - \epsilon_n - z\sqrt{\frac{nq}{2\kappa_1}}\right] \qquad 4.38$$

Now $$f(q,t) = -\rho_1 c_1 \kappa_1 \cdot \left.\frac{dT}{dz}\right|_{z=0} \qquad \text{by definition} \qquad 4.39$$

Thus, by substitution after differentation of equation 4.38 for

$\left.\frac{dT}{dz}\right|_{z=0}$ from equation 4.39

$$T'(t)\Big|_{z=0} = \sum_{n=1}^{\infty} P_n \sqrt{\frac{nq}{2\kappa_1}} \cdot \sin(nqt - \epsilon_n) \qquad 4.40$$

and

$$f(q,t) = -\rho_1 c_1 \sqrt{\kappa_1} \cdot \sum_{n=1}^{\infty} P_n \cdot \sqrt{\frac{nq}{2}} \cdot \sin(nqt - \epsilon_n) \qquad 4.41$$

Equations 4.36 and 4.41 are identical and thus by comparison of terms of (qt):

$$P_1 = \frac{I}{2\rho_1 c_1 \sqrt{\kappa_1 q}} \quad ; \quad \epsilon_1 = -\frac{\pi}{4}$$

for all odd $n>1$; $P_n = 0$; $\epsilon_n = 0$

for all even $n>0$; $P_n = \frac{-2I}{\pi(n^2-1)} \cdot \frac{1}{\rho_1 c_1 \sqrt{nq\kappa_1}}$; $\epsilon_n = \frac{\pi}{4}$

Thus equation 4.38 becomes upon substitution:

$$T = T_0 + \frac{2R_N}{\rho_1 c_1 \sqrt{q\kappa_1}}\left[\frac{\pi}{4} \cdot \cos\left(qt + \frac{\pi}{4}\right) - \sum_{n=2}^{\infty} \frac{\cos(nqt - \pi/4)}{(n^2-1)\sqrt{n}}\right] \qquad 4.42$$

From equation 4.35, $R_N = I/\pi$; however, direct substitution of this relationship into equation 4.42 is valid only for flat (horizontal) surfaces at the equator. The effects of different latitudes and time of year (both factors affecting the angle of the sun at the surface and thus the incident radiation absorbed per unit area) are accounted for in the equations below (12).

$$T = T_o + \frac{I}{\sqrt{\rho_1 c_1}\sqrt{\omega\lambda}} \cdot \cos\lambda \cdot \cos\delta \cdot \phi(t) \qquad 4.43$$

where; $$\phi(t) = 2\sum_{n=2}^{\infty} \frac{(\sin nh \cdot \cosh - \cos nh \cdot \sinh) \cdot \cos(n\omega t - \pi/4)}{\pi n^{3/2}(n^2-1)}$$

$\omega = \frac{2\pi}{24}$ radians per hour (The diurnal angular velocity of the earth).

$\lambda \equiv$ latitude

$\delta \equiv$ declination of the earth's axis w.r.t the sun

$t \equiv$ time after local noon

$\cos h = -\tan\lambda \cdot \tan\delta$

A more advanced version of the above model is incorporated in the work of Watson (13). The daytime and night-time air temperatures are a part of the model so as to give a measure of the "effective" temperature of the ground. A cloud cover factor is incorporated to modify the intensity of the incident solar radiation and the albedo of the terrain can be set to an appropriate value. The transmission M of the atmosphere, previously assumed to be unity, is a function of the path length through the atmosphere and is of the form M(Z) suggested by Allen (14).

$$M(Z) = 1 - 0{\cdot}2\sqrt{\sec Z}$$

where Z is the Solar zenith angle i.e.

$$\cos Z = \cos\lambda \cdot \cos\delta\,(\cos\omega t + \tan\lambda \cdot \tan\delta)$$

The effects of sloping terrain are allowed for by modifying Z by the dip angle d, and the strike azimuth measured from north ϕ. Z' the "effective" solar zenith angle is given by:

$$\cos Z' = \cos(\lambda - d\sin\phi).\cos\delta.(\cos(\omega t + d\cos\phi) + \tan(\lambda - d\sin\phi)\tan\delta)$$

The mathematical model suggested by Watson has been developed as a computer programme available through the U.S. National Technical Information Service (15). This was acquired and subsequently modified to run on the University CDC 6600 computer. The programme assumes initial temperatures for the terrain at night and day and then calculates in a step-wise fashion the corresponding temperatures 24 hours later. Ultimately these will be the same and the initial estimates are modified iteratively until a fit is found.

4.7 Discussion of the Thermal Model

The programme package referred to above represents the most advanced readily available model incorporating the flexibility of inputting different cloud covers, albedos, air temperatures, emissivities, geographical position and topographical orientation. However, the cloud cover is assumed constant over 24 hours and the air temperatures to be constant over a 12 hour period. The programme could be modified so as to include these as continuous variables, but the amount of environmental monitoring required would probably not justify the effort.

The area of greatest uncertainty is felt to be the surface properties of the terrain where the effects of weathering, moisture, chemical composition and vegetation cover can radically alter the thermal properties of the terrain.

An estimate of the albedo of a surface can be determined by the use of a spectro-radiometer or very roughly estimated from black and white photographs.

The emissivity however is more difficult to determine. An extreme case is quoted by Watson (13) where the thermal effect of a 2 cm. layer of dry lichen is to mask completely the underlying rock strata. The same reference deals with the variation of the thermal inertia P, defined by the equation $P = (K\rho c)^{1/2}$ (K: specific (thermal) conductivity; p density; c specific heat) with varying amounts of moisture in porous rocks. The basic equations and the magnitudes of the effects are summarised:

$$A = \frac{2^n}{2^n - 1} \cdot \left\{ 1 - \frac{1}{(1+f)^n} \right\} \qquad 4.44$$

where A is derived for a given rock
f is the % porosity of the rock
n is an empirical exponent determined for each rock type
n $\sim$ 2 for sandstones
$\sim 4\frac{1}{2}$ for carbonates.

The effective conductivity, K, of the porous rock and the saturating intruding medium is given by:

$$K = (1-A) K_S + A K_f$$

where K_S is the conductivity of the solid
and K_F is the conductivity of the intruding medium.
The product of the density P, and specific heat, c, of the mixture is similarly expressed as:

$$\rho c = (1-f)\rho_s c_s - f \rho_f c_f \qquad 4.45$$

where the subscripts s and f denote solid and intrusion respectively.

Thus the thermal inertia P of the mixture is given by combining equations 4.44 and 4.45.

$$P^2 = \left[(1-A) K_s + A K_f\right] \cdot \left[(1-f)\rho_s c_s + f \rho_f c_f \right] \qquad 4.46$$

Typical values for sandstone are $f \sim 8\%$; $n \sim 2$

$K = 0.006$; $\rho_s = 2.3$; $c_s = 0.23$

units; cals/cm.sec.deg.; g/cm^3; cal/gm.deg. respectively

and if water is the intruding medium

$K = 0.00144$; $\rho_f = 1$; $c_f = 1$

Thus from 4.44

$$A \approx 0.19\%$$

and from 4.46

$$P \approx 0.055$$

for an air saturated sample, 4.46 can be approximated to the form:

$$P^2 = (1-A)(1-f)P_s^2 \qquad 4.47$$

For a dry sample of sandstone the value of P is 0.048 and the saturation (8% by volume) of sandstone with water will alter the thermal inertia by 13%

Furthermore the emissivity of water is unity, so increasing water content results in an increased rock emissivity and increased albedo.

Table 4.5 lists the terrain surfaces encountered in Australia for which information is available, together with various loams indicating how soil contents affect reflectance and emissivity values.

The computer model was further modified so as to display the results graphically on microfilm together with the values of thermal inertia, albedo etc., which were later used (example Figure 4.8). Typical results are presented and discussed when they are compared with ground temperature readings.

TABLE 4.5 THE THERMAL, EMISSIVE AND REFLECTANCE PROPERTIES OF TYPICAL SURFACES

Surface	Thermal Inertia (cals/gm sec½)	Albedo (%)	Reference
Quartz (rock)	0.098		11
Quartz sand dry	0.014		11
Quartz sand 8% moisture	0.030		11
Quartz sand 10% moisture	0.034		11
Quartz sand 22% moisture	0.047		11
Water	0.038	0 (if deep)	
Granite	0.057	20	13
Limestone	0.047	30	13
Sandstone	0.056		13
Calcite	0.075		16
Hematite	0.128		16

Sands (2)	Reflectance 0.7-1.0 μm	Emissivities (1.8-2.7)μm	(3.0-5.0)μm	(8-13)μm	
Hainamanu silt loam	0.15	0.82	0.84	0.94	17
Barnes fine silt loam	0.21	0.58	0.78	0.93	17
Gooah fine silt loam	0.39	0.54	0.80	0.98	17
Vereiniging	0.43	0.56	0.82	0.94	17
Maury silt loam	0.43	0.56	0.74	0.95	17
Dublin clay loam	0.42	0.54	0.88	0.97	17
Pullman loam	0.37	0.62	0.78	0.93	17
Grady silt loam	0.11	0.58	0.85	0.94	17
Colts Neck loam	0.28	0.67	0.90	0.94	17
Mesita Negra	0.38	0.70	0.75	0.92	17
Dry grass	0.41	0.62	0.82	0.88	17

Mean of sands (2) above	Reflectance 0.32 ± 0.04	Emissivity 0.81 ± 0.02

4.8 Infra-Red Radiation from Vegetation

The vegetation cover of the terrain is not included in Watson's model and has to be treated separately due to its particular properties such as high moisture and semi-transparent nature.

Models which describe the temperature and energy transfer between vegetation and the atmosphere exist (18) but they are of more direct application to day-time rather than pre-dawn studies.

The emissivity of vegetation at wavelengths greater that 2.0 μm is of the order of 0.95 - 0.98 (19), almost equivalent to that of a black-body, but the temperature is a function of physiological factors in addition to albedo, emissivity etc. Dry vegetation lacks water and its emissivity is consequently considerably lower. (Dry grass Table 4.5 $\epsilon_{ab} = 0.82$ for $a \rightarrow b = 3.0 \rightarrow 5.0 \mu m$)

The physical characteristics of the vegetation such as leaf size, structure and surface texture will affect the emissive properties, as will the water content.

In order to withstand the harsh daytime environment, plants in semi-arid and arid regions have different reflectance properties from those normally seen (19). Instead of having broad leaves the plants tend to consist of thick fleshy stems/needles which contain the chlorophyll. The stems are opaque to visible and near infra-red radiation and, in order to maintain the amount of absorbed radiation (and thence the temperature of the plant) at a minimum, the plant reflectance is greater at all wavelengths than that of plants in less harsh surroundings. At night the effect of the needle-like leaves is for their surface temperature to approach the ambient air temperature due to the large surface area and lack of a canopy layer encouraging heat conduction rather than convection. High correlations between air and leaf surface temperatures have been found during the day (20) which lends weight to this arguement. Thus at night most of the vegetation

will be at a temperature approaching that of the air and the high emissivity will result in almost black-body radiation intensities. The differences between vegetation types will thence be very small assuming that the infra-red signal is due solely to the vegetation and not influenced by the terrain beneath.

The emissivity for dry grass (Table 4.5) is of interest as it represents the effect of extreme moisture stress and the change in emissivity from normal vegetation (15%) would make it detectable assuming that the effects from sands (whose mean emissivity is the same as that of dry grass) could be eliminated. Stresses are of importance in agricultural and 'wild' environments and stress types are listed in Table 4.6.

TABLE 4.6

Stress	Environments in which most important	Use when detected
Lack of water	Agricultural	Allows stress to be rectified.
	Wild	Enables soil types to be inferred.
Salinity	Wild	Speeds land reclamation.
Pollution	All	Can be used as a pollution monitor.
Minerals	All	Absence of essential minerals allows situation to be rectified.
		Presence of excess minerals leads to mineral exploration.
Biological attack	Agricultural	Situation can be monitored and rectified.

Within the context of thermal infra-red wavelengths the effects of stresses will be two stage. The first will be the breakdown of the normal physiological routine of the plant. This seems in most cases

to cause a decrease in the water content of the plant. The second stage is the onset of gross physical deformities such as changes in leaf colour, size, texture etc. The Australian study was concerned with the first stage effects where it was hoped that the semi-arid conditions would reveal stresses to the full as any adverse factor in addition to the harsh environment would send the vegetation into a highly stressed state. The manifestation of first stage stresses as decreases in water content results in them being greatest at noon or shortly after. This is the result ((17),p73) of both the migration of soil moisture downwards to the cooler regions and of the solar radiation being at a maximum. At night the reverse takes place and the moisture migrates to the now cooler surface layers of the soil and the absence of solar radiation enables the plant to some extent to overcome the stress conditions. Thus the detection of stressed vegetation is optimised by infra-red imagery obtained at, or soon after, noon.

4.9 The Results of Field Work Relating to the Effects of Solar Radiation on the Terrain

The field work carried out (2.2) resulted in some 20 days for which recordings were made of the surface temperatures of grass, soil, water and concrete from approximately 06.30 to 08.15 (sunrise was at ~ 07.00). Additionally, three sets of readings taken over several hours monitored factors such as ground, air and water temperatures. The meteorological data from Mt. Isa airport was also obtained so as to provide rainfall and air pressure readings over the time of study.

4.9.1 Monitoring of the Calibration Areas for the Infra-Red Linescanner

In addition to the monitoring of the temperature of the water in a swimming pool, the soil and grass on a playing field and the concrete of a tennis court, the dry and wet air temperatures and the position of the sun's rays on the ground were recorded as sunrise progressed and direct solar heating commenced.

The grass oval, tennis courts and swimming pool were within a few hundred feet of each other and the sun's rays touched the surface at 07.05 ± 5 minutes.

In order to determine whether the temperature of the ground was affected by heating of the atmosphere prior to dawn, the temperature changes just prior to 07.00 were tabulated (Table 4.7).

TABLE 4.7 Temperature Change of Targets Prior to Dawn

Temperature Change / Surface	Times Increasing	Times Decreasing	Times Same
Soil	1	9	6
Grass Canopy	7	7	2
Dry Air	6	4	4
Wet Air	3	5	6

The main trend was either stationary or decreasing temperatures, the magnitudes of the changes being less than 1° over 10 → 20 minutes. A more interesting and significant trend was seen when the mean daily 07.00 temperatures of the pool, soil, canopy and concrete were plotted over the days of recording (Figure 4.3). Each of the targets shows the same long term temperature fluctuation and this phenomenon must be due to the geographical location - the interior of the continent - where conditions are relatively stable. The greatest fluctuation is in the air temperature, but even so the targets can be ordered in terms of temperatures:

Swimming Pool:	$\theta^{\circ}C$
Ground:	$(\theta-5.0)^{\circ}C$
Air:	$(\theta-6.5)^{\circ}C$
Grass Canopy:	$(\theta-9.7)^{\circ}C$

FIGURE 4.3

GRAPH OF THE DAILY 07·00 TEMPERATURES FOR THE LINE-SCAN CALIBRATION AREAS FROM (26/APRIL → 13/MAY) 1971.

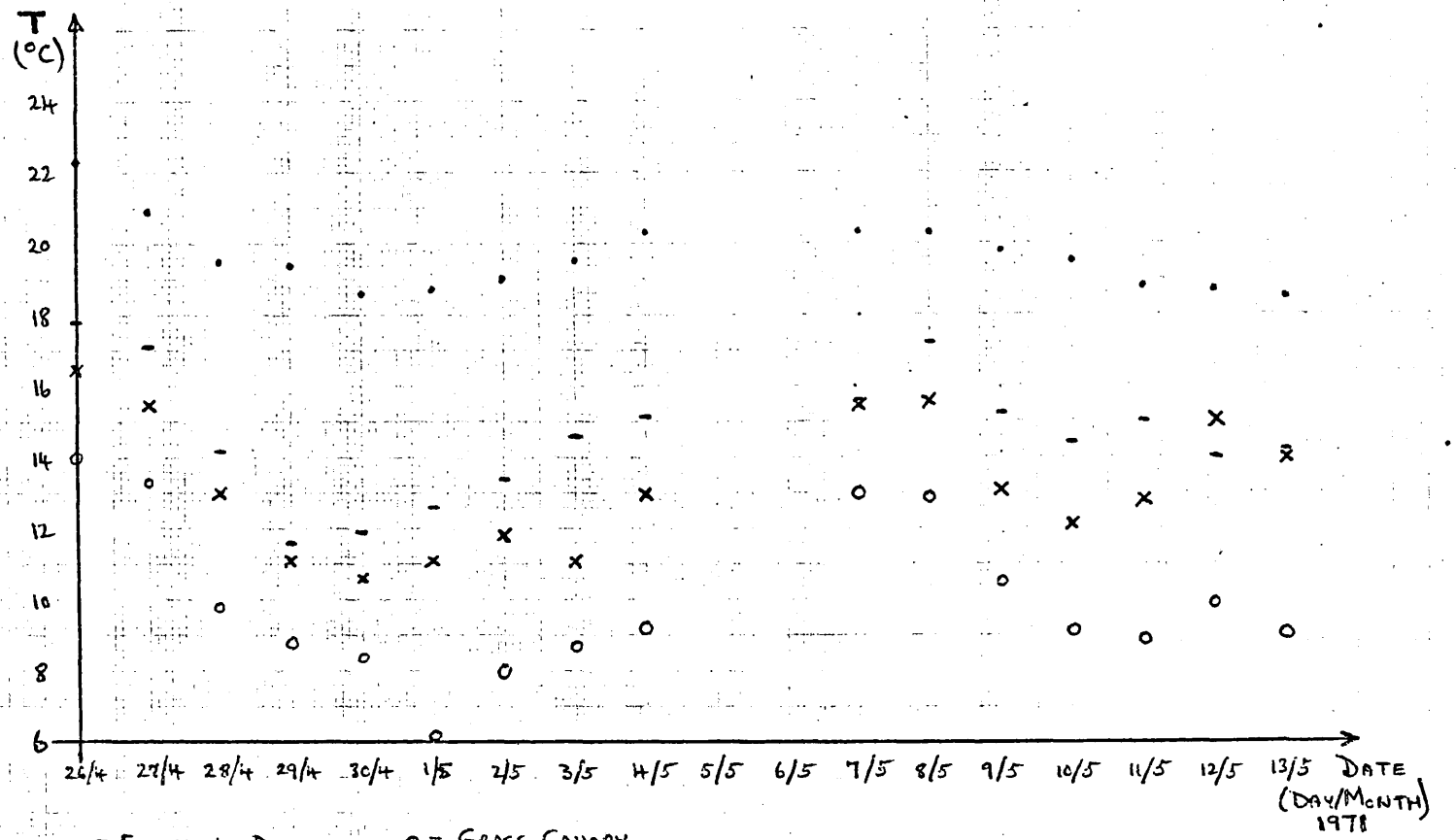

As the linescanning operations were at and after sunrise the calibration target temperatures were recorded continuously, from before the aircraft flew over on its way to commence operations until after it had passed over on its return flight to the airport. In this way 16 daily sets of readings showing the relative heating rates of the targets were obtained. A typical set is shown in Figure 4.4 (the 06.58 dry air temperature displacement from the mean is thought to be due to a recording error). The effect of thermal inertia is seen when the relative heating rates of the grass, ground and water are compared. Of interest is the cross-over of the air and ground temperatures as this will influence the surface moisture on the ground. The data from 16 days was averaged and equality of temperatures occurred at (08.09 $\pm$ 4 minutes) the increases in ground and canopy temperatures for equality being (0.7 $\pm$ 0.1)^{o}C and (5.4 $\pm$ 0.4)^{o}C respectively.

4.9.2. Field Measurements of Water, Rock and Vegetation Temperatures

Two large sets of measurements were made of the temperatures of water in a stream, a rock crevice, the ground and a triodia bush in the vicinity of the Dugald River lode (Fig. 4.10 and co-ordinates VC 120600 on Figure 4.31) where the field party camp was set up.

The results are presented in Figures 4.5, 4.5 whilst Figure 4.7 reproduces the region of sunrise at an enlarged scale.

Three river water temperatures were recorded for Figure 4.6, the average being presented in the graphs, as the variance was about 0.1^{o}C. The triodia bushes change shape with age, young plants being solid bushes, resembling a spiky hemisphere up to 1 metre in diameter whilst larger, older bushes die off in the middle resulting in an annulus of healthy vegetation surrounding the dead grey stems in the middle. The annular region can be up to 2 or 3 metres in diameter. The temperature readings were made on young healthy bushes and although they do not correspond to

FIGURE 4.4

TEMPORAL VARIATIONS OF LINE-SCAN CALIBRATION AREA TEMPERATURES

ON 11/MAY/1971

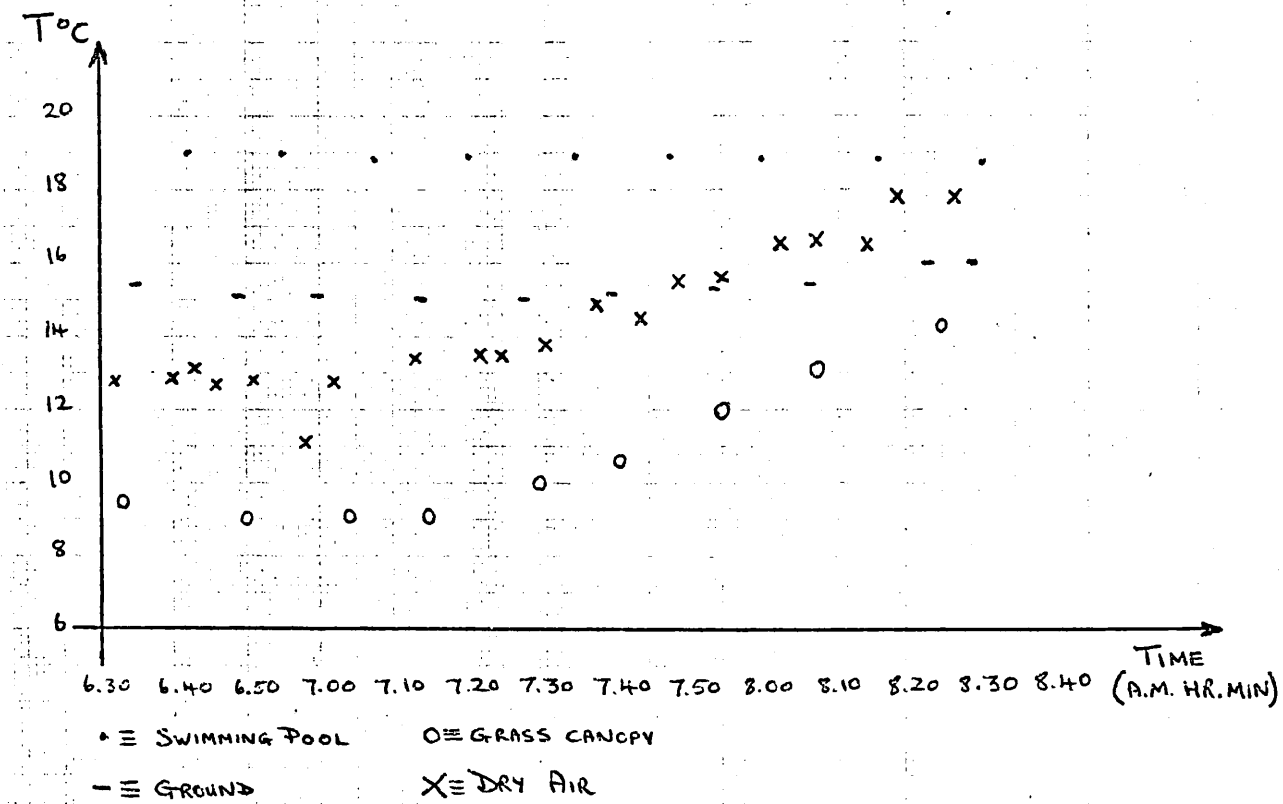

FIGURE 4.5

GRAPH SHOWING THE TEMPERATURE VARIATION WITH TIME FOR WATER, GROUND, AIR AND VEGETATION IN THE DUGALD RIVER LODE AREA. 9/APRIL/1971

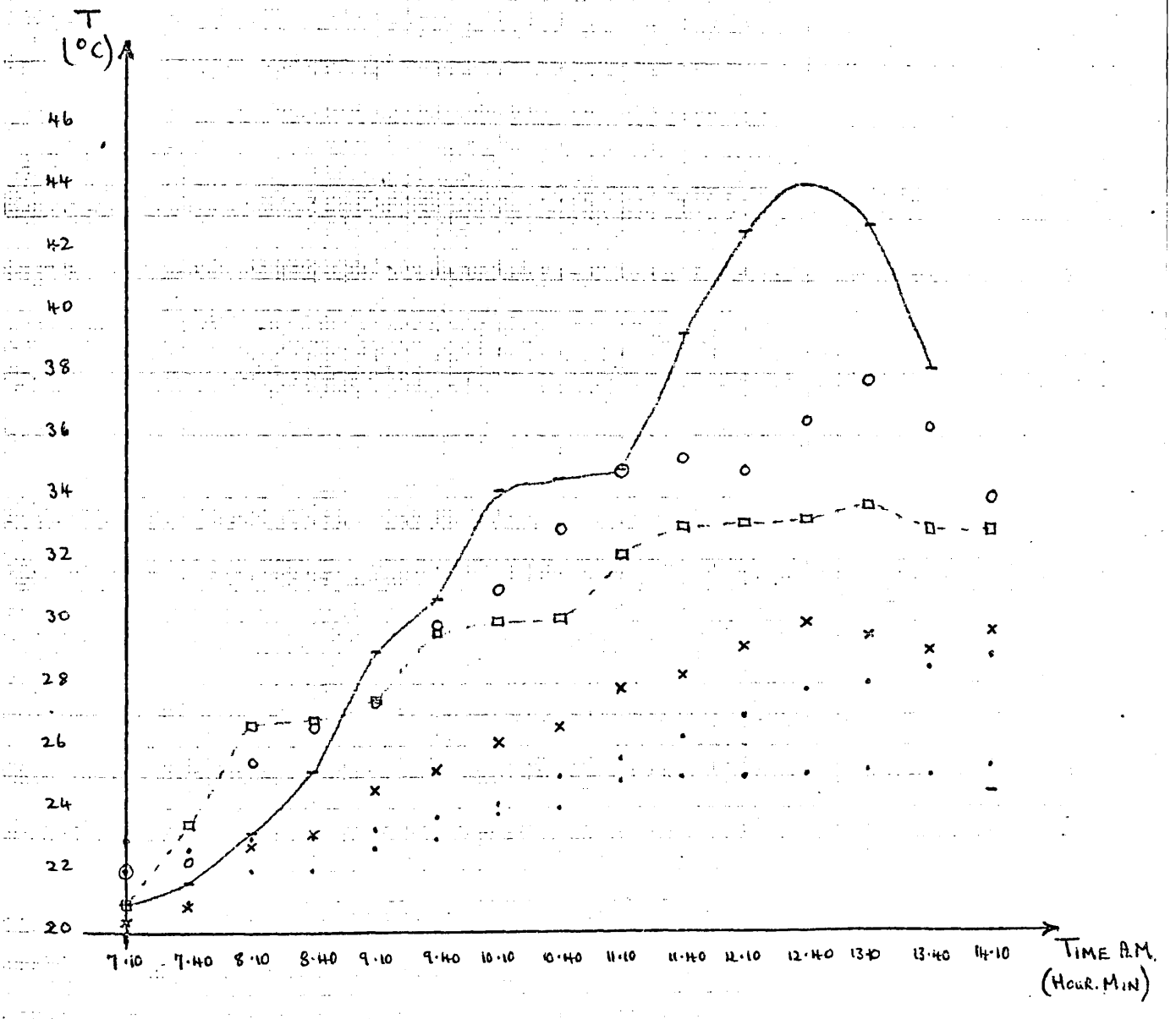

• = RIVER (2 READINGS)

O = TRIODIA BUSH (CENTRE)

– = GROUND (14·10 IN SHADE)

X = DRY AIR

□ = TRIODIA BUSH (SIDE TOWARDS SUN)

FIGURE 4.6

GRAPH SHOWING THE TEMPERATURE VARIATIONS WITH TIME FOR VARIOUS SAMPLES IN THE DUGALD RIVER LODE AREA. 15th + 16th MAY 1971

O ≡ TRICHIA BUSH
+ ≡ GROUND TO EAST OF LODE
X ≡ DRY AIR
— ≡ DRY HARD GROUND
• ≡ RIVER WATER
□ ≡ ROCK CREVICE

SEE FIG 4.7 FOR DETAILED 06·00 → 08·30 READINGS

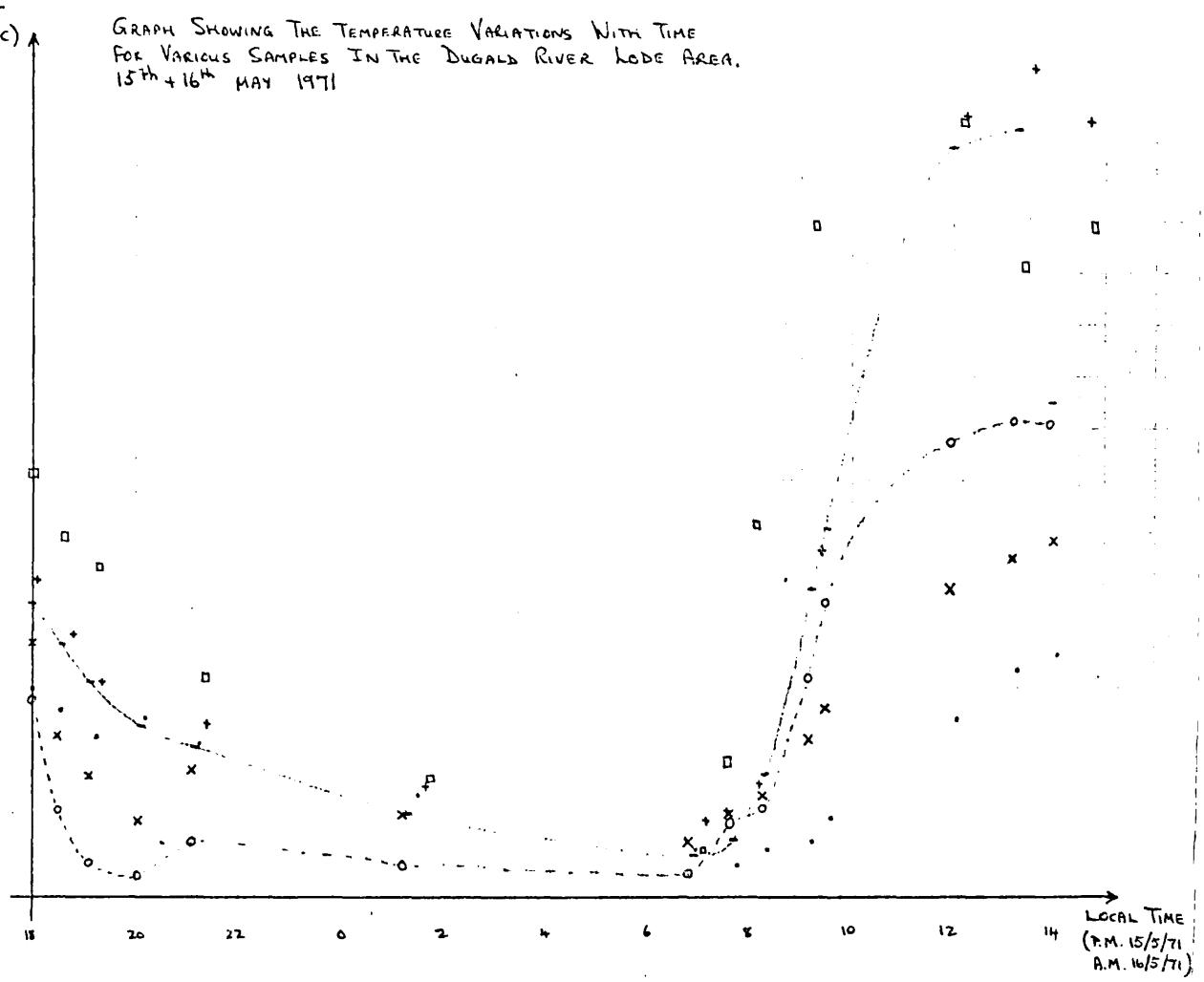

O ≡ TRICHIA BUSH X ≡ DRY AIR — ≡ DRY HARD GROUND (14·00 READING IN SHADE)
+ ≡ GROUND TO EAST OF LODE (SHALLOW SURFACE DEBRIS OVER SOLID ROCK) • ≡ RIVER WATER. □ ≡ ROCK CREVICE.

FIGURE 4.7

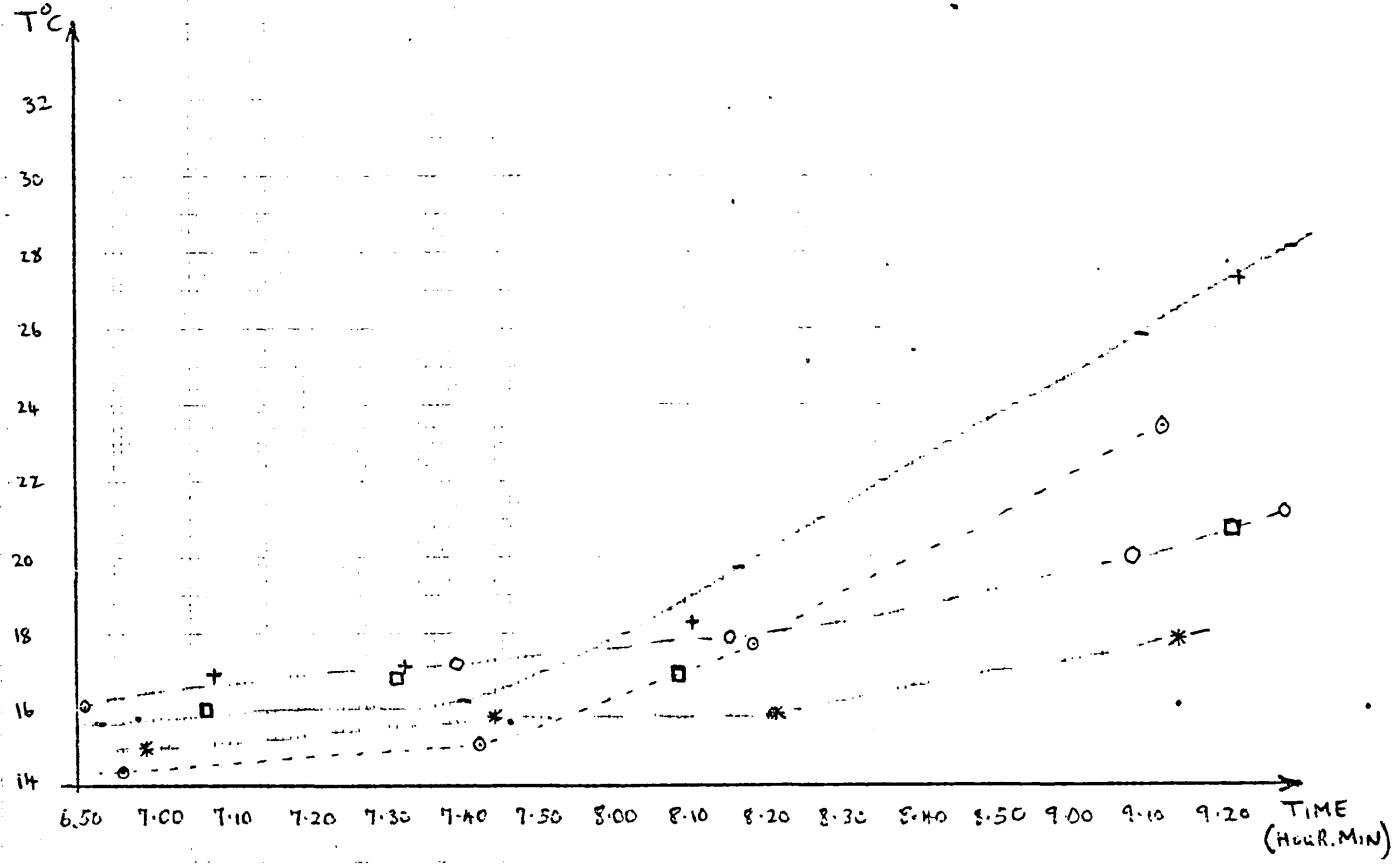

○ ≡ TRIODIA BUSH
\+ ≡ GROUND TO EAST OF LODE
— ≡ DRY HARD GROUND
* ≡ GROUND ON RIVER BANK
⊙ ≡ WET GROUND CLOSE TO RIVER

GRAPH SHOWING THE TEMPERATURE VARIATIONS FOR VARIOUS TARGETS IN THE DUGALD RIVER LODE AREA. 16TH MAY. 1971.

the surface temperature they do indicate the order and rate of change of temperature that the bush experiences. An interesting phenomena is seen in Figure 4.6 where a change in wind direction from W. t S.S.E. at 20.30 affected the air, triodia and water temperature readings.

Two spot readings were made of grass near to the Dugald River (Map, Fig. 4.31 reference VC 120600) on the 17th May 1971 at 07.22 when the grass was laden with dew and later on at 10.17 when the sun's rays had evaporated off the moisture. The respective temperatures were 10.1 and 31.0°C indicating the pronounced cooling effect of surface moisture. Dew was only observed in regions near to the Dugald River itself and not at the camp.

The relative pre- and post-dawn temperatures are shown in Table 4.8.

Thus from Table 4.8 and Figure 4.7 it can be seen that pre-dawn the temperatures are declining at a rate of ½°C per hour. At dawn the temperatures start to rise but for the first 15 - 20 minutes none of the target temperatures plotted crossed over each other. The pre-dawn temperature range was $\sim 3^{\circ}C$ ($7^{\circ}C$ if the dew laden grass is considered). By 07.50 the temperature range has increased to $\sim 4.2^{\circ}C$ and the relative temperatures of the targets have altered. This is of particular importance as it implies a tone reversal on the infra-red imagery.

4.10 Correlation of Observed Ground Temperatures with those Predicted by Watson's Model.

The predicted temperatures from the model, together with their associated variables are shown in Figures 4.8 and 4.9. A problem arose quite early on in the use of the model when, from comparison with ground measurements, it was found that wet sand was hotter at night and colder by day than dry sand, whereas according to the model its larger thermal inertia should make the inverse true.

TABLE 4.8 The pre-dawn and post-dawn temperatures as recorded in the vicinity of the Dugald River Lode Camp

TEMPERATURE (°C)	TARGET (06.30 - 07.00 Pre-dawn)	TARGET (07.30 - 08.00 Post-dawn)
10	Dew laden grass	
14	Wet ground near river	
15	Ground on river bank	River water
15.1		Wet ground near river
15.5	Triodia canopy	
15.6	Dry compact ground	
15.8	River water	Ground on river bank
16.2	Limestone	
16.8		Dry compact ground
17.0	Soil cover over limestone	
17.1		Soil cover over limestone
19.2		Limestone

FIGURES 4.8 (LOWER) AND 4.9 (UPPER) SHOWING THE SURFACE TEMPERATURE VARIATIONS WITH TIME FOR DIFFERENT MATERIALS, DERIVED USING WATSON'S MODEL.

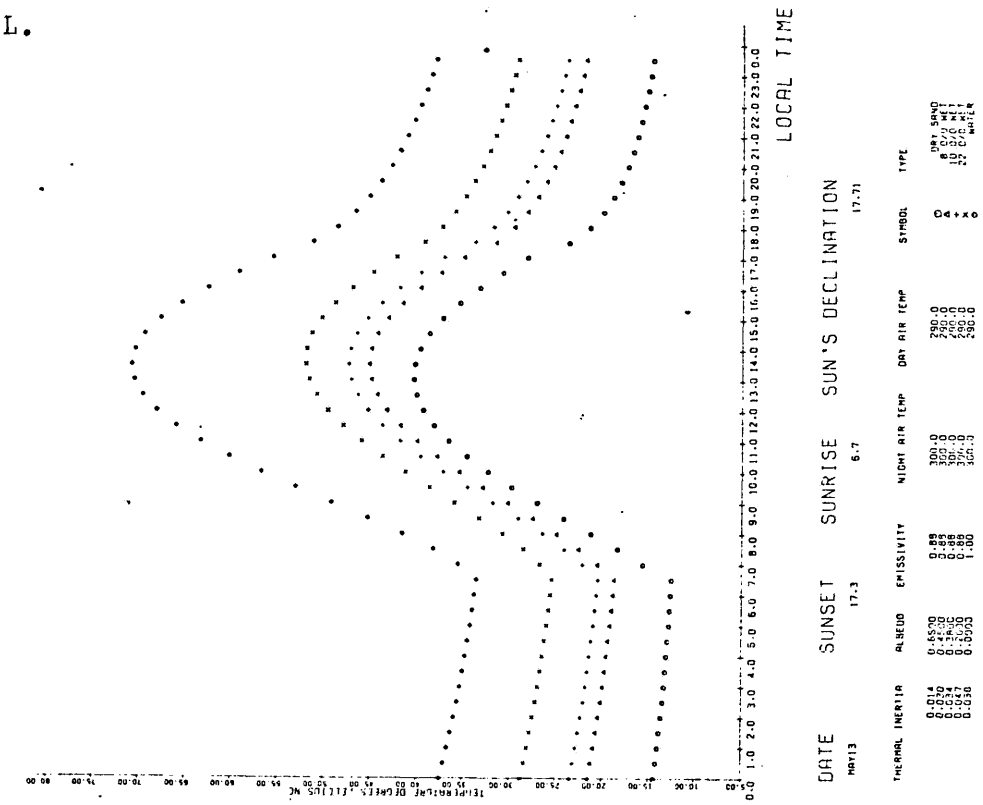

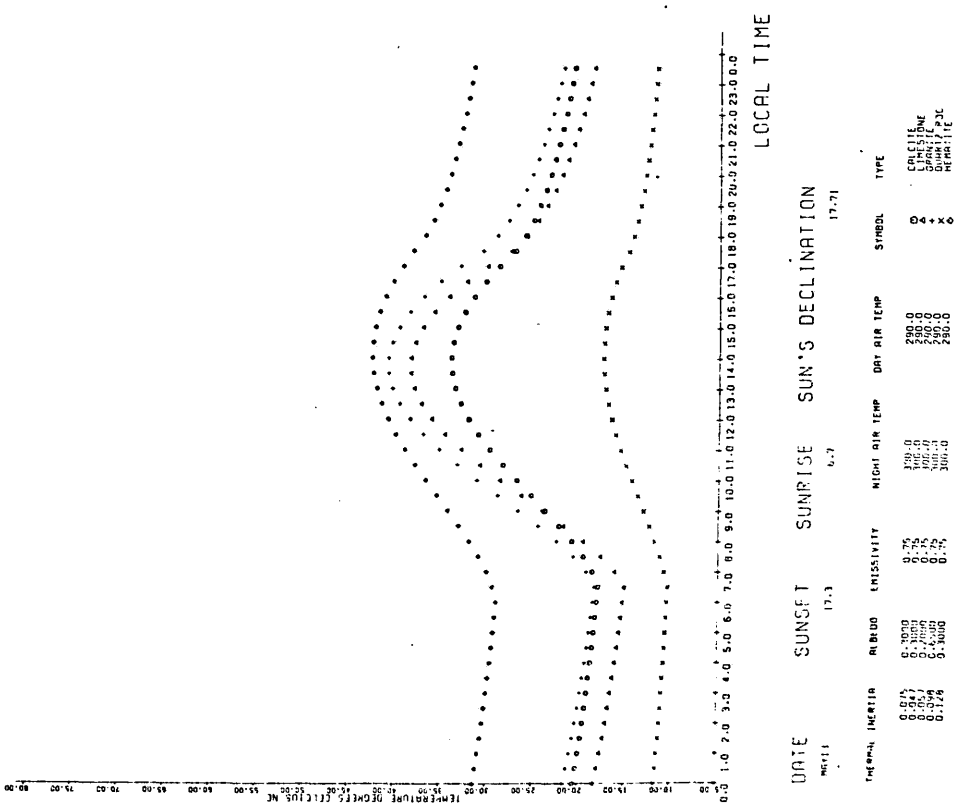

It was realised that the change of albedo and density with soil moisture, i.e. wetter soils and sands are darker and thus absorb more heat, had not been incorporated. Data on the variation of albedo with moisture content is extremely sparse, and the values finally used (22) related to Newtonian Silt loam; although this is not a sand the changes are probably of the correct order. The change of emissivity with moisture has not been incorporated as no data was available. The resulting curves showed agreement between the dry compact ground and dry/8% moist sand to within 1 or 2°C which is considered good in view of the deficiencies inherent within the model and already discussed. The temperature of the rock crevice differs considerably from that of the model and it is felt that the measured values could not have been representative of the surface temperature of the rock.

The terrain to the east of the lode consisted of a thin cover of loose soil and rocks overlying solid rock. This area is a good example of the difficulty of using the thermal model. The surface was a mixture of rocks of different sizes, textures and types. This varying composition means that the moisture trapped was undeterminable and hence the albedo, emissivity and thermal inertia for the area could not easily be determined. The solid rock near the surface would affect the heat conduction through the terrain and although all these factors could be incorporated into the model it is not readily feasible.

No attempt was made to derive a model to describe the temperature of vegetation in the time around dawn, mainly due to the dependence on air temperature discussed earlier.

In conclusion it was felt that despite its sophistications the model was not able to predict accurately the temperature of the terrain for a given target. Part of the failure lies in the inevitable variations in (i) cloud cover, and (ii) day and night air temperatures encountered in the field. More importantly, the

precise determination of terrain structure of a depth of 1 metre, surface albedo, emissivity and moisture was not sufficiently detailed. However, it is doubtful whether the amount of ground monitoring measurements required would warrant the time as the scale of the phenomena investigated in this study and seen on the imagery would require ground truth for quadrats with sides of 100 - 300 metres, a figure incompatible with a remote sensing survey. A discussion of the valuable role which infra-red linescan imagery and mathematical modelling could play is included in Section 4.13.

4.11 Linescan Replay and Correlation with Ground Features.

The EMI 'Airscan' system used on the survey did not have internal calibration facilities and it was decided to fly the system over a swimming pool, tennis courts and grass recreation ground before, ~ 06.30 and after, ~ 08.15 the scanning sortie. The temperatures of the three targets were recorded in situ and calibration was to be related to their respective grey tones on the imagery. Examples of the imagery over the calibration areas have been chosen and are presented in Figures 4.11, 4.12, 4.13, 4.14, 4.15, 4.16, to illustrate the problems to be discussed later on.

The offset voltage and gain of the system for each tape recorded (see section 3.7) was known and the video tapes were replayed so that the limits of the video signal corresponded to the limits of the dynamic range of the film being used (Ilford FP4). Each video tape was replayed at the optimum dynamic range and, in order that comparisons could be made between different tapes, a 'grey' scale, generated by feeding known step voltages into the replay system, was recorded at the start of each replay.

Calibration was attempted by measuring the densities of the calibration targets together with those of the step wedge and the film fog level with the Autodensidater described earlier. The target density readings were then scaled using the wedge reading so that

ERRATA; FOR FIGURE 4.10, SEE PAGE 101.

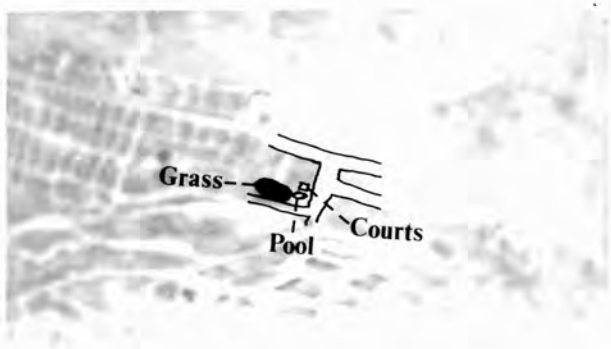
Grass
Courts
Pool

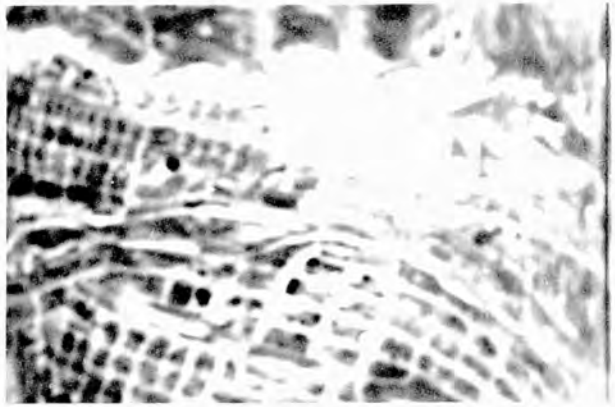

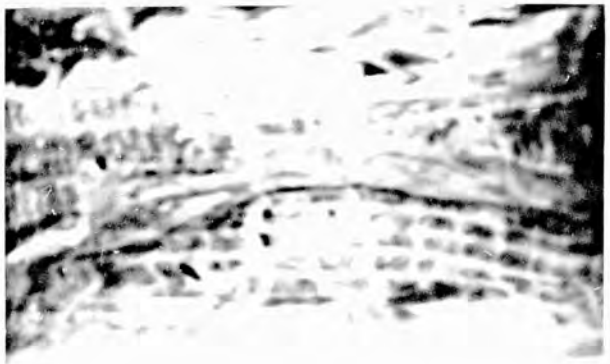

Figure 4.11
- with overlay.

Typical pre-dawn imagery.

Time; 06.50
Altitude; 4000ft.

Figure 4.12

Typical post-dawn imagery.

Time; 08.00
Altitude; 4000ft.

Figure 4.13

Worst example of imagery
(Targets barely visible).

Time; 08.00
Altitude; 4000ft.

Figure 4.14

Best example of line-scanner imagery.

Time; 06.50
Altitude; 2500ft.

Figure 4.15

Example of the effect of
aircraft roll on the line-scanner
imagery.

Time; 06.50
Altitude; 4000ft.

Figure 4.16

Example of line-scanner imagery gathered
over Derbyshire.

Time; 14.00
Altitude; 4000ft.

the changes in replay conditions were eliminated. The densities were measured for the days on which the offset bias, gain of the recording system and the cooling rate of the nitrogen to the detector were identical giving results for eight days out of a total of fifteen flown. The results are presented in Table 4.9 together with aircraft altitude, indicated air speed and the corresponding ground temperatures. The relative humidities enabled the attenuation to be obtained from Figure 4.2.1. These humidities obtained from the whirling hygrometer, and the pressures from Mt. Isa meteorological station, relate to ground level and the attenuations thus can only be treated as guides to the changes taking place. The waveband to which Figure 4.2.1 relates is from (2.8 to 5.8) μm including attenuation by the two water absorption bands centred at (2.7 and 6.0) μm and thus the attenuation is probably twice as great as that for the 4.5 - 5.5 μm band. The greatest daily attenuation change was only 1.8% although the long term change (late over-flight first day and early over-flight last day) was 10%. The effect of carbon dioxide attenuation for the two different flight altitudes (2,600 and 4,000) feet with a terrain height above sea level of 200 metres is seen to be $\sim$ 1%.

Although there was difficulty in locating the targets on some of the imagery (e.g. Figure 4.14) it can be seen clearly that the imagery lacked definition and the two flights on a given day over the targets yielded completely different tones although the temperature of the targets, especially the pool, had changed by very little e.g. Figures 4.11 and 4.12.

It was realised as soon as the imagery was replayed (in England) that the system of rotating mirror and parabolic reflector must have been out of focus as the imagery was of much poorer resolution (5 times) than that obtained in England, Figure 4.16. In some cases e.g. Figure 4.13, the signal was so large that the electronics were saturated and the response of the system slowed so that a ghosted image is seen in the direction of rotation of the mirror

TABLE 4.9 SHOWING THE DENSITIES OF THE LINE-SCANNED CALIBRATION TARGETS TOGETHER WITH THE PARAMETERS AFFECTING THEIR CORRELATION WITH THE MEASURED TARGET TEMPERATURES.

DATE Day	Month	TIME Hour.Min	FILM DENSITY (D) Pool	Grass	Courts	FILM WEDGE(D) High	Low	Base	TEMPERATURES(°C) Pool	Grass	Ground	Courts	AIRCRAFT IAS (Knots)	Alt.(ft)	HUMIDTY (Relative)	ATTENUATION *
4	5	6.35	590	188	610	1104	94	80	20.3	9.6	15.0	17.0	136	4000	89%	0.515
4	5	8.16	Not identified						20.3			22.0	136	4000	70%	0.521
7	5	6.58	945	645	917	1060	86	76	20.3	12.1	15.6	17.0	145	4000	70%	0.509
7	5	8.02	535	165	486	1048	128	83	20.3	13.7	16.4	17.6	140	4000	65%	0.500
8	5	6.35	850	290	870	1207	174	99	20.3	12.9	17.2	17.0	122	4000	68%	0.507
8	5	8.05	594	195	595	1183	120	94	20.3	14.6	17.4	20.0	137	4000	68%	0.507
9	5	6.30	875	336	650	1237	112	75	19.8	11.0	16.5	14.0	110	4000	69%	0.498
9	5	8.15	348	29	238	1212	109	80	19.8	14.7	16.3	18.4	141	4000	66%	0.504
10	5	6.47	894	247	710	1202	91	92	19.5	9.1	14.4	13.0	142	4000	64%	0.487
10	5	8.14	518	213	416	1226	104	96	19.5	13.0	15.6	17.2	146	4000	56%	0.485
11	5	6.29	1080	550	960	1201	100	95	18.8	9.1	15.2	13.8	121	2600	57%	0.478
11	5	8.22	678	297	630	1227	94	89	18.8	14.0	16.0	19.0	100	2600	44%	0.483
12	5	6.36	1060	321	877	1228	111	100	18.7	10.6	14.0	13.9	90	2600	54%	0.476
12	5	8.06	258	0	87	1210	109	101	18.7	12.5	14.4	18.4	90	2600	47%	0.483
13	5	6.29	813	239	726	1258	153	94	18.5	8.5	13.8	14.1	80	2600	50%	0.474
13	5	8.20	200	0	156	1473	164	90	18.5	13.2	15.2	17.0	104	2600	Hygrometer Broken	

*Attenuation was calculated from 4.2.1 using the relative humidity shown above
The relative humidity related to the air a few feet from the ground.
The error placed on the density readings was ± 10 units, the table of densities shown above is in units, 860units=1D
The size of the sampling aperture in the object plane was 0.1mm. across.

(in the case referred to, the signal from the swimming pool is ghosted across the recreation ground).

The difference in tones between the early and late overflights is felt to be due to the lack of resolution of the system blurring the calibration targets. Although the infra-red radiation relates to the surface temperature and this quantity is difficult to measure with a thermometer or thermistor, at least in the case of the swimming pool the top few millimetres which absorb and radiate the thermal infra-red radiation were measured. A compensating factor is that the temperatures of the targets were highly suited (maximum, middle and minimum tones seen on the imagery) to the exercise and had the system been focussed correctly their sizes would have been compatible with the resolution of the beam.

A plot of temperature versus scaled density is presented in Figure 4.16.1 for the inbound and outbound overflights and shows that although calibration curves can be constructed for each of them, the change referred to above is also clearly seen. The temperature used for the recreation ground was that of the grass as the cover was 100% and the emissivity is ~ 1, the same as that for water. Concrete has an emissivity of ~ 0.92 (23) and hence the error in equating radiances to temperatures is small in comparison with the total experimental error.

The calibration procedures are felt to have been proven despite the equipment failures. The targets chosen were suitable not only in terms of being sufficiently large with respect to the theoretical F.O.V. dimensions but also because their temperatures were representative of the extreme range of values encountered during the linescanning.

Future improvements suggested are to agree not only on the thermal but also the spatial resolution targets with the air survey team so that equipment performance can be checked in the field and also

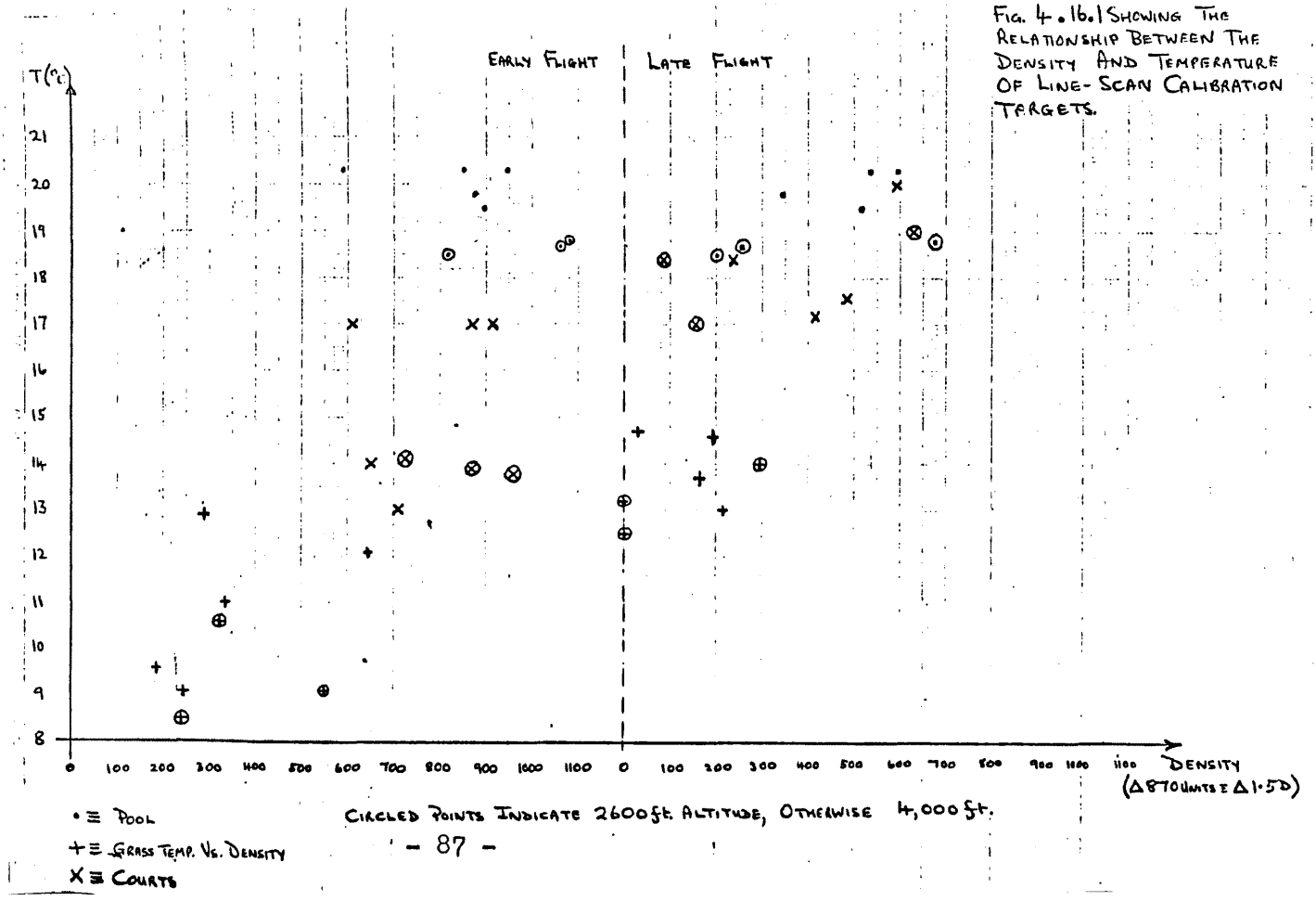

Fig. 4.16.1 Showing The Relationship Between The Density And Temperature Of Line-Scan Calibration Targets.

to use a hand-held radiometer to monitor ground emission (i.e. the black-body temperatures of the calibration targets). This would overcome the problems of measuring surface temperatures with a thermistor or a thermometer and the reading obtained is furthermore a directly related function of that detected by the linescanner. The temperature range of the area scanned was very low ($\sim 10^{o}$ at the most) and the thermal resolution of the linescanner ($\sim 0.2^{o}$) makes the use of video recording superfluous as the 50 levels ($10^{o}C/0.2^{o}C$) concerned can easily be recorded directly on to film provided that the average terrain temperature does not increase as the sortie progresses.

4.12 Interpretation of Linescan Imagery

The failure of the calibration exercise resulted in absolute assessment of the imagery, and thereby day-to-day comparisons being impossible. However, whatever the distortions in the system, the thermal contrasts are unaltered and this was the basis for their interpretation. The results presented are specific examples of general phenomena seen throughout the imagery.

The figures to be used are described below:

Figure 4.17 Geological map of the Dugald River area. The point marked 00, located within the box marked Dugald River Lode Area, corresponds approximately to the map reference VC 120600 on Figure 4.10. The scale of the map is shown on the right hand edge and is in feet. Figures 4.18 to 4.26 and 4.28 to 4.30 are infra-red linescan images and their overlays, detailed in Table 4.10.

Figure 4.27 is a photo-mosaic constructed from three consecutive, adjacent flight lines of the Panchromatic film with the yellow filter. The scale matches that of the linescan in the N-S direction.

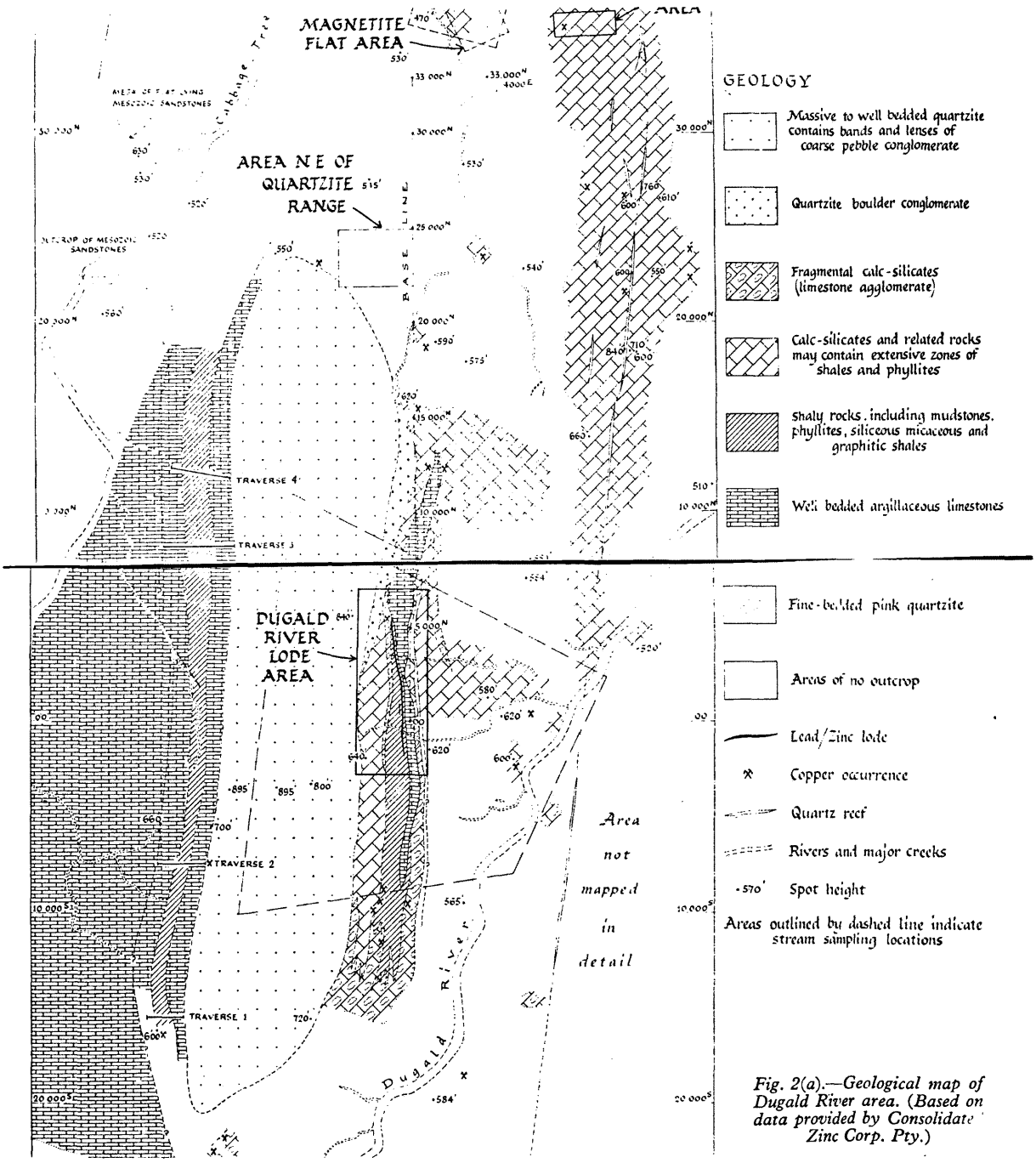

Fig. 2(a).—Geological map of Dugald River area. (Based on data provided by Consolidated Zinc Corp. Pty.)

FIGURE 4.18.1 OVERLAY TO FIGURE 4.18

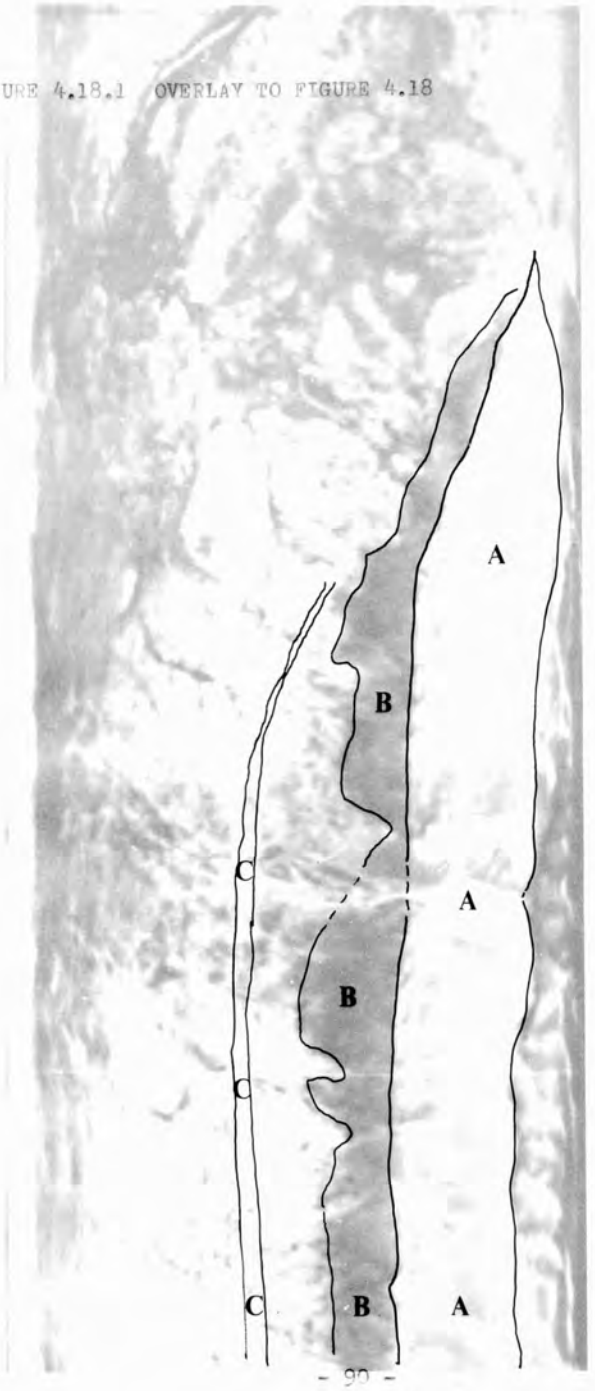

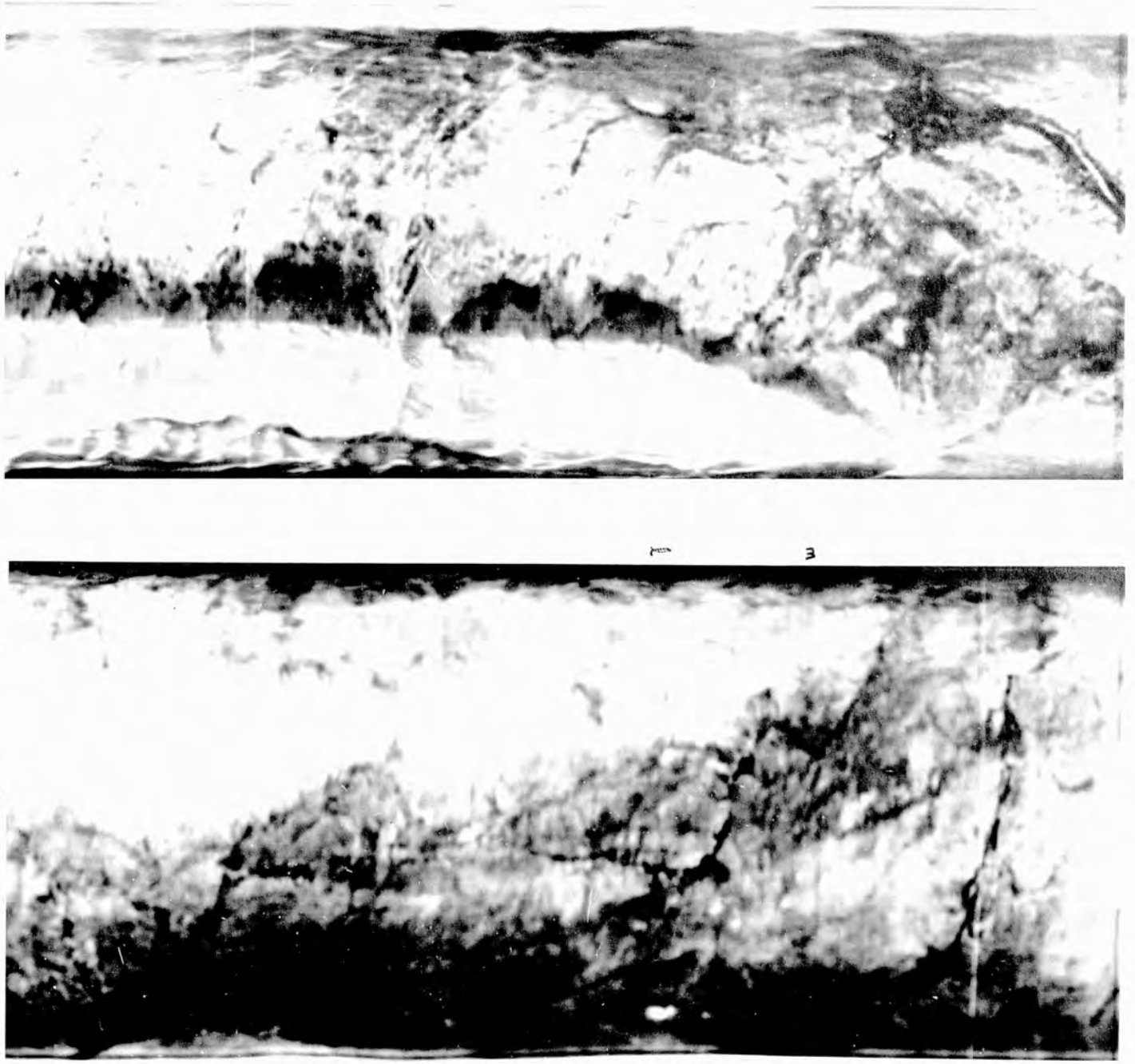

FIGURE 4.20.1 OVERLAY TO FIGURE 4.20

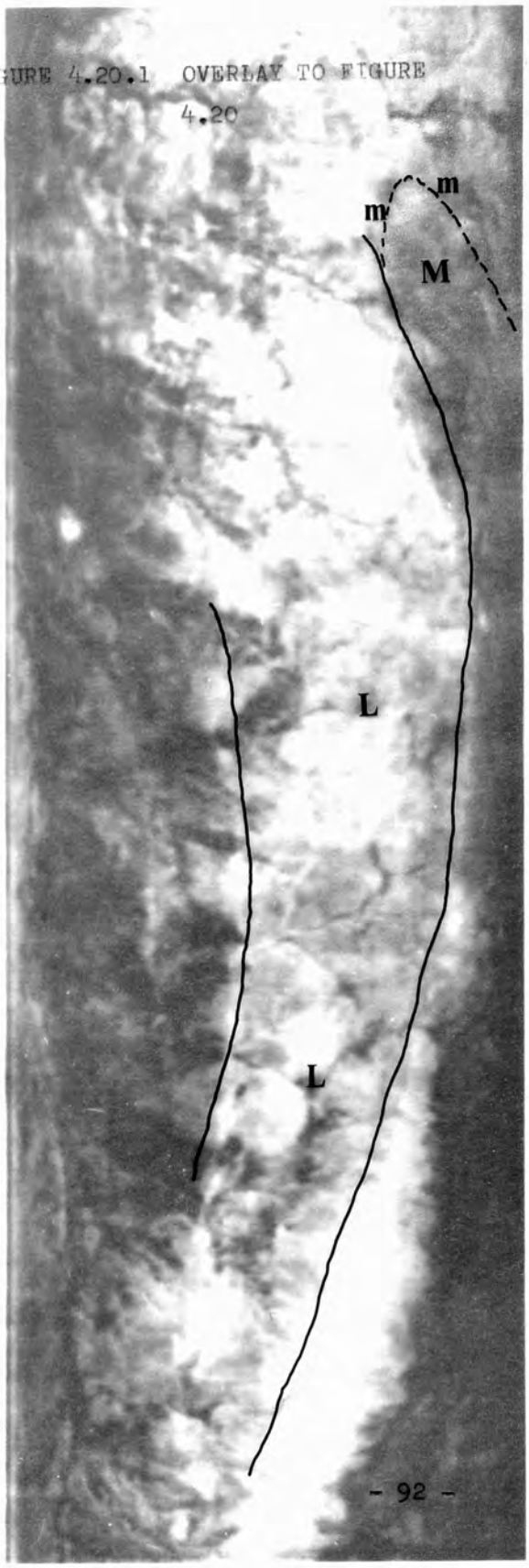

FIGURE 4.21.1 OVERLAY TO FIGURE 4.21

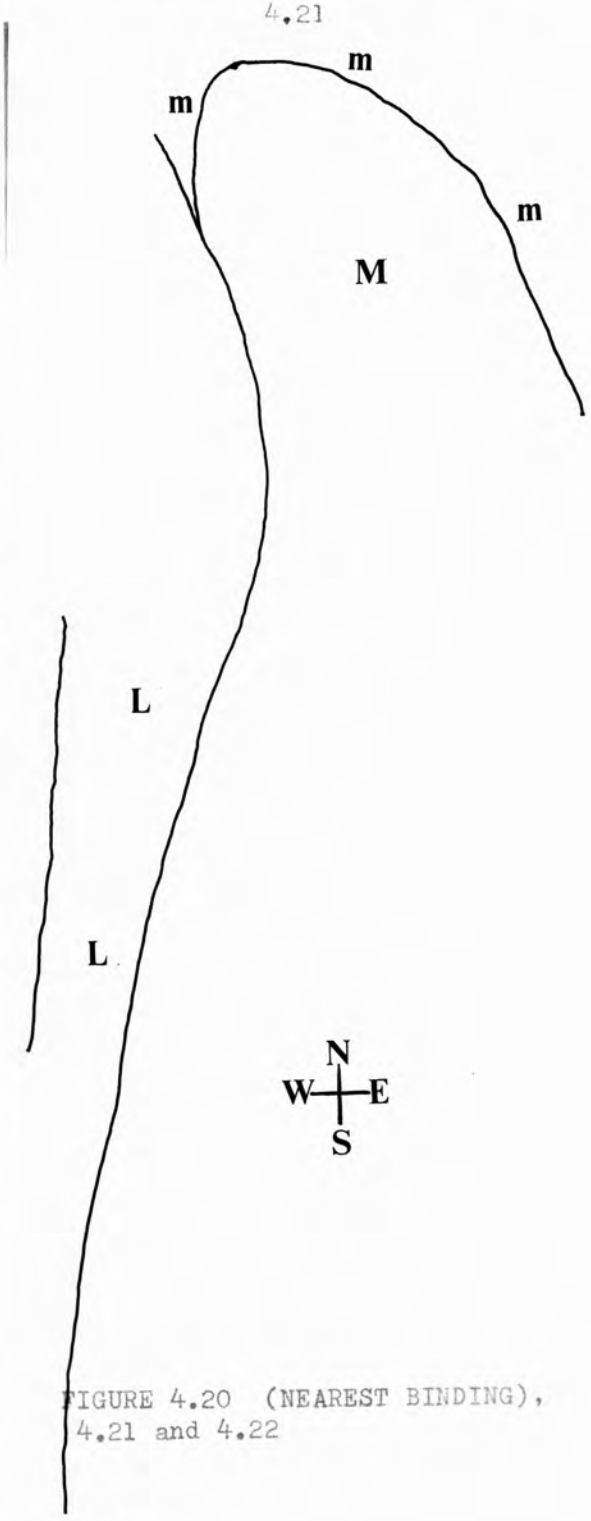

FIGURE 4.20 (NEAREST BINDING), 4.21 and 4.22

FIGURE 4.20 (NEAREST BINDING), 4.21 and 4.22

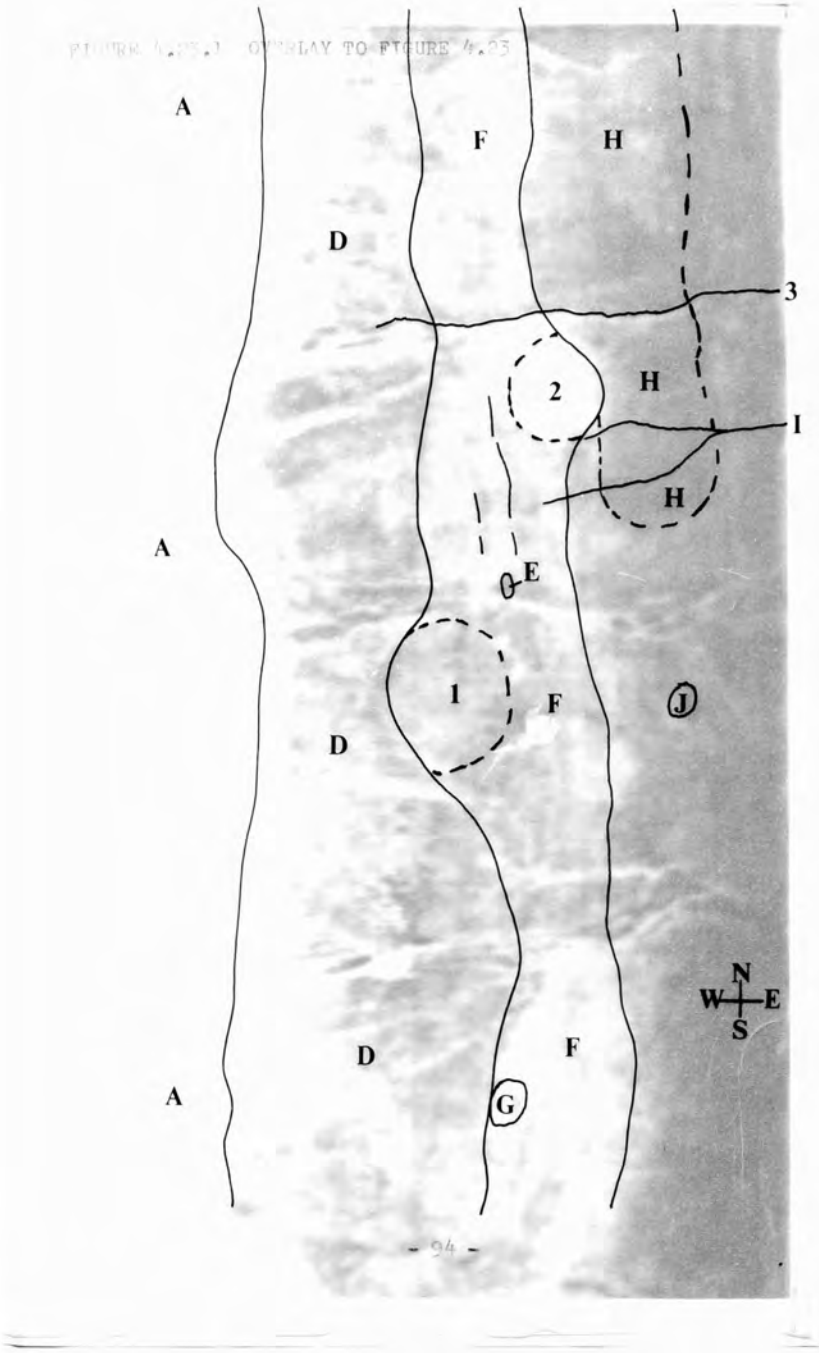

FIGURE 4.24.1 OVERLAY TO FIGURE 4.24

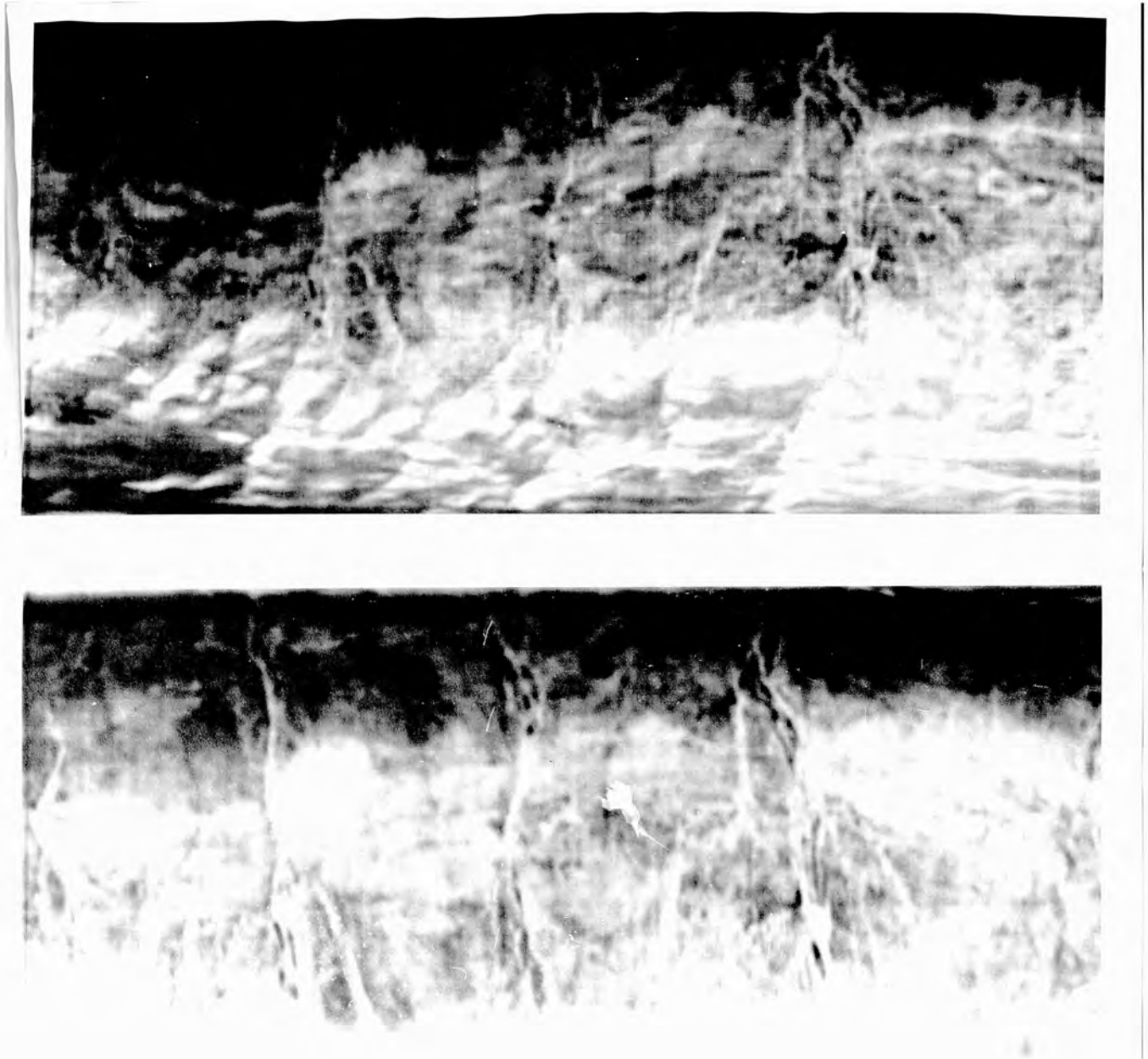


3
2
I
e
k
j
1
9
D 1K E G2F H J


3
e
1
A D 1 EF

TABLE 4.10 SHOWING THE TIME AT WHICH THE LINE-SCANNED IMAGERY WAS OBTAINED.

FIGURE NO.	TIME OF DAY.
4.18	07.50
4.19	07.15
4.20	07.25
4.21	07.40
4.22	07.50
4.23	07.05
4.24	07.15
4.25	07.30
4.26	07.50
4.28	07.05
4.29	07.40
4.30	06.45

FIGURE 4.27 PHOTO - MOSAIC OF DUGALD RIVER AREA.

FIGURES 4.28 to 4.31 - PAGE 100.

FIGURE 4.28 TOP LEFT HAND CORNER.

FIGURE 4.29 LOWER LEFT CORNER.

FIGURE 4.30 TOP RIGHT HAND CORNER.

FIGURE 4.31 MAP, LOWER RIGHT CORNER.

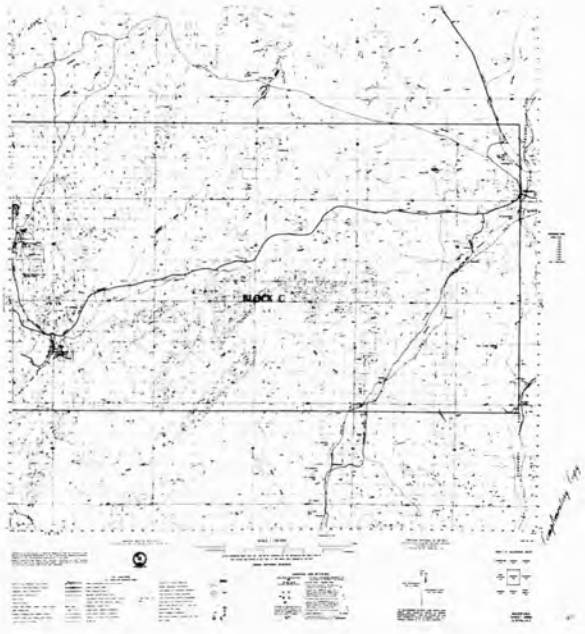
BLOCK C

FIGURE 4.10 TOPOGRAPHIC MAP SHOWING THE LOCATIONS OF BLOCKS A and B.

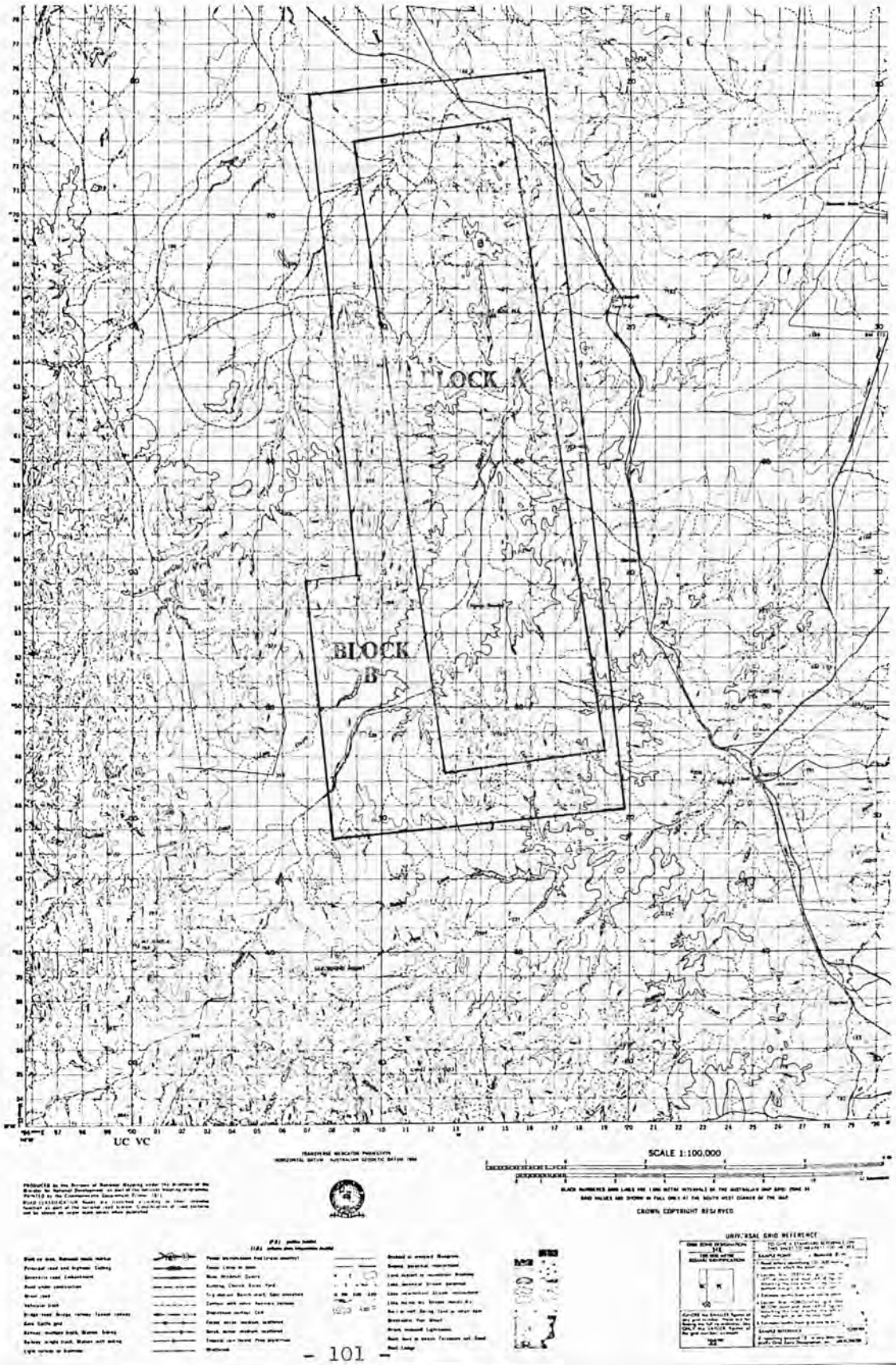

Figure 4.31 shows the approximate location of block C, although the block extends some 5 to 10 Km west of the edge of the map. Mary Kathleen is located on the western extremity of the map at ordinate UC 060.

The features discussed and areas referred to are located initially by means of an overlay and then by the corresponding lettered grid position. Thus feature E is located on the overlay, Figure 4.23.1 accompanying Figure 4.23 as E whilst on Figures 4.24, 4.25 and 4.26 it is found at grid reference eE.

The processing of the linescan imagery is such that increased emission of infra-red radiation leads to lighter tones on the imagery.

Feature A is a large, solid quartzite rock-range running approximately north to south with a maximum height above the surrounding flat terrain of about 250 metres and located on Figure 4.10 at map reference VC 100 540 to VC 100 660. The height of the range results in the uppermost parts being heated by solar radiation before the nearby ground, hence the intense white tones on the figure. However, the areas which were shadowed from the sun are still considerably lighter than the surrounding terrain and predawn imagery would have distinguished this feature.

Feature B, the dark band running the length of the western edge of Feature A, most probably corresponds to the argillaceous limestones. The sharp straight boundary between this feature and Feature A shows that the dark tone is not due to shadowing of the solar radiation by the range but it deserves a ground work investigation before it can be fully explained.

Feature C appears as two parallel light bands running due north and then turning abruptly north east. These are associated with

the shaly rocks and the fault, denoted by a line of ___'s and ??? 's shown on the geology map.

These features which are apparent despite the poor resolution and distortion of the system were found to be more readily distinguishable on the linescan imagery than on conventional black and white photographs.

Feature D, the region of darker tones to the east of the quartzite range corresponds to an area of calc-silicate rock types and is of particular interest because of the changes in thermal contrasts seen on successive images as time progresses and the terrain is heated. Initially (Figure 4.23) the dry stream beds, such as within area 3, running west to east appear as the lightest objects whilst the darkest correlate with areas of a more clay-type soil. Medium tones probably indicate the sub-surface rock structure. After several minutes the imagery (Figure 4.24) shows a higher overall thermal contrast in the Feature D region and although most of the relative contrasts are the same, some areas, e.g. 1, show subtle changes. Feature D is located on the most westerly edge of Figure 4.25 but the details observed show little change from the earlier imagery. Figure 4.26, the latest imagery of the feature, bears little resemblance to the others; Area 1 is now darker than the surrounds and a textured appearance has replaced the ephemeral qualities of previous images. The texture effect correlates with areas of tree cover and, it was noticed from the aircraft at about the time of this flight, that the sun's rays were illuminating the tops of the trees, throwing long shadows on the ground which would account for the speckled appearance. Within feature D all the stream beds except for that south west of feature E appear darker than the surrounds. Had the streams been moist, observations elsewhere would have predicted that they would appear initially dark and then lighten. A possible explanation is that the contents of the bed have been transported

from the higher western area and could be of quartz sand as well as calc-silicate matter, thus having different thermal properties from the immediate surrounding area.

Feature E corresponds to the topographic expression of the host rock associated with the lead-zinc lode but its appearance on all the imagery as a light tone with a dark tone on its immediate west side cannot be a shadow and could possibly be associated with the lead-zinc lode. Directly to the east of feature E, running north a total of about 3 cms. and $\sim$ 1.5 mm. wide and marked on Figure 4.23 is a dark line associated with the lead-zinc lode shown also on the geology map, Figure 4.17 and on Figure 4.27 as a light area devoid of vegetation. A similar dark line 0.7 mm. west of the first, 1.1 cms. long and broken in the middle is also seen on Figure 4.23. This corresponds to another lead-zinc lode known to exist but not marked on the geology map. Although the lode appears to manifest itself as a dark line on the imagery, it does not automatically follow that dark lines are lodes!

Feature F is the N-S band of lighter tones within which feature E is located and corresponds to the shaly rocks. The general N-S formation of the shales is clear but in some cases the exact boundary between them and the surrounding calc-silicates is not so obvious. Area 2 appears to be an associated shale region but the geology map implies that it is a calc-silicate. Such differences are bound to occur because the geologists will infer the underlying structure whilst the infra-red linescanner merely records incident radiation from the area. However, because the earlier scans showed the shales and the calc-silicates as different entities, areas such as 2 require further ground work. Feature F has slight topographic expression (3 $\rightarrow$ 10 metres) which is revealed by the differential surface heating shown in Figures 4.25 and 4.26.

Figure 4.27 shows that there is a strong geobotanical relationship over the northern two-thirds of feature F. The dark vegetation,

mainly triodia bushes, does not appear to have influenced the infra-red emission although area 2, which is devoid of vegetation appears lighter. In the vicinity of feature G, feature F is seen clearly in Figure 4.23 but hardly at all on Figure 4.27.

Feature G is visible on both the conventional photographs as a botanical and topographical expression and on the early linescans as a bright circle corresponding to the ring of high ground giving the feature a crater like appearance. The feature is degraded with time which implies that it is not due to solar heating which tends to enhance the topographic expression. Moisture trapped in the centre of the ring would account for the dark centre whilst shale or quartz rocks probably make up the 'crater' walls.

Feature H is seen on Figure 4.23 and 4.25 as a dark 'tongue' but its southerly extent is bounded by stream 3 on Figure 4.25, whereas it embraces feature I in Figure 4.23. There is no geological or straight photographic feature with which H can be correlated but the change in shape between Figures 4.23 and 4.25 suggests it is near to the surface and possibly due to moisture.

Feature I is more readily seen on Figure 4.25 where two stream courses and their merging point are surrounded by very dark tones. This feature is within feature H but is just resolvable in Figures 4.23 and 4.24. The feature is unusual as its appearance on the conventional photographs (Figure 4.27) suggests that many similar features occur elsewhere. However feature I is unique to the area of imagery inspected and, as Figure 4.23 was obtained much later than the previous images, the implication is one of completely different thermal properties from the surrounding terrain.

Feature J, a circular dark spot appears from a study of the true colour photography to be a clay area with a heavier constituency than the surround and thus more moist. Similar features were

identified elsewhere on the true colour photographs but, as with feature I, it appears as a unique object on the infra-red imagery.

Feature K (Figure 4.25 only) is a small fire lit at the field camp.

The features discussed below relate to the area of Mt. Rose Bee, a quartz ridge rising to about 250 metres above the surrounding level terrain. It is located on Figure 4.10 at map reference VC 140 660 and shown on Figure 4.17 in the north-east area as a series of quartz reefs running almost north in an area of calc-silicate rocks. The area is shown on four different sets of imagery, Figures 4.19, 4.20, 4.21 and 4.22, all of which show the gross lateral geometric distortions introduced by the scanning mechanism.

Feature L is the light toned area extending the length of the imagery bounded by the quartz ridges which, because of their topographic expression, have undergone solar heating and appear white. Of particular interest is the implication from the imagery that the whole of feature L is associated with the quartz and thus, if the geology map is correct, the depth of the shales is small.

Feature M, the region apparently composed of shales, has a very sharply defined boundary to the north-west which does not correspond with the geology map (however, the effects of surface debris may account for the discrepancy). Figure 4.22 shows at an enlarged scale the remarkable boundary between the quartz and the shales as well as the manner in which drainage patterns are revealed as dark dendritic features. Figure 4.28 was unfortunately enlarged with north and south directions reversed so that Features N and O appear reversed. However the area, located at map reference 123534 on Figure 4.10, contains the Dugald River running through it. Figures 4.28 and 4.29 were obtained at 07.06 and 07.37 respectively and show clearly the effects of moisture and solar

heating. Figure 4.28 shows large regions on either side of the river to be colder than the rest of the area as a result of evaporative cooling. However, 30 minutes later the solar radiation has effectively evaporated all the surface moisture and all regions, except for those in the immediate vicinity of the river bank, have reached the same temperature as the surroundings. Field measurements showed that dew laden grass was 4°C colder than dry vegetation as a result of evaporative cooling. The depression of the temperatures due to evaporation will never exceed that between a wet and a dry thermometer in the environment, typical values being between (1 and 9)°C.

Figure 4.30 illustrates the small scale geological structures seen on the imagery and contains a dyke running through the centre from the north north-east to south south-west as a dark line. At the lower edge, to the right of centre, the northern-most tips of Lake Corella are seen as light tones. The lake is located on Figure 4.31 at map reference VB 000 960 i.e. towards the eastern edge of the map and slightly south of centre.

Although the features discussed have topographic expression, there is a tonal banding associated with the different rock types which exists even where solar heating could not be present.

In Figures 4.28, 4.29 and 4.30, water bodies are easily detected as a result of their high thermal inertia which results in their being warmer than other objects at sunrise; the warmth dominating any evaporative cooling effects.

4.13 Conclusion

Operations at dawn led to high relief being shown due to the low sun-angle. Such information is of value to geologists but ordinary photography could provide the same results only more cheeply. Basic rock types were distinguishable and some mapping could be

performed on the imagery but the results were not entirely consistent and mapping would need to be carried out in conjunction with conventional aerial photography. Small scale interpretation showed most useful results when rock types were in areas with shallow overburden. In three cases where this occurred the overburden was "penetrated" and rock type boundaries seen. Lack of soil/rock profile information made interpretation difficult as the effects could have been due to the depth or characteristics of the overburden material. Even so, the information provided by the imagery could not have been detected on conventional photographs. In one or two cases dykes were seen but these represented a small proportion of the number known to exist.

Of considerable interest on the small scale interpretation was the appearance of areas with relatively high moisture levels. In the early morning imagery (i.e. up to 07.15) the moist areas dominated the imagery, revealing old drainage channels, moist valleys free of standing water and areas of moist soils and clays. The moisture resulted in the areas being cold due to evaporation, which is in direct opposition to the results predicted by thermal modelling or apparently seen on satellite imagery (24). The location and monitoring of moist areas in semi-arid regions could provide a valuable aid to the agricultural utilisation of such areas (24). The detection of water was shown to be very simple as its thermal inertia resulted in it being considerably warmer than all other targets prior to dawn.

The effects of solar heating were undesirable in terms of identifying rock types as the topography of the regions altered the apparent emission. However, features that were seen on pre-dawn imagery and disappeared in the 30 minutes after dawn can only be due to condensation on the surface or other surface/sub-surface phenomena. In the vicinity of rivers the effect was due to overnight condensation giving rise to evaporative cooling prior to dawn. Some 30 minutes after dawn the evaporation was complete

and the area quickly attained the ambient temperature of the surroundings. Away from the rivers, in regions of little vegetation cover, the changes seen which did not correlate with conventional aerial photographs were probably due to the constitution and moisture content of the sub-surface material. Extensive ground work is required before any direct correlation of the phenomena can be investigated.

The vegetation cover in the area was low and the emission from it blended in most cases with that from the background. The principal exception to this is in the post-dawn flights where individual trees effectively shielded a large area of ground giving the imagery a different texture.

The presence of tracks and other man-made objects in blocks A, B and C was not obvious except in the case of bitumen roads and a camp-fire. The implications of infra-red linescanners for locating either man-made or accidental fires is obvious.

In their present form, infra-red linescanners provide information related to the surface and sub-surface moisture conditions in semi-arid regions by their use prior to dawn. The differences in pre and post-dawn imagery may provide important and useful data on sub-surface composition but further ground work is required before unambiguous conclusions can be drawn.

CHAPTER 4 - REFERENCES

(1) HASE, H: R.S. of Environment, Mich. 7, 237, 1971

(2) DEIRMENDJIAN, D: Appl. Opt., 3, 187, 1964

(3) PEINDORF, R: U.S.A.F. Cambridge Research Centre, AFCRC-TN-55-206

(4) BAUER, E: Appl. Opt., 3, 197, 1964

(5) PLESSEY RADAR: E.S.R.O. Contract No. ESTEC 1673/72 EL Multi-Spectral Scanning Systems and their potential application to earth resource surveys, Vol. 1

(6) YATES, M.W. and TAYLOR, J.H: N.R.L. Report 5453, U.S. Naval Research Laboratories, 1960

(7) WILSON, R.A. Appl. Opt., 5, 899, 1966

(8) HAWKER SIDDELEY DYNAMICS INFORMATION SHEET (No other identification)

(9) McMAMON, H.O: J. Opt. Soc. Am., 40, 376, 1950

(10) BRUNT, D: Quart. J. Royal Met. Soc., 58, 389, 1932

(11) CARSLAW, H.S., and JAEGER, J.C: Conduction of Heat in Solids, Oxford, 1947

(12) JAEGER, J.C. and JOHNSON, G.H: Geogisica Pura E Applicata, 24, 104, 1953

(13) WATSON, K. et al: R.S. of Environment, Mich. 7, 2017, 1971

(14) REFERRED TO IN 13 BUT REFERENCE NOT STATED

(15) WATSON, K: N.T.I.S., Springfield, Va., U.S.A.

(16) N.T.I.S. DATA SHEET: No other reference

(17) N.A.S.A: Nimbus Technical Report No.2, Nov. 1971

(18) GATES, D.M: Remote Sensing in Ecology. Ed. P.L. Johnson, Athens, Georgia U.P., 1969

(19) GATES, D.M. et at: Appl. Opt. 4, 11, 1965

(20) WIEGAND and NAMKEN: Agronomy J., 58, 1966

(21) BEAUMONT, T.E.B: Personal Communications

(22) COULSON, K.L: J. Geophys. Res., 70, 4601, 1965

(23) PLESSEY RADAR: As for ref. 5, but Vol. II

(24) POUQUET, J: N.A.S.A. Report, TN D-4647

5 VISIBLE AND NEAR INFRA-RED RADIATION (0.4 - 0.9)μm

5.1 Introduction

The intensity of solar radiation at the earth surface is shown in Figure 3.2. The regions from (0.4 - 0.75)μm and (0.75 - 0.9) μm are termed the visible and near infra-red respectively and both are detectable by cameras with appropriate lenses, films and filters. The solar spectral radiance is at a maximum over these regions at the earth surface and it is convenient to treat them both as a single entity when considering the mechanisms of radiation transfer through the atmosphere, reflection by surfaces and detection with sensors.

5.2 Attenuation of (0.4 - 0.9)μm Radiation by the Atmosphere

The main attenuation is due to Rayleigh type scattering by the air molecules and water absorption.

Rayleigh scattering occurs when the radii (r) of the scattering particles (assumed to be spherical) are small compared to the wavelength, λ, of the incident radiation i.e. $r < 0.1\lambda$. The Rayleigh scattering coefficient per unit path length σ'_λ, is given by:

$$\sigma'_\lambda = \frac{32\pi^3 (n_\lambda - 1)^2}{3N\lambda^4} \qquad 5.1$$

where n_λ is the refractive index of the atmosphere (~ 1) and N is the number of particles/unit volume.

The transmissivity, q_λ, of the atmosphere is defined as the fraction of energy transmitted through a Rayleigh Atmosphere. Values of σ'_λ and q_λ calculated for a vertical path through the earth's atmosphere for different values of λ are given in Table 5.1.

TABLE 5.1 (Ref. (1))

Showing the variation of Rayleigh scattering coefficient (σ_λ) and transmissivity (q_λ) of the atmosphere with wavelength.

Wavelength (microns)	σ_λ ($\times 10^8$)	q_λ
0.30	152	0.295
0.40	45	0.696
0.50	18	0.865
0.60	8.6	0.933
0.70	4.6	0.964
0.80	2.7	0.979
0.90	1.7	0.987
1.00	1.1	0.991

In areas away from large expanses of water the constituents of haze have been shown by Diermendjian (2) to have radii of the order of (0.02 - 0.05) μm and thereby to contribute strongly to Rayleigh scattering. The attenuation by water vapour occurs at (0.75 and 0.94) μm with absorptions of $\sim$ (20 and 50)% and absorption band widths of (0.01 and 0.03) μm respectively for a vertical path through a typical atmosphere containing 2.0 cms. precipitable water vapour. Hence within the region of the spectrum from (0.4 - 0.9) μm only slight absorption will be experienced at 0.75 μm

The amount of atmospheric attenuation encountered will vary with changes of haze concentrations in the atmosphere and also with time as the path length of solar radiation varies.

The area of Australia chosen for the study was one where the effects of haze and water vapour were small and, by restricting the aircraft operating times and altitudes, changes in attenuation should have been minimal. Similarly, narrow angle lenses ($\pm$ 20° from

the nadir to the effective frame edge), limited the attenuation across the photographs due to varying path length.

5.3 Reflectance of Radiation by Terrestial Objects

At the surface of an object the incident radiation is reflected, absorbed and transmitted to varying degrees depending upon the surface properties of the object. Thus the reflectance mechanism for a rock, which is a surface effect, differs considerably from that of vegetation where the surface is semi-transparent and internally scattered radiation is a sizeable proportion of the observed reflected radiation.

In the general case light will undergo reflection and absorption at the surface, the reflection being both specular and diffuse (bi-directional) their relative proportions being a function of surface characteristics such as texture.

Specular reflection is characterised by the reflection of light by a mirror - i.e. angle of incidence = angle of reflection - and a parallel beam remaining parallel after reflection. However the intensity of diffusely reflected radiation obeys Lambert's law and is therefore equal in all directions. The reflectance by surfaces which are specular, diffuse and a mixture of the two (the more typical case) is shown schematically in Figures 5.1, 5.2 and 5.3 where the dotted line represents the amplitude of the intensity vector from point O.

Figure 5.1 Specular Reflection:

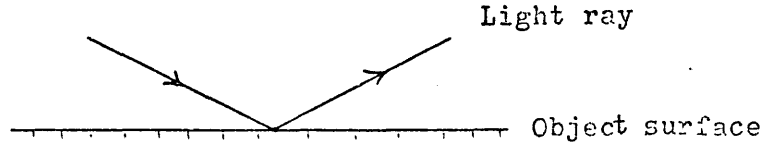

Figure 5.2 Diffuse Reflection:

Figure 5.3 Specular and Diffuse Reflection:

The intensity of the specularly reflected component is derived by considering the incident radiation resolved into components normal and parallel to the object surface.

The ratio of the amplitudes of the reflected ray to the incident ray in the plane normal to the surface (R_r) and parallel to the surface (R_l) are given (3) by:

$$R_l = \left\{ \frac{\tan (I - I')}{\tan (I + I')} \right\}^2 \qquad 5.2$$

$$R_r = \left\{ \frac{-\sin (I - I')}{\sin (I + I')} \right\}^2 \qquad 5.3$$

where I and I' are the angles of incidence and refraction respectively and are related by Snell's law:

$$n \sin I = n' \sin I' \qquad 5.4$$

and where n and n' are the refractive indicies of the incident and refractive/reflective media respectively.

Thus the changes in intensity and polarisation ($\Delta R_{\perp} \neq \Delta R_{+}$) of the specularly reflected ray can be predicted given the refractive index of the object.

5.4 Reflection of Radiation by Soils and Rocks

The reflectance properties of soils and rocks have been studies in great detail and are documented in the form of reflectance curves from the visible to mid infra-red wavelengths (4). The spectra refer only to normal incidence measurements and do not indicate the specular and diffuse components which are related to the texture and composition of the soils and rocks. Soils can be considered as being made up from varying proportions of sands, silts and clays with the average diameters of individual particles varying from 2mm.- 0.06 mm; (4 - 60) 10^{-3}mm. and less than 4.10^{-3}mm. respectively.

Some attempts have been made to construct a model of the manner in which light is reflected by soil based on the scattering from the individual soil particles.

The surface layer of the soil can be considered as a matrix of individual particles where the amount of light reflected directly by them, as opposed to being scattered into the inter-particle spaces, is a function of the surface structure.

Figure 5.4

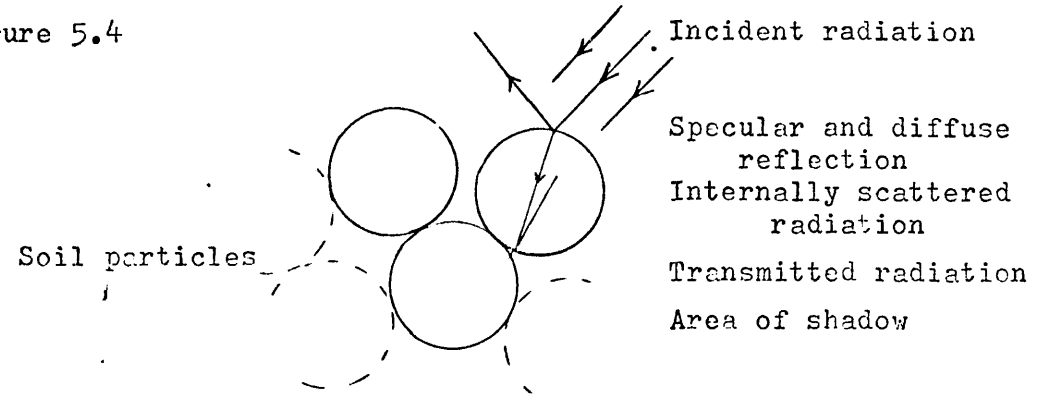

The changes in particle size result in differing amounts of areas of shadows etc. Whilst large sized particles reflect light at the surface and the colour seen is a surface effect, small particles which scatter the light into and from the top layers of the soil exhibit a different colour, termed body colour.

For larger particles surface reflection will dominate and Coulson (5) has shown that a model with Mie scattering and the shadowing effect shown in Figure 5.4 can produce good correlations with field measurements, implying that the speculary reflected component is negligeable. The variations of intensity with different angles of incidence and observation are also given and for the present study the changes in reflectance would be of the order of 2% across the photograph due to the $\pm 20^{\circ}$ look angle of the lenses. Similarly the combination of near mid-day photography with relatively narrow angle lenses reduces any polarisation effects, which might inadvertently be obtained, to a negligeable level.

The infusion of water into the inter-particle spaces affects the soil reflectance as a result of the water/soil particle interface and the associated refractive indicies. For a given value of I, from equation 5.4 the corresponding value of I' will be greater for the water/soil refraction and thus from 5.2 and 5.3 R_r and R_l will decrease.

However, the decreases in R_r and R_l will be different so not only will the total reflectance decrease but also the degree of polarisation will change. Water absorption bands appear as the moisture content increases, but their wavelengths (1.45 and 1.60)μm are outside the range of normal photographic systems.

Measurements by Conduit (6) on the reflectance spectra of 160 soils showed that four basic types were present within the samples taken and that an individual could be classified as a particular type on the basis of four reflectance readings taken between (350 and 1,000)nm. The soils were monitored under laboratory conditions with uniform moisture levels thus giving a measure of the difficulties likely to be encountered in the field.

The reflectance spectra from rocks are more predictable than those from soils due to the less variable nature of the surfaces involved as a result of climate etc., and are also documented (4).

5.5 Reflection of Radiation from Vegetation

The principal vegetation reflecting surface is the uppermost leaves of the canopy or, in the case of desert plants, the thick stems which are their equivalent of leaves.

Leaves of deciduous vegetation are semi-transparent whilst desert plant stems and evergreen leaves are generally opaque, although in all cases the concept of body colour referred to earlier (5.4) is of importance as the solar radiation penetrates between (10 and 100)μm below the surfaces of the leaves.

The effective reflectance of vegetation as measured from a distance is a function of the density of the canopy, the orientation of the leaves within the company, and the reflectance properties of the leaves themselves.

The general arrangement of the leaf, with cells of walls which are of hydrated cellulose and spaces filled with water, air and structures approaching the wavelength of the incident (0.4 - 0.9) μm radiation results in a high degree of multiple reflection of the longer wave (0.7 - 0.9) μm radiation which is not absorbed within the leaf. Figures 5.5, 5.6 and 5.7 (13) show the relationship between water absorption and leaf absorption; the effects of different moisture levels and the difference in reflectance spectra between corn and soya beans respectively. All the figures show the increases in reflectance at (0.53 and 0.74) μm as a result of the presence of chlorophyll and multiple scattering respectively.

5.6 External Factors Affecting the Reflectance Properties of Vegetation

Leaf maturity is the most important factor affecting leaf reflectance and is treated as an external effect because it is directly related to the local environment in which the vegetation is found. The reflectance spectra from a vegetation canopy alters with maturity not only as a result of changes of the vegetation but also as a consequence of different proportions of vegetation and underlying terrain occupying the field of view of the sensor.

Blight and insect infestation alter the physical characteristics of the leaf (size and texture) and the reflectance effects associated with leaf decay are seen.

Increasing water moisture content decreases the reflectance of vegetation (7), the change in the reference quoted being typically of the order of +3% in the percentage reflection at 0.55 μm which was 11%.

The effects of moisture stress on corn leaves are shown in Figure 5.6 but it appears that the samples were taken from corn

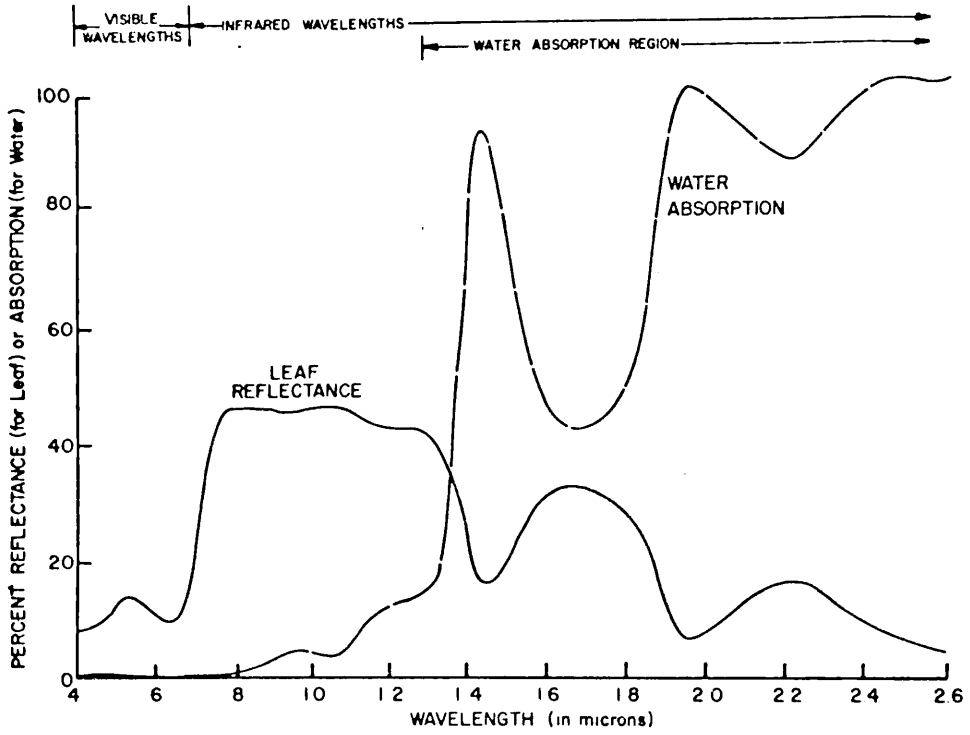

Fig 5.5 Relationship between Leaf Reflectance and Water Absorption in the 0.4-2.6μ Wavelength Region.

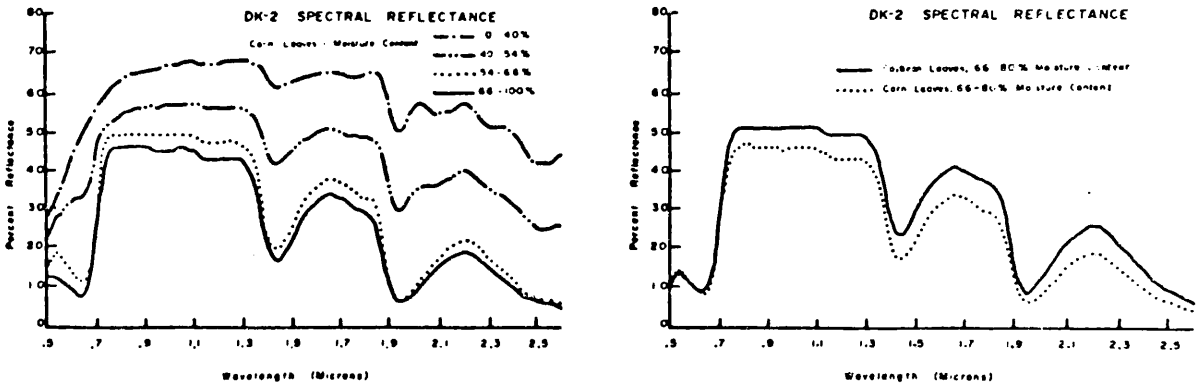

Fig.5.6 a. Corn Leaves at Four Moisture Levels. 5.7 b. Corn and Soybean Leaves at the Same Moisture Level.

Effects of Differences in Moisture Content on Leaf Reflectance Spectra.

in different states of maturity and the changes may not be due entirely to moisture content.

Mineral toxicities have been seen to affect the reflectance spectra of vetetation (8), (9), (10) and are more fully discussed in Chapter 8.

Whilst it is possible to induce the stresses of blight, water content and mineralisation into vegetation under laboratory conditions, in nature the stresses build up over a period of time and also manifest themselves indirectly as changes in maturity or growth vigour.

5.7 The Detection of Visible and Near Infra-Red Radiation

The present study made use of photographic systems to sense the (0.45 - 0.9) μm radiation but multi-spectral scanners (see section 3.3 for a description of a single detector scanner) have found favour where the information needs to be absolutely calibrated and/or transmitted over a data link.

The lower wavelength limit of photographic systems ($\sim 0.4\ \mu m$) is imposed by the severe Rayleigh scattering of radiation by the earth's atmosphere whilst at $1.0\ \mu m$ not only do the film and lens characteristics show a rapidly declining sensitivity but also the extra information gained over that sensed at $0.9\ \mu m$ is minimal.

The films used in the Australian section of the study are shown in Table 2.1 together with their relative speeds and resolutions.

Conventional colour films tend to be termed 'true-colour' films whereas infra-red sensitive colour films which record green objects as blue; red objects as green; and infra-red (reflecting) objects as red are referred to as 'false-colour' films (11).

The sensitivities of the layers on the colour films - Figure 2.1 - are such that each film senses three wide wavebands, although a yellow filter is used in conjunction with the false colour film where the infra-red layer needs to be shielded from the blue light to which it is also sensitive. After processing, the dyes associated with the colour sensitive layers are such that each waveband sensed can be 'extracted' by the appropriate primary filter - see Table 5.2 and Figure 2.2.

TABLE 5.2 Showing the waveband extracted from the colour films with a particular primary colour filter

Filter Used	Film Type	True Colour	False Colour
Blue		Blue	Green
Green		Green	Red
Red		Red	Infra-Red

In the case of the black and white PanF films the light was filtered before it reached the emulsion using Wratten Green and Yellow filters - the latter resulting in red and green radiation being recorded.

The bandwidths of the regions sensed were consequently a few 100's of nanometres with ill-defined cut-offs ((12) and Figure 2.1). Narrower bandwidths with sharper cut-offs are obtainable with interference filters - see Appendix A - but the bandwidths of ~ 15 nm would have resulted in a severe loss of resolution as a result of the very high speed films required.

5.8

CHAPTER 5 - REFERENCES

(1) PENNDORF, R: U.S.A.F. Cambridge Research Centre, AFCRC-TN-55-206

(2) DEIRMENDJIAN, D: Appl. Opt., 3, 187, 1964

(3) LONGHURST: Geometrical and Physical Optics, Longmans, 1964

(4) N.A.S.A: Earth Resources Spectral Information System

(5) COULSON, K.L: J. Geophys. Res., 70, 4601, 1965

(6) CONDUIT: Photogrammetric Engineering, 955, 1970

(7) WARD, J.H: R.S. of Environment, Mich. 6, 1205, 1969

(8) YOST, E. and WENDEROTH, S: R.S. of Env. Mich. 7, 269, 1971

(9) HOWARD, J.A: R.S. OF Environment, Mich. 7, 285, 1971

(10) PRESS, N: B.I.S. Symposium, April 1973, London

(11) NATIONAL RESEARCH COUNCIL: Remote Sensing with special reference to agriculture and forestry, Washington National Academy of Sciences, 1970

(12) KODAK: Wratten Filters, 4th Edition, Kodak, London, 1969

(13) HOFFER, R.M. and JOHANNSEN, C.J: R.S. in Ecology, Ed. Johnson, P.L., Athens, Georgia, U.P., 1969

6 ANALYSIS: THEORETICAL

To the eye, vegetation species such as grasses and bushes can be easily distinguished and, to the expert, crop types and states of maturity can be assessed.

The manner in which targets are first distinguished between and then later classified is, in humans at least, a complex physiological process (1) but analogies of human decision processes help to demonstrate the approach used in the analysis/classification.

6.1 Analysis by Discrimination

An approach to the analysis of an area of terrain might consist of examining two areas (which happen separately to consist of grasses and bushes), the object of the analysis being to determine whether the two target areas are similar or different. The terms 'similar' and 'different' would be dependent upon the targets being considered but might be related to their percentage reflectance in the infra-red (0.7 - 0.9) μm or to the heights of targets above the ground. The emphasis of this approach is the discrimination between targets on the basis of data relating to them.

6.2 Analysis by identification

A different analysis procedure could require that the two targets be positively identified rather than be discriminated from each other. In the case of a human observer the process is virtually intuitive and consists of comparing the targets with known targets previously encountered and identified. Similarly a 'machine' decision is the result of correlating measurements of the targets with those of known targets. Discrimination of the targets is not implied by this approach. In both approaches there will be a measure of uncertainty related to the eventual result.

6.3 The Parameters used for Target Analysis

Within the scope of the present study the parameters used for classification are the corresponding densities on the films - and film layers in the case of a colour film - which are in turn a function of the reflectance properties of the target over the waveband(s) being sensed.

The differences in value, chroma and hue of objects whether they be vegetation, soils or rocks are appreciated to some extent by the eye but the subtleties of the reflectance spectra are reduced by their integration over the (0.45 - 0.70) μm band by the eye and brain.

However, a considerable number of radiometric studies have shown that on the basis of their reflectance spectra, vegetation, soil and rocks types can theoretically be identified (2) - thus for example it would appear possible to differentiate between several particular genera of plants by measuring their reflectance coefficients at 550 nm which range from 8% to 20% (3).

In general, the targets either between which discrimination is sought or of which identification is required will be numerous and so no single waveband will be capable of providing a unique discriminant measure. The number of wavebands sensed by experimenters has ranged from one (filtered black and white film) to 24 (4) and in this study was eight (photographically sensed) and one (linescanned).

The information which is not directly appreciated by the human observer is that from wavebands outside the visible spectrum; in particular the 'near' infra-red (0.7 - 1.0) μm which is of particular relevance to vegetation studies and the long wave (3.0 - 14.0) μm region associated with the emissivity and surface temperature of targets and termed the 'thermal infra-red'. The

information content from these two infra-red wavebands is, in general, not related directly to the target reflectance properties in the visible spectrum and is of optimum value when used in conjunction with the latter spectrum for classification purposes.

The reflectance spectrum of a target becomes, when measured, a set of samples over discreet wavebands and is referred to as the target Spectral Signature. In the simplest case, classification consists of allocating a target to a category on the basis of the spectral signature. However, the spectral signature is not necessarily unique to a particular type of target and, although identical targets will have identical spectral signatures, the converse does not automatically follow. For example a black and white photograph will record many targets as the same grey tone i.e. identical spectral signatures, yet they need not be identical.

For a given waveband under consideration there will, in practice, be a finite range of values that the measured parameter (e.g. % reflectance) can take. The complete set of values is termed the Measurement Vector.

Hence the definition of a spectral signature can be the n values associated with the n measurement vectors which were the result of observing the target. (In this study the term Observation is used to describe the spectral signature derived from the multi-spectral camera array).

The n measurement vectors are, for convenience, considered at this stage to be orthogonal and from the concept of identical targets outlined above, identical targets will be found at the same position in the n dimensional (n-D) space, referred to as measurement (m) space, which the vectors span.

In practice a particular target will be characterised by a series of observations and for a given vector the observations will take

on a gaussian type distribution, the target being represented by a multi-variate gaussian 'cloud' rather than a point in m space. Consequently a collection of different targets when 'projected' in m-space will take on the appearance of a number of clouds which may or may not overlap depending upon their spectral signatures.

The manner and form which the analysis of the m-space takes is dependent upon the a priori knowledge available about the targets; the choice lies primarily between a supervised or unsupervised approach.

6.4 Supervised Learning Approach to m-space Analysis

The supervised approach is applicable when there exists a set of observations made on known targets. This enables the n-D m-space to be partitioned, each partition representing the region characterised by a particular target type. The partition boundaries represent the surfaces in n-D at which there is an equal probability of a point, falling on the boundary, being associated with the two partitions on either side of it. The partition boundaries themselves are derived from the probability functions functions associated with the different targets.

An unknown point is classified by means of its relative position in m-space. The classification procedure derives a probability score of its membership to each of the several partitions; the highest probability implying membership of that particular partition.

In practice the approach has been to collect imagery over areas such as agricultural land (5), (6). A 'training set', e.g. a set of fields for which ground truth is available, is used to determine the probability functions associated with each field type and the remainder of the imagery classified using Bayesian (5)

or other 'likelihood' (6), (8) criteria which operate on the probability functions.

Several drawbacks are associated with supervised learning:

(i) The training sets must be representative and/or typical of those unknown targets in the remainder of the imagery.

(ii) The number of identifiable target types can at best equal the number of training sets used (subject to the inclusion of an extra class termed 'unclassified').

(iii) The distributions on which the probability functions are based and the decision criteria derived from them assume Gaussian type data distributions. This may not be the case and the resulting partitioning may therefore be sub-optimal (7).

Indirectly (iii) above is a justification for applying a method of supervised learning for without a priori knowledge as to the form which the probability functions take, the analysis assumes a gaussian type. However, from the training sets a decision criterion based on their particular probability functions could be derived using supervised learning.

The advantages of supervised learning are its speed of application and the ability to interface a man with the machine.

The need to extract the training sets from the several megabits of other data contained in a given scene has resulted in line-printer or visual display units being developed. The latter not only allow interactive graphics but also permit an on-line assessment of any changes in decision criteria which the experimenter may make. As the decision criteria operates on each observation separately and in turn, it is possible (9) to replay the data (normally stored on magnetic tape) through an analogue classifier.

The results can then be processed and displayed in real-time where the analogue decision network is slaved to a digital computer which derives the initial probability functions from the training sets. Hybrid digital/analogue interactive machines using supervised learning techniques appear to represent the more advanced approach to image processing (10).

6.5 Unsupervised Learning Approach to m-space Analysis

The supervised learning method partitions measurement space without recourse to any a priori knowledge of the targets or of their types.

Earlier it was stated that, at least theoretically, the observations on a group of similar targets would form a multi-variate Gaussian distribution in m-space with different types of targets occurring in separate regions of the space. Hence the classification procedure could be considered as isolating the cluster of points which forms a given distribution and then correlating it with a particular target type.

Searching for the regions in measurement space in which the clusters fall is merely operating on the data without reference to training sets or the like and is referred to as cluster analysis or unsupervised learning. The technique was used exclusively in the present study and as a consequence is discussed in more detail.

6.6 Cluster Analysis

In general terms cluster analysis techniques can be applied to any type of distribution of observations in m-space (11) but earlier it was stated that clusters in the form of Gaussian clouds were most probable. This implies that certain relationships exist firstly between points belonging to the same cluster and, secondly, between different clusters. The mathematical formulation of the relationships forms the basis of the partition processes.

The one dimensional expression of the Gaussian distribution **f(x)** is of the form:

$$f(x) = Ae^{-h^2(x-\bar{x})^2} \qquad 6.1$$

where; $\bar{x}$ is the mean value of x

$A = \frac{h}{\sqrt{\pi}}$ for a normalised distribution

$h = \frac{1}{\sigma\sqrt{2}}$ where σ is the root mean square deviation of x

The probability, P, that an observation will fall between $\pm t\sigma$ units of the mean, $\bar{x}$ is given by:

$$P = \int_{x=\bar{x}-t\sigma}^{x=\bar{x}+t\sigma} \frac{1}{\sigma\sqrt{\pi}} \cdot e^{-(x-\bar{x})^2/2\sigma^2} \cdot dx \qquad 6.2$$

This is reduced by the substitution:

$$T = \frac{(\bar{x}-x)}{\sigma}$$

Thence 6.2 becomes:

$$P = \int_{-t}^{+t} \frac{e^{-\frac{T^2}{2}}}{\sqrt{2\pi}} \cdot dT \qquad 6.3$$

Tables exist for the value of P over a range of t and hence the probability of a particular observation being associated with a given distribution can be obtained.

Most clustering routines do not utilise directly the relationships of equations 6.1 and 6.3 but draw on the concept implied by them of the form which the clusters take in m-space.

Fundamentally different methods, termed Agglomerative and Divisive, can be used within cluster analysis routines.

6.7.1 Agglomerative (fusion) Cluster Analysis

Each observation is treated as an individual and clusters are built up by associating different observations with each other, i.e. initially there are as many partitions of m-space as there are observations and at each step the number of partitions is reduced by one as most similar observations or groups of observations are associated together within a common partition cell.

The need to find most similar observations implies an $N(N-1)/2$ sized similarity matrix whilst the number of steps required to reduce the initial N partitions to M is $(N-M)$.

6.7.2 Divisive Cluster Analysis

Divisive routines consider m-space as a single partition and then subdivide it into the two most dissimilar partitions. These partitions can be further subdivided, the process continuing until finally each partition has only one observation associated with it. The advantages of such rountines over agglomerative approaches are that the number of steps required to obtain M partitions is $(M-1)$ and there is no need for a large matrix to store similarity/dissimilarity measures.

6.8 Hierarchical and Iterative Relocation Considerations

The agglomerative and divisive routines discussed earlier have been treated in a hierarchical manner in that each merging or division of partitions was considered as an irrevocable step. However, although each step in itself is designed to optimise the local requirements of similarity or dissimilarity, in terms of the situation throughout the whole of m-space the step could well be sub-optional.

For example the situation in Figure 6.1 would result after a division of the first partition in B being subdivided into B' and B". Consequently cluster B would never be a single entity as further divisions could result in, for example, the partitioning of (A+B') and (C+B"). Similarly an agglomerative routine applied to the two overlapping distributions A and B shown in Figure 6.2 would result in clusters forming in areas 1, 2 and 3 (denoted by dotted lines) where the cluster centres and overlap are the three most dense regions in m-space. When only three partitions remain, the cluster cores would be in the centres of regions 1, 2 and 3 whilst the next step would be to combine say 2 and 3 whereas the near optimum solution would be for 2 to be subdivided and its members shared between 1 and 3.

A method of optimising the partitions after division or agglomeration (fusion) is to employ an iterative relocation routine. After each step, either one of fusion or division, all the partitions are examined by considering each observation in turn and reassociating it with another partition should the appropriate similarity or dissimilarity measure be improved. Each observation having been examined and possibly reassociated, the entire set of observations is re-examined and further reallocations made is necessary. The process is repeated until a stable situation is reached and then fusion or division, followed by the relocation routine, takes place.

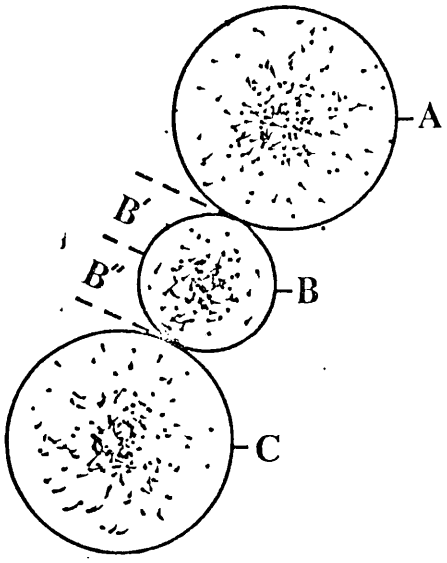

Fig. 6.1

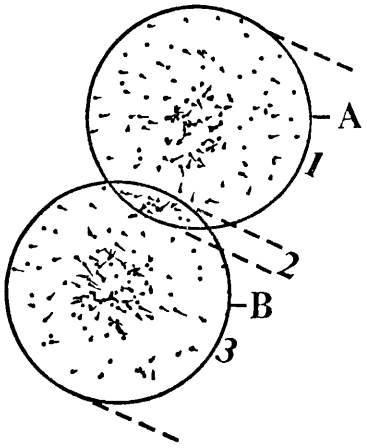

Fig. 6.2

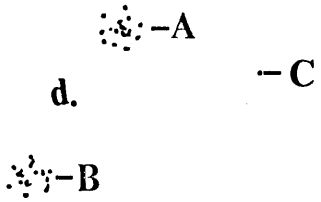

Fig. 6.3

Fig. 6.4

In addition to the optimisation of a given number of partitions, two other benefits arise when a relocation routine is used in conjunction with a fusion routine. Whereas for hierarchical fusion the initial number of partitions equalled the number of observations, relocation and fusion permit a partitioning of the observations either randomly or on the basis of a priori knowledge to be input, the number of partitions being considerably less than the number of observations. The partitions are then first optimised before hierarchical fusion commences but as the number of initial partitions is small both the store required for the similarity measures and the number of steps required to reach the desired partitioning are smaller. In fact it can be argued that if the distribution of data in m-space is in the form of unique 'real' clusters then whatever the initial partitioning, identical partitioning should occur when the number of partitions equals the number of 'real' clusters.

Although in practice, despite the fact the relocation routines attempt to optimise the partitioning, it is possible that several different stable optimum partitions of m-space can exist and thus the initial allocation of observations to partition cells could affect the final result.

Hierarchical fusion can be considered to be the particular form of iterative relocation where no reallocation occurs and, as a consequence, by examining the differences between the results of fusion routines with and without relocation a measure of the suitability of straight fusion can be obtained.

The manner in which the relocation routines would act on particular distributions can be shown with the aid of Figures 6.1 and 6.2.

(i) Division. Assuming that the first division of the three distributions in Figure 6.1 resulted in (A+B') and (C+B") very little relocation would occur. However after the next

division, of say (C+B") into C and B" relocation would recombine the partitions such that (A+B') and C and B" would become A, C and (B'+B") i.e. the three desired 'real' clusters.

(ii) Fusion. When fusion reaches the three partition levels, number 1, 2 and 3 in Figure 6.2, the next step would be the merger of 2 and 3 giving partitions 1 and (2+3). Relocation would now reallocate the observations previously contained within partition 2 between clusters 1 and 3 although obviously it would not be possible to reconstruct the original clusters A and B because of the overlap of distributions.

6.9 Similarity Measures

Before observations or sets of observations can become associated with each other within the same partition cell, some measure of similarity has to be derived between them. In general the similarity measure is a function of the various measurement vectors and so far in this study has been related to the distribution of the observation within m-space. If the distribution of the observations is assumed to be Gaussian the measures are related to the probability density functions discussed earlier (6.6).

6.9.1 Euclidean Distance Between Observations (Spq)

Where P and Q are the two sets of observations associated with two different partition cells; N_p and N_q being the number of observations within P and Q respectively: $N_P \geqslant 1$; $N_Q \geqslant 1$

The similarity measure, S_{PQ} is the euclidean distance in measurement space between the observations (for $N_P = N_Q = 1$) or between the means of the observations (if N_P and/or $N_Q > 1$). In many cases the square of the euclidean distance is used as the measure.

Thus:

$$S_{PQ}^2 = \frac{1}{N_{MV}} \cdot \sum_{j=1,N_{MV}} (u_{Pj} - u_{Qj})^2$$

where:

N_{MV} is the number of measurement vectors involved:
U_{ab} is the value of the b^{th} measurement vector for the a^{th} observation for $N_a = 1$ or the mean of the set of observations of U_{ab} over all N_a for $N_a > 1$

The square of the euclidean distance is a ($\frac{1}{+2}$) type term whereas the gaussian relationship between the mean and a particular point is of an exponential form. Such a discrepancy could be readily rectified but this does not appear to have been by other workers. Although highly suited to the linking of pairs of observations, i.e. $N_p = N_q = 1$ the measure as it stands does not encourage the growth of clusters with tightly packed centres as the mean of many observations has the same weight as that of a single observation. Thus if in Figure 6.3 clusters A and B have their means at A and B respectively and AB < AC < BC, where C is a single point, then the euclidean distance measure would merge A and B, the resulting mean partition centre being at d, some point between A and B. However, if (A and C) or (B and C) were to be merged together within a single partition, the mean positions of the new partitions would be very close to A or B respectively and the compactness of the partitions preserved.

6.9.2 Error Sum of Squares Similarity Measure

The concept to be outlined was first developed by Ward (12) and it endeavours to encourage the formation of clusters with tightly packed centres.

Initially, in fusion routines, the similarity measures are between pairs of observations and the euclidean squared distance is used. However, as soon as two observations are enclosed within a single partition cell, the cell has associated with it a measure of the similarity of the observations contained within it, and furthermore

all measures between it and other cells are derived not only from the euclidean squared distance but also from the intra-cell similarity measures (the in-group variances).

Thus for a cell C' formed by the merging together of cells C and D, the measure between C' and a cell M ($S_{MC'}$) is given by:

$$S_{MC'} = \{S_{MC}(N_M+N_C) + S_{MD}(N_M+N_D) + S_{CD}(N_C+N_D) - S_{MM}.N_M - S_{CC}.N_C - S_{DD}.N_D\} / (N_M+N_C+N_D) \qquad 6.4$$

where in general S_{AB} is the measure between cells A and B and N_A is the number of observations associated with cell A.

The similarity measure is then derived by:

$$E_{AC'} = S_{AC'} - S_{AA} - S_{CC'} \qquad 6.5$$

where $E_{AC'}$ is the similarity measure between partitions A and C'.

The effect on the similarity measure when derived by means of equations 6.4 and 6.5 is to weight it in favour of clusters with larger numbers of observations and to take account of their variances. Thus for two clusters A and B for which previously $E_{AC} = E_{BC}$ where C was a single observation, equation 6.5 would encourage C to be merged with the more diffuse cluster i.e. the cluster for which S_{-C} was greater.

The term $E_{AC'}$ as defined by equation 6.5 is often referred to as the "error term" because, unless zero, it implies that associating A with C' is to consider as identical two dissimilar partitions.

If the situation shown in Figure 6.4 were to arise and a fusion routine were being used, then the process would eventually result in two partitions A and B. It is clear that the error term for associating A with B will be much greater than that previously encountered when partitions within A and B were being merged. Consequently, if the data is distributed in m-space as discreet clusters of observations, the error term should indicate when the discreet partitions of clusters, rather than the partitions of 'real' cluster members, are being merged by the term rapidly increasing. Such an indication is of the utmost value as otherwise the clustering routine will proceed until all observations become enclosed by the one same partition.

6.10 Dissimilarity Measures

The measure discussed is of the type used in Polydiv, a divisive routine which has been developed by Lance (13).

The first division will attempt to partition the m-space distribution into two discreet distributions. If there were two multi-variate gaussion distributions which did not overlap to too great an extent, then a histogram plot of any particular measurement vector density distribution should exhibit a dimodal distribution as seen in Figure 6.5. The divisive routines merely search through the density distributions for bimodal type variations and then split the population so as to maximise the differences between the two new partitioned populations. Rather than treat each measurement vector separately, Polydiv first reduces the data by a principal components routine, standardises each new vector and then commences division. Iterative relocation routines are available but Lance has found that relocation need only be applied after several (e.g. 5) divisions have taken place where the end result may be 10 partitions.

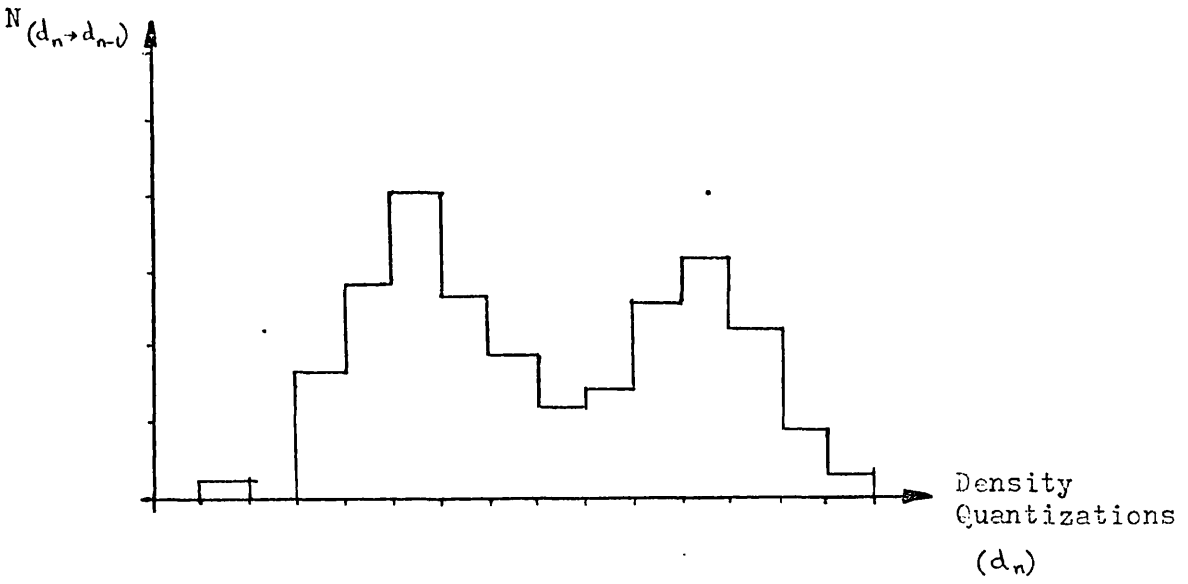

FIGURE 6.5 SHOWING TYPICAL DENSITY DISTRIBUTION OF A MEASUREMENT VECTOR

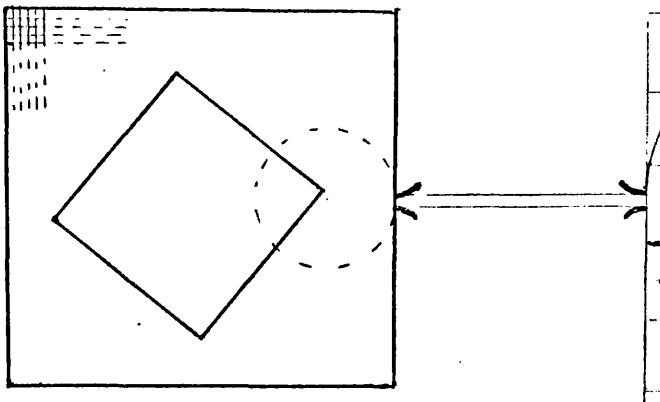

FIGURE 6.6 A BLACK TARGET ON A WHITE BACKGROUND

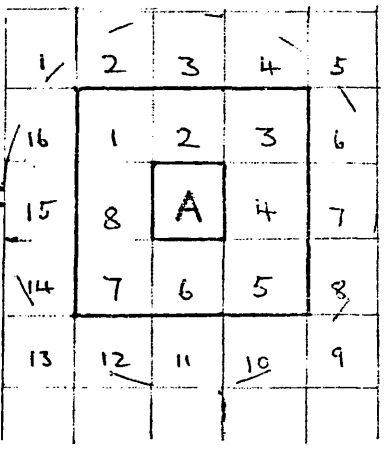

FIGURE 6.7 A SECTION OF FIGURE 6.6 SHOWING PART OF THE SCANNED ARRAY

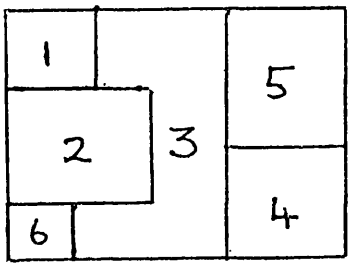

FIGURE 6.8 SHOWING THE SPATIAL CLUSTERING OF AN AREA INTO SIX GROUPS

6.11 Image Space Clustering

The previous discussions on analysis have considered the partitioning to be carried out on the observations when projected in measurement space whereas the results are general required to indicate the physical partitioning of an image (e.g. drawing boundaries around similar areas of ground). Image space clustering partitions the image, but the similarity (or dissimilarity) measures used are still the density measurement vectors. The concept is demonstrated in conjunction with Figure 6.6. which consists of a square black target on a white background. The total image is considered to have been scanned and for simplicity only one measurement is being considered.

It appears to be feasible to apply either fusion or divisive routines in order to partition the image but apart from the work presented in this chapter, Chapter 7, Appendix B, and a theoretical study by Haralick and Kelly (14), no other publications appear to consider the application of clustering to image space. Consequently the fusion routine which was used is discussed here.

The similarity measure is based on the measurement vector and is derived as before. However, the measures are only created between the partition under consideration and physically neighbouring partitions of the image and hence initially each observation constitutes a partition and observations are 'located' at the point on the image where they were recorded. Whether the neighbouring points between which the measures will be created are the eight adjacent partitions or those eight together with the 16 partitions immediately surrounding them, see Figure 6.7, or even any other partitions will depend on such factors as the noise within the scene and the dimensions of likely boundaries between uniform areas. Hence, as partition cells merge, larger and larger areas of the image are classified as similar until, as before, all observations fall within the one same partition. However, the image space

clustering cannot be pursued too far as shown in Figure 6.8 where six fields have been classified by the image space routine. The next merging of partitions must be one of the following:

1-2; 2-6; 1-3; 2-3;
6-3; 3-5; 4-5; 3-4

despite the fact that, say, 1 and 4 may be identical in all ways. Consequently, when a certain number of partitions determined through considerations related to the final number of desired partitions has been reached, the measurement space clustering routine is applied. This will then associate the partitions according to their similarity in measurement space and will lead to 1 and 4 being classified as similar. The results from such an image space clustering have proved sufficiently promising for further studies to be made.

A programme recently developed has shown that when image space clustering is applied to a string of observations (c.f. a single row of the array in Figure 6.6 and thus only observations on either side of a particular observation are used for similarity measures) instead of searching the whole set of similarity measures and acting upon the smallest, it is possible to permit the merging of one fifth of all the partitions at once as shown schematically in Figure 6.9. Having reduced the number of partitions along the rows of the array (Figure 6.6) the routine is then applied to merge partitions between rows using steps 2 to 5 as before. This processing should reduce the observations to a number of partitions which can be economically handled by the measurement space routine.

The possibility of applying the dissimilarity measure as used within Polydiv has been considered (13) as an alternative approach to overcome the problems of storing similarity measures. If the observations are examined sequentially, i.e. either as they are derived from the multi-spectral scanner detectors or the photographic raster scanned matter, then as the observations pass from

one desired partition to the other (e.g. the observations relate to one field and then another, both being desired as separate partitions in the final analysis) then the observations should show a marked change. Hence, if some dissimilarity measure could be derived from the sequential observations it may be possible to set a dissimilarity threshold which would indicate when different 'desired' partitions were being sensed. Figure 6.10 illustrates schematically how a proposed routine would function.

Figure 6.9

A proposed agglomerative image/measurement space clustering routine

Step 1: Write observations on to magnetic tape.

Step 2: Rewind tape. Read tape. Create similarity measures and store the smallest 20%.

Step 3: Rewind tape.

Step 4: Update the new partitions derived from step 2 and write on to a new tape.

Step 5: If more image-space clustering is required, go to step 2.

Step 6: Apply measurement space clustering.

Step 7: Output results.

Figure 6.10

A proposed divisive image/measurement space clustering routine.

Step 1: Accept observation.

Step 2: Add to previous observations.

Step 3: If the distribution is not bimodal return to Step 1.

Step 4: Remove those observations formed by the earlier observations and store them.

Step 5: Return to step 1 unless there are no more observations.

Step 6: Apply clustering techniques (in image and/or measurement space) to obtain the required number of partitions.

Step 7: Output results.

6.12 The Differences Resulting from Measurement and Image Space Clustering

Superficially the discussions of image and measurement space routines have not suggested any particular reasons as to why the final results might differ from one another. However a consideration of the probability functions and the image space similarity measures demonstrates how the routines construct different partitions of the image. Within a typical image, the chances of two observations being very similar is high, but the chances of them being from adjacent points on the image is considerably lower. Consequently these highly similar observations will become enclosed by an m-space routine within a single partition. Other observations will also become associated with the partition, and the mean centre position of the partition in measurement space will be in a particular region. However, if the most similar adjacent partitions were merged, the observations would not be as similar as before and the mean centre of the measurement space projection of the resulting partition need not be near its counterpart. Once a number of observations have become associated with a given partition, the Error Sum of Squares routine tends to fix its position in m-space because of the weighting factors discussed earlier. The final partitioning of the observations is consequently quite different for image and measurement space procedures. (See Chapter 7, also Appendix B.)

6.13 Data Pre-Processing

Pre-processing involves the manipulation of the data prior to the analysis and can be of a corrective and/or transform nature.

Corrections are applied when known effects such as lens distortion, non-linear detector response etc., are involved. However, some factors such as variable haze concentrations, cloud shadow and terrain slope will affect the data in a manner which although it can be determined theoretically would, in practice, be too time consuming. In these cases it is simpler to transform the data so as to remove the effects.

Along a particular flight line several conditions can vary. Figure 6.11 shows some of the fluctuations which affect photographic imagery. The target T1 is considered to be on a flat horizontal plane and changes in its position can not only alter the angle ϕ but also the angle β which is the angle between the (Sensor - T1 - Sun) and (Sensor-Nadir-Sun) planes. Families of curves can be projected on to the terrain representing lines with constant values of β or ϕ, but to sample along these lines (so as to remove the appropriate angle effects) is only practicable when scanning systems are placed in satellites whose orbits and orientations permit the scanners to follow the particular curves. Changes in ϕ and β modify the apparent reflectance of the target as a result of the specular and diffuse reflectance properties of the targets. Target T2, which may be identical to T1 will appear to have different reflectance properties not only because the values of ϕ and β are different, but also as a result of its not being on a horizontal plane and also because the path lengths (and hence atmospheric absorption) between (Sensor - T1) and (Sensor - T2) are different.

Atmospheric effects could be compensated for either by the use of models (15) or by estimating their attenuations by means of sensor responses over known targets (16). Turner (15) suggests that models are more applicable to very high altitude imagery where the effects of changes in haze concentrations etc. contribute proportionally less to the total attenuation whereas at lower altitudes transforms appear more promising (17), (18).

FIGURE 6.11 SHOWING THE GEOMETRY RELATING TO TERRAIN REFLECTANCE MEASUREMENTS.

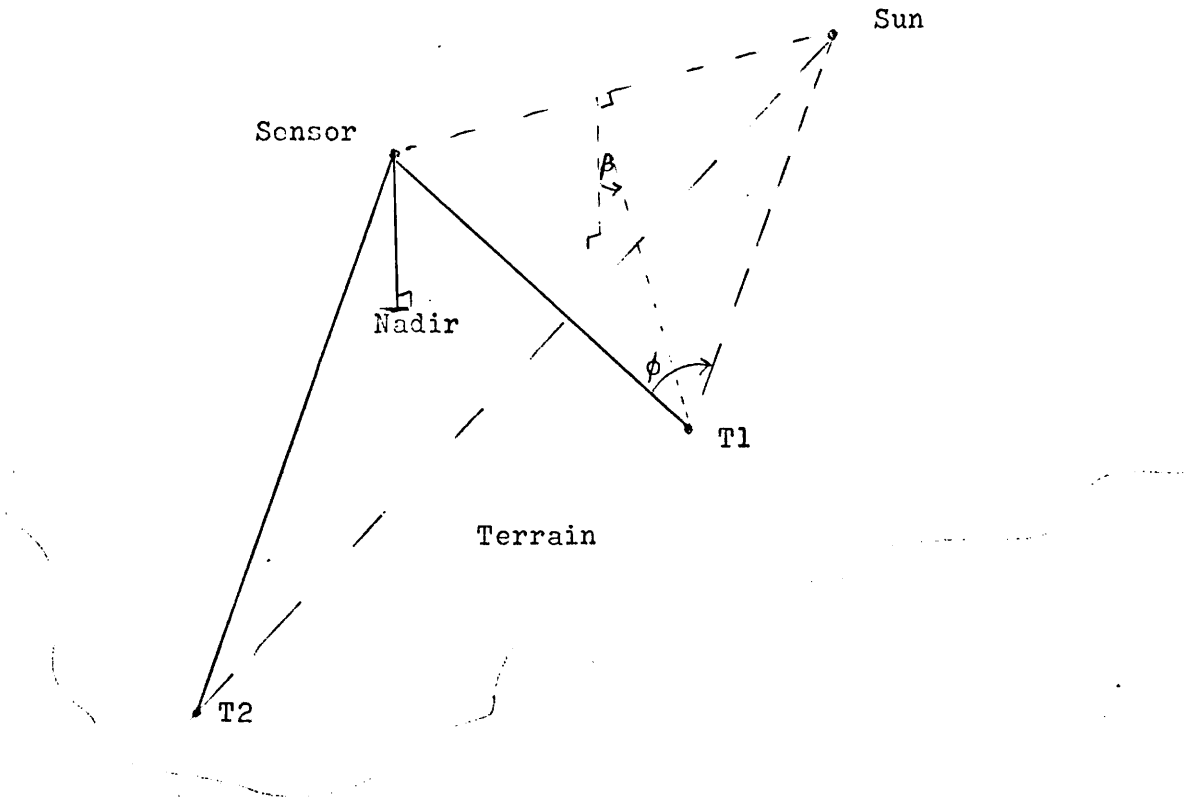

Several transforms are available which reduce the effects of the atmosphere and changes in ϕ and β (17). Of more interest to the present study are those termed single waveband ratioing and sigma waveband ratioing - the other transforms are of more direct application when wide fields of view ($> \pm 30^{\circ}$ from the nadir) are used (18).

6.14 Single Waveband Ratio Transform

For a particular set of neighbouring wavebands, the effect of T1 and T2 having different values of ϕ and β will be to alter the magnitude of the reflectance reading in the wavebands by a constant factor rather than distort the spectral signature - unless, that is, the values of ϕ and β are such that the whole scene is different and/or the reflectance is a body colour effect (see 5.4) where spectral signature changes could be expected.

Let the signal S at the surface of the two targets and in wavebands a and b be;

$$S_{aT1};\quad S_{bT1};\quad S_{aT2};\quad S_{bT2}$$

Then the effects of T1 and T2 being at a spatially different position on the detected signal can be factors C_{T1} and C_{T2} respectively which transforms the surface signals into the form:

$$C_{T1}S_{aT1};\quad C_{T1}S_{bT1};\quad C_{T2}S_{aT2};\quad C_{T2}S_{bT2}$$

Analysis would involve the comparisons of:

$$(C_{T1}S_{aT1} \text{ and } C_{T2}S_{aT2})$$

and

$$(C_{T1}S_{bT1} \text{ and } C_{T2}S_{bT2})$$

where C_{T1} and C_{T2} are virtually unknown and for a particular image could take on several hundred different values depending upon the magnitudes of ϕ and β .

However, if the ratio of the signals in wavebands a and b from the two targets are used, the 'C' terms drop out and comparison involve:

$$\frac{S_{aT1}}{S_{bT2}} \quad \text{and} \quad \frac{S_{aT2}}{S_{bT2}}$$

and for identical targets the two ratios are equal.

The 'C' factor can also be considered as a measure of the fraction of surface signal which is received at the detector and, if neighbouring wavebands are ratioed, then the changes in atmospheric transmission as a result of different signal path lengths are reduced.

6.15 Sigma Waveband Ratio Transform

This transform is less sophisticated than the single waveband ratio but in particular cases is adequate. It is of direct application where the reflectance of similar targets differs as a result of sloping terrain or changes in incident illumination. These changes are considered to be constant throughout the wavebands being sensed and by expressing each waveband measure as a fraction of the summed waveband measures similar targets will have identical transformed signatures.

6.16 Principal Components Transform

The correlation between two measurement vectors relating to the same scene is generally very high (for visible wavelengths usually 0.1% significance) and consequently when several measurement

vectors are used in the analysis, a large amount of redundant information is unnecessarily included.

The principal components of the measurement vectors can be derived and in many cases three or four components will contain as much as 95% of the variance within the 6 or 8 original vectors. This transform is of particular benefit to analogue classifiers where each vector of input information required its own separate circuitry (19). The eigen values of the measurement vectors are necessarily a function of the particular data set chosen and thereby relate solely to the scene under analysis and consequently they will not in general represent the optimum set for any other scene.

6.17 Data Scaling

The approach to cluster analysis outlined earlier considered the measurement vectors to be orthogonal, i.e. they were treated as linearly independent quantities. Principal components analysis routines may be used to construct the orthogonal vectors, but there appears to be no justification for so doing apart from mathematical intuition.

Similarly both the variances and ranges of the several measurement vectors will differ and programmes such as Polydiv scale each vector to zero mean and unit variance before analysis commences. Schemetically Figures 6.13 and 6.12 show in two dimensional feature space the effect of scaling the measurement vectors; the Z vector will tend to dominate the analysis when its range is increased.

FIGURES 6.12 and 6.13 SHOWING THE EFFECTS OF DATA SCALING.

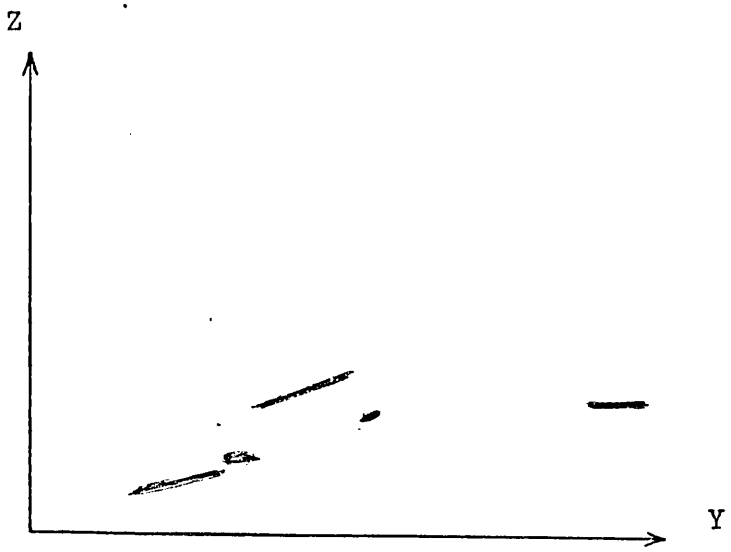

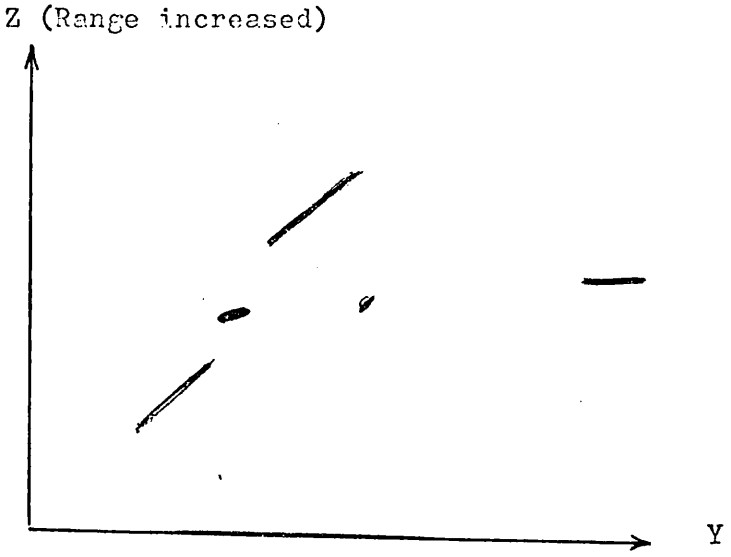

Intuitively the calibrated raw data, or the calculated target reflectance would appear to be the most sensible input.

6.18 The Application of Pre-Processing Transforms to Cluster Analysis Data

Whilst it may mathematically appear advisable to correct the data so as to obtain the ground equivalent target reflectance value, the models of atmospheric transmission/attenuation and the variability of the atmosphere make the effort prohibitive for all except satellite imagery. The choice then lies between calibrated, scaled or transformed data. The narrow field of view of the photographic systems used, combined with the very slight topographic relief in the areas imaged, have led in the main to calibrated data being used in the clustering routines of this study.

More generally the use of transforms, whilst of considerable use in removing the effects of haze, look angle etc., will reduce the uniqueness of the spectral signature by relying on relative magnitudes of the wavebands sensed rather than their absolute values for the decision criteria.

Similarly the principal components of a particular scene will generally not apply to any other scene although in the case of a supervised learning approach this may not be so important.

CHAPTER 6 - REFERENCES

(1) GRASSELLI, A: Automatic Interpretation and Classification of Images. Academic Press, N.Y., 1969

(2) N.A.S.A: Earth Resources Spectral Information System, NAS-CR-31650-24-T

(3) GAUSMAN, H.W. et al: R.S. of Environment, Mich. 7, 1599, 1971

(4) BENDIX MSDS SCANNER: IEEE Transaction, GE9, No.3, July 1971

(5) BROONER, W.G: R.S. of Environment, Mich. 7, 1929, 1971

(6) SMEDES, H.W: R.S. of Environment, Mich. 7, 2073, 1971

(7) RICHARDSON, A.J. et al: R.S. of Environment, Mich. 7, 1357, 1971

(8) PATRICK, E.A: Fundamentals of Pattern Recognition, Prentice-Hall, 1972

(9) AMERCIAL SOCIETY OF PHOTOGRAMMETRY: Operational Remote Sensing, Houston, A.S.P. 1972 (SPARC/H, p245)

(10) U.S.C. ENGINEER: University of Southern California, December 1972

(11) WISHART, D: Division Report No. R-31, Stats.1, Civil Service Whitehall

(12) WARD, J.H: Am. Stat. Assoc. J., 58, 236, 1963

(13) LANCE, G.N: Personal Communications

(14) HARALICK, R.M. and KELLY, G.L: Proc. IEEE, 57, 654, 1969

(15) TURNER, R.E. and SPENCER, M.M: R.S. of Environment, Mich. 8, 895, 1972

(16) ROSS, D.S: Photogrammetric Engineering, 39, 377, April 1973

(17) KRIEGLER: R.S. of Environment, Mich. 6, 97, 1969

(18) NALEPKA, R.F. and MORGENSTERN, J.P: R.S. of Environment, Mich. 8, 1972

(19) PRESTON: Proc. IEEE, 1220, 1973

7 THE ANALYSIS OF VISIBLE AND NEAR-INFRA-RED IMAGERY

7.1 Calibration Procedures, Corrections and Transforms

As a result of the field work (2.2), the coloured calibration boards appeared beneath the aircraft on at least one occasion whilst a set of films was being exposed. The photographs were taken with a forward overlap of approximately 60% to enable stereoscopic viewing and consequently, for each occasion on which the boards were photographed, the boards were recorded on two or possibly three consecutive frames.

Although no absolute reflectance measurements were made on the boards, their average reflectance properties were monitored with a light-meter and were considered to have been relatively constant throughout the flying period. Film-to-film and frame-to-frame changes caused by different processing, sun angles, look angles etc., were then assessed by measuring the images of the boards on different films and frames. In addition to these measurements, step-wedges were exposed on the leaders of every black and white film used. This enabled the processing and film responses to be monitored.

7.1.1 Results from the Step-Wedges Recorded on the Black and White Films

Spot density readings were made of the step-wedges on the panchromatic films used in the quantitative analysis described later on in this chapter. Figure 7.1 shows the results for the films with the green and yellow filters, suffixed 'G' and 'Y' respectively. Although the 'Y' films were processed in Australia and the 'G' films in England, the consistency and agreement was found to be high. A slight difference in gamma was evident between 32G and 33G, however, over the linear section of the graph (500 to 1,500 units) the root mean square deviation was found to be 34 units -

FIGURE 7.1 GRAPHS SHOWING THE MEASURED DENSITY RESPONSES ON THREE FILMS TO UNIFORMLY STEPPED DENSITY INPUTS

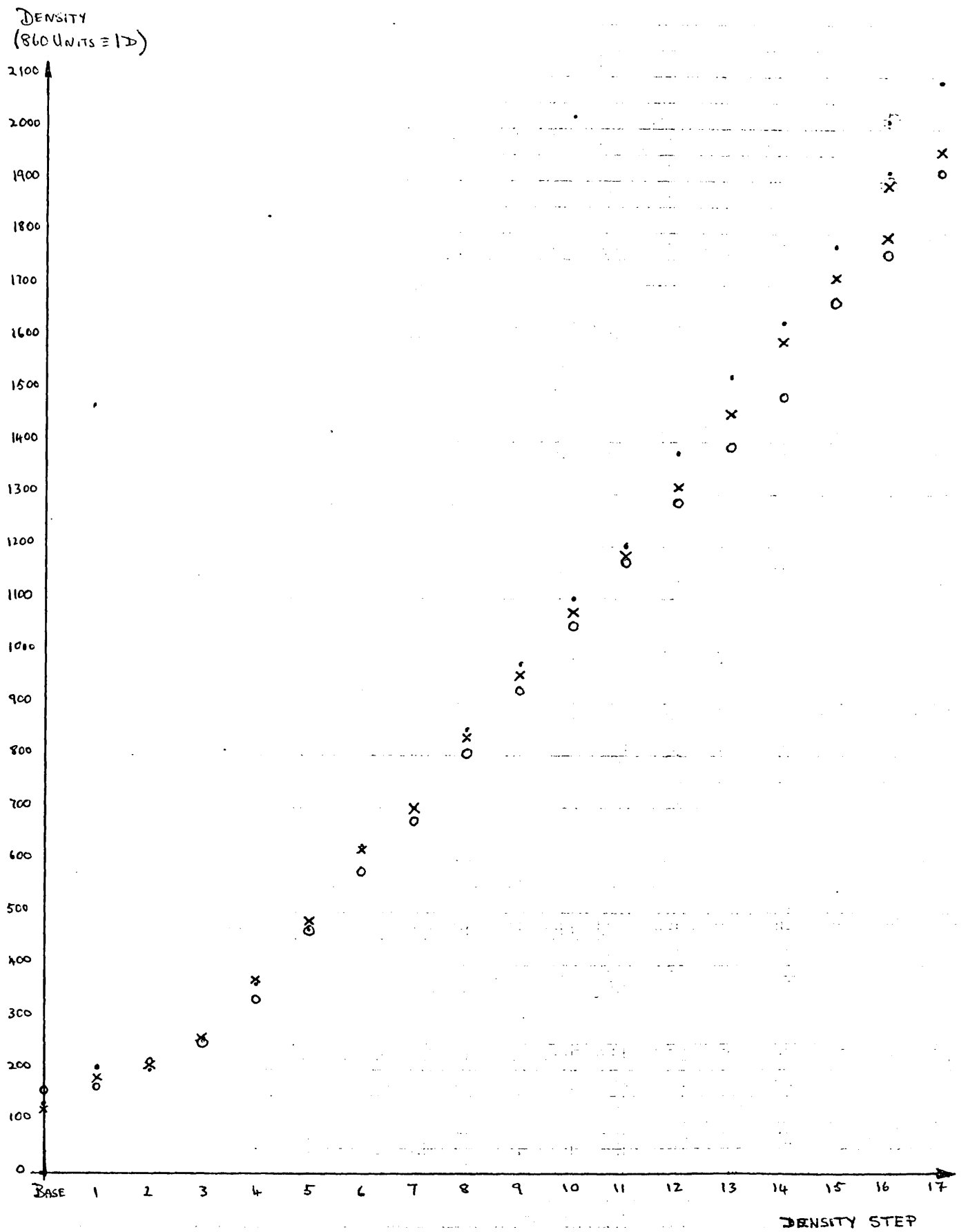

on the 'Y' films it was 33 units. The form which the quantitative assessment took (Chapter 6) involved the comparison of densities on the 'Y' and 'G' films separately and therefore the consistency sought was one within the 'Y' and 'G' films separately, rather than between them. The results from the step-wedge measurements showed the specified tolerances of development time and temperature had been met and that a satisfactory level of densitometric consistency was found to be present.

7.1.2 Calibration of the Imagery Using Ground Targets

Although the results from 7.1.1 showed high satisfactory level of processing of the black and white films, it was not technically feasible for the air survey team to record wedges on the colour films. Consequently, in order to monitor the differences between colour films, targets within the exposed images had to be used.

Initially the use of uniform areas of terrain was considered for calibration purposes. However, it was found extremely difficult to find such regions even when resolution elements equivalent to two or three metres were used. Consequently all the measurements made and discussed below relate to the calibration boards - although their surface reflectance properties differed considerably from those of the natural terrain.

The boards were sampled with a 50 x 50 μm spot; samples being made separately through each of the separation filters in the case of the colour films. Figures 7.2 to 7.9 show the several spectral bands and the densities of the fixed boards within each of the respective bands. The films to which the measurements refer are from the sets numbered '32' and '33' whilst the suffixed number (e.g. - 323) is the film frame count.

The bandwidths of the filters (1) and the spectral sensitivities of the emulsion layers within the folour films (Figure 2.1) should

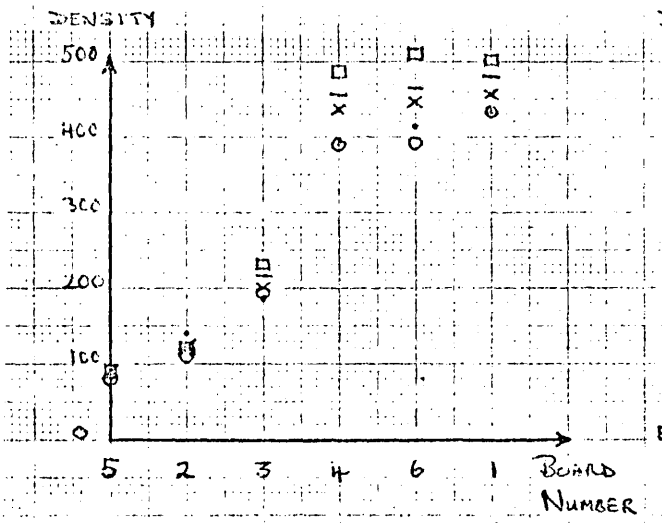

FIGURE 7.2 TRUE COLOUR (GREEN)

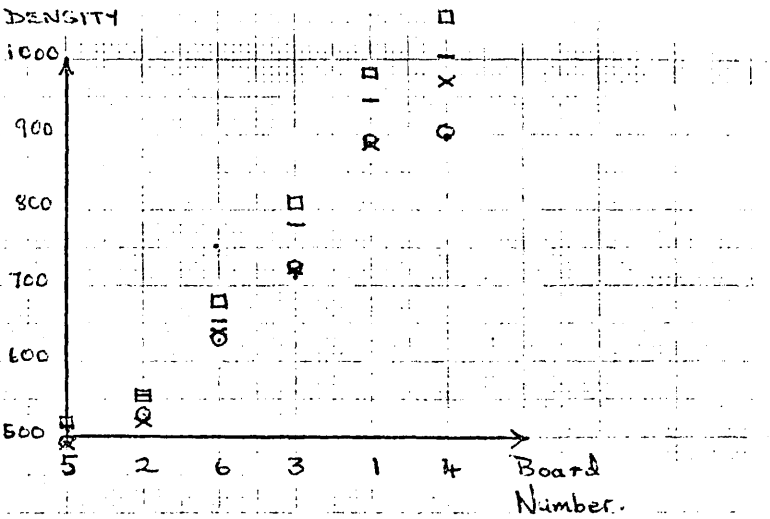

FIGURE 7.3 TRUE COLOUR (RED)

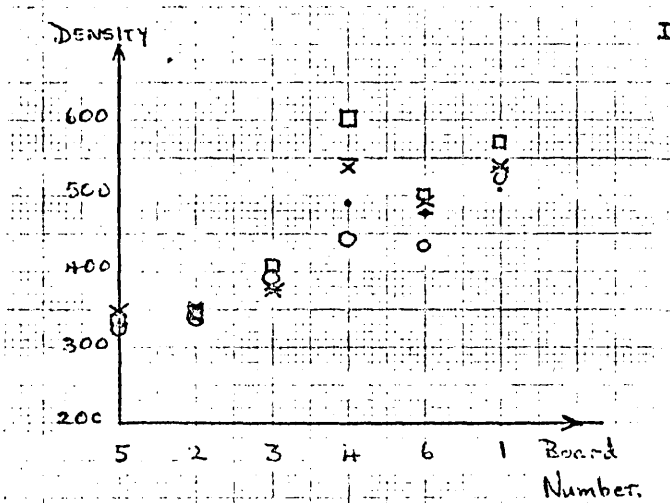

FIGURE 7.4 FALSE COLOUR (BLUE)

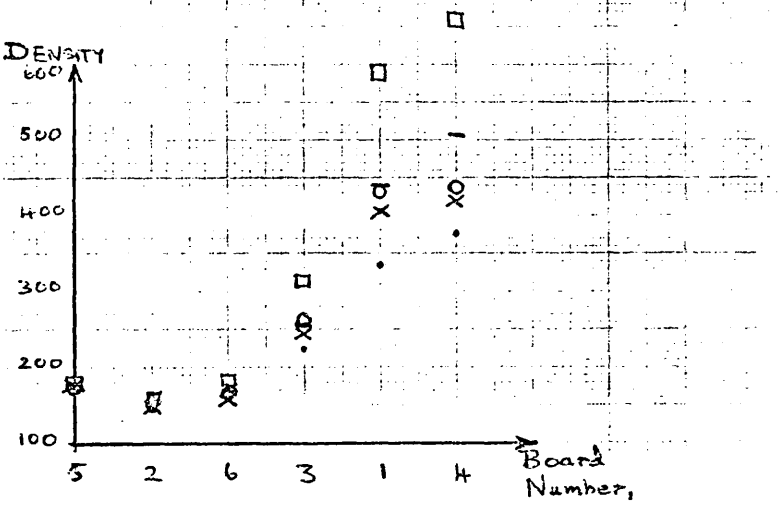

FIGURE 7.5 FALSE COLOUR (GREEN)

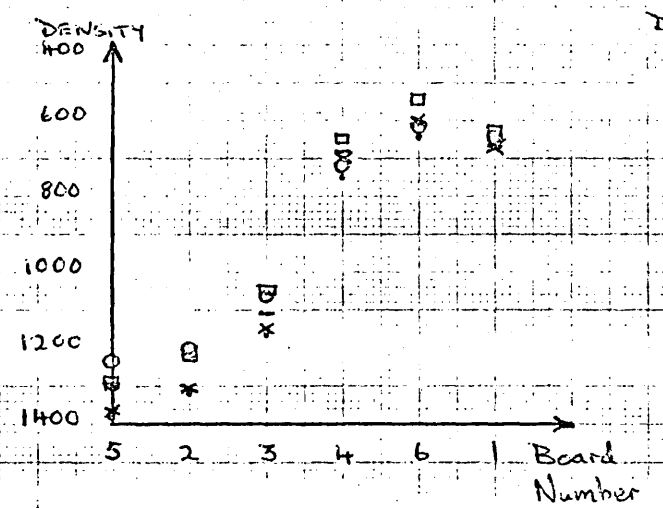

FIGURE 7.6 PANCHROMATIC (GREEN)

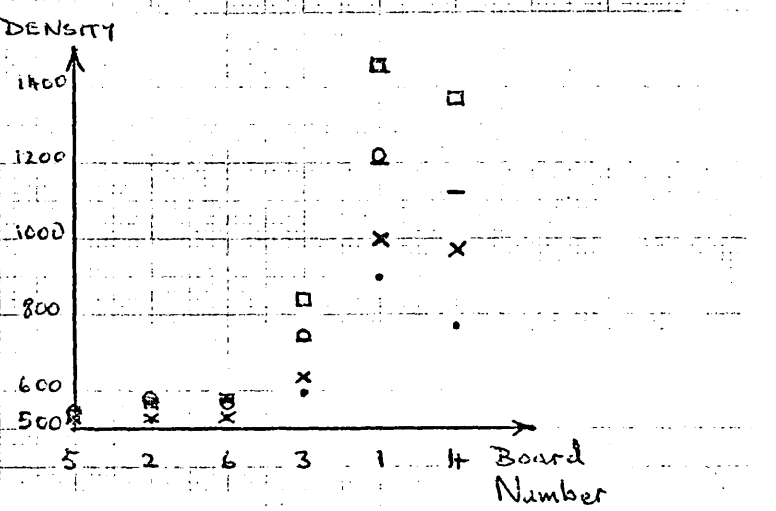

FIGURE 7.7 FALSE COLOUR (RED)

FIGURES 7.2 TO 7.7 SHOWING THE RELATIVE DENSITY OF THE CALIBRATION BOARDS ON DIFFERENT EMULSIONS.

(SEE AFTER FIG. 7.9 FOR KEY)

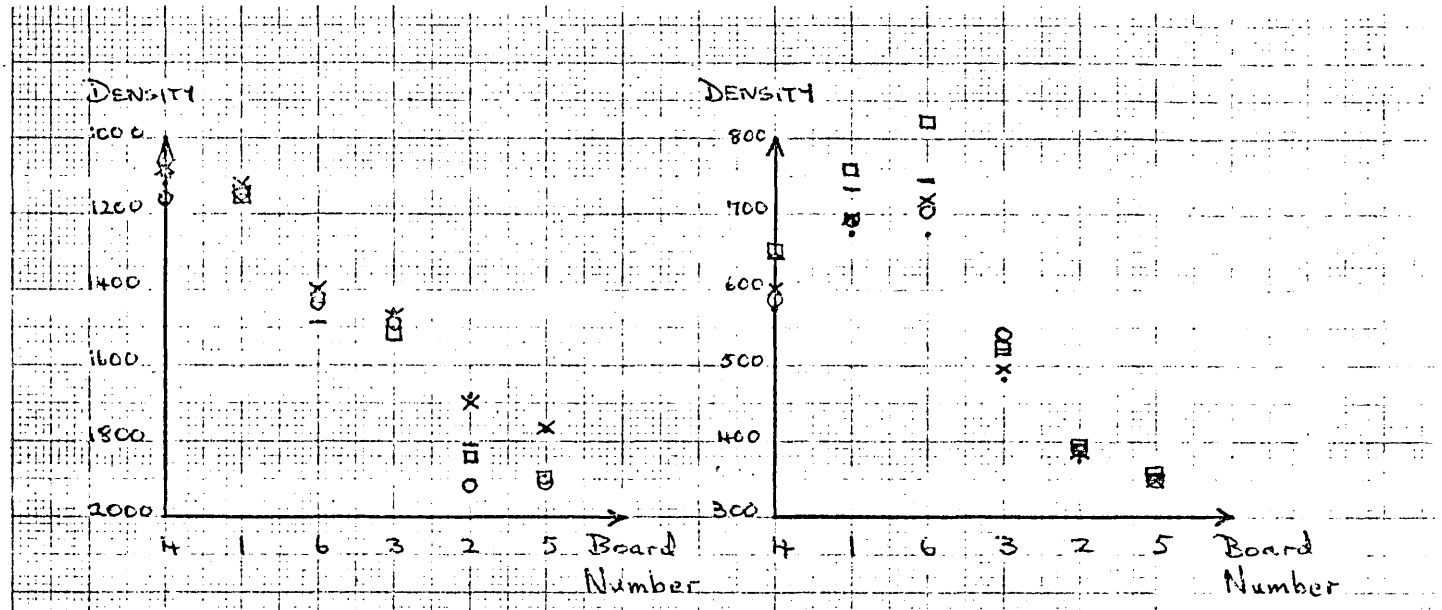

FIGURE 7.8 PANCHROMATIC (YELLOW) FIGURE 7.9 TRUE COLOUR (BLUE)

FIGURES 7.8 AND 7.9 SHOWING THE RELATIVE DENSITY OF THE CALIBRATION BOARDS ON DIFFERENT EMULSIONS.

KEY FOR FIGURES 7.2 TO 7.9 :

FILM	FRAME	SYMBOL
33	323	•
33	324	X
33	325	O
32	326	—
32	327	□

ITEM WITHIN BRACKETS INDICATES EMULSION LAYER OR FILTER USED TO SELECT WAVEBAND THAT WAS SCANNED

have resulted in similar density readings for the two following cases:

(i) False Colour Blue (dye) layer: True Colour Green layer; Panchromatic film with green filter

(ii) False Colour Green (dye) layer: True Colour red layer

In the figures appropriate to these comparisons the boards are ranked similarly along the X axis, whilst for clarity, the density scales for the negative black and white films have been inverted.

Each of the wavebands shows the same general density change from frame to frame. Thus 32-327 is always darkest with 32-326 lighter and then 32-325, 33-324 and 33-323 exhibiting a high degree of similarity. However, it can be seen that despite the general correlations between frames, there are noticeable differences when the wavebands discussed above are examined. The differences are greater than the experimental error and therefore must result from differences in wavelength sensitivity. The correlation between wavebands is discussed more fully later on in this chapter.

The error placed on a given reading was $\pm 1\%$, a figure derived when the same targets were re-sampled several times.

Frame 32-327 on the false colour film was one subjected to under-exposure as a result of a faulty camera mechanism (see 2.3). The effects are seen as an increased density reading when compared with other frames.

Table 7.1 shows the readings made on the green sensitive layer of the true colour film after corrections were applied. The corrections resulted in the readings being absolutely and linearly related to density: 000 being equivalent to no attenuation whilst 860 units were equivalent to an attenuation of 1D. Each board density was

TABLE 7.1 SHOWING THE ATTENUATION OF THE FIXED CALIBRATION BOARDS AS MEASURED ON THE GREEN SENSITIVE LAYER OF THE TRUE COLOUR FILM. (1D=860 UNITS)

Board No.	1	2	3	4	5	6
Frame/Film No.						
323/33	453	124	202	414	104	433
324/33	475	138	220	457	110	465
325/32	456	127	214	413	104	416
326/32	500	140	235	476	107	482
327/32	521	140	247	506	116	527
% Difference between frames	±7	±6	±10	±10	± 6	±12

TABLE 7.2 SHOWING THE ATTENUATIONS FROM TABLE 7.1 EXPRESSED AS A FRACTION OF ALL BOARDS ON THE FRAME

Board No.	1	2	3	4	5	6
Frame No.						
323	.26	.07	.12	.24	.06	.25
324	.26	.07	.12	.25	.06	.25
325	.26	.07	.12	.24	.06	.24
326	.26	.07	.12	.26	.06	.25
327	.25	.07	.12	.25	.06	.26
%Difference between frames	± 2	0	0	± 4	0	+ 4

sampled on the five frames where it appeared. The variations of the densities shown in Table 7.1 were considered to be of sufficient magnitude to warrant further investigation.

7.1.3 Corrections and Transforms Derived From The Calibration Boards

The differences between and merits of, corrections and transforms have been discussed earlier (6.13 to 6.18). As no absolute radiometric measurements were made, absolute calibration of the imagery by means of mathematical models (2) to correct for effects such as camera fall-off, atmospheric attenuation etc., were not considered practicable. Simple corrections, to enable film-to-film variations to be reduced were also considered, but these too were rejected when the frame-to-frame variations were seen to be of the same order as film-to-film changes (e.g. Table 7.1, board no.6).

The first transform to be applied was a scaling factor between frames. For a given frame, each board density was expressed as the fraction of the sum of the densities of all the boards on that frame. Consequently, if the differences between frames were constant scaling factors, then, by effectively normalising the densities on each frame, identical boards should have similar densities. Table 7.2 is the result of such a transformation when applied to the data used for Table 7.1. The percentage differences between the same boards are greatly reduced. This implies that on this particular emulsion layer (true colour green) the differences can be expressed as a simple scaling factor.

The same transform was applied to the densities derived from the false colour infra-red sensitive layer and from the panchromatic film (green filter). The percentage deviations about the mean density readings for each board, both before and after transformation are shown in Table 7.3. The results imply that although the frame-to-frame differences can be reduced, they may remain as high as $\pm$19% if the under-exposed band on the false colour film is included.

TABLE 7.3 SHOWING THE PERCENTAGE DEVIATION OF THE ATTENUATIONS OF THE CALIBRATION BOARDS ABOUT THE MEAN, BEFORE AND AFTER TRANSFORMING.

Board No.	1	2	3	4	5	6
Film layer						
False Colour Red.						
% Before	$\pm$36	$\pm$27	$\pm$38	$\pm$36	$\pm$32	$\pm$20
% After	$\pm$ 9	$\pm$13	$\pm$ 9	$\pm$13	$\pm$19	$\pm$15
Panchromatic (Green filter)						
% Before	$\pm$ 5	$\pm$ 9	$\pm$ 5	$\pm$ 8	$\pm$ 6	$\pm$ 8
% After	$\pm$ 4	$\pm$ 5	$\pm$ 1	$\pm$ 6	$\pm$ 2	$\pm$ 5

TABLE 7.4 SHOWING FOR EACH EMULSION LAYER THE SCALING FACTOR RELATING THE CALIBRATION BOARD DENSITEIS BETWEEN FRAMES.

Emulsion Layer	FCG	TCG	FCR	PG	PY	TCB	TCR	FCB
Frame No.								
323	.151	.186	.132	.187	.209	.175	.188	.183
324	.176	.200	.147	.192	.210	.197	.210	.200
325	.201	.186	.224	.208	.192	.189	.226	.224
326	.211	.208	.218	.202	.195	.213	.184	.186
327	.261	.221	.279	.212	.195	.226	.192	.207

Table 7.4 shows the scaling factors as derived by the above method for each emulsion layer (as opposed to each board) on each film. Thus each particular element represents the factor by which the individual board density measurements on a given frame need to be divided for frame-to-frame compatibility. Comparison of the elements indicates the applicability of summed waveband ratio transforms (6.15). For this transform to be effective the ratio of a given waveband response between two frames should be equal to the ratio from any other waveband.

For example $\frac{323,FCG}{324,FCG}$ should equal $\frac{323,FCB}{324,FCB}$ and it can be seen

that although in this particular case the comparison is acceptable

$\left(\frac{151}{176} \sim \frac{183}{200}\right)$ there is in general poor consistency.

Similarly inconsistent results were obtained when single waveband

ratio transforms (6.14) were applied to the same data, e.g.

$$\left(\frac{323,FCG}{323,FCB} \sim \frac{324,FCG}{324,FCB}\right)$$

7.1.4 The Application of corrections and Transforms to the Photographic Imagery

The differences between the step wedge densities on the panchromatic films showed that frame-to-frame and processing effects were minimal when compared with the changes seen between the same image on consecutive frames of a particular film.

Frame-to-Frame differences are the result of changing sun-target-camera angles and although for a specific set of angles (Table 7.3) a correction factor was derived, in general it was not feasible to derive a complete set to correct the whole image.

Single and summed waveband ratio transforms were applied to the data relating to the boards, with inconsistent results. This was most probably due to the differences in gammas between the emulsion layers, but further controlled exposures would be required to test this hypothesis.

The calibration boards represented the most specular surfaces encountered on the imagery - with the exception of smooth water surfaces - and, consequently, the frame-to-frame differences represented the worst cases that could be expected. Typically they were seen to be a change of between 10% to 30% in the absolute density recorded on the film.

7.2 The Analysis of Density Scans made on the Photographic Imagery

Areas of terrain for study were chosen either prior to or during the Australian field study programme. Most areas were located within Block A (Figure 4.10) and were related to the geobotanical anomalies associated with surface or near surface mineralisation. Sampling of the terrain was carried out by the geography team along a transect chosen to run across the anomaly and into the background regions on either side. The anomalies tended to be of a highly eliptical shape, often a few tens of metres across and a few hundreds of metres in length. Any particular anomaly was usually contained within one or two frames of the 1:15000 scale imagery.

The line of the transect was in some cases delineated before photography took place with spots of white paint a few tens of centimetres across. The densitometer scans made on the imagery passed through these spots. Consequently, the exact locations of the scans were known and when different emulsions were scanned, problems with registration between each emulsion were reduced.

Density scans were made over several different types of terrain, vegetation features and the calibration boards. The results presented are typical of those obtained, although the classifications derived from clustering programmes using transformed data have not been presented as the results were inconclusive.

Iterative relocation techniques were applied to the measurement space clustering routines, but, as no dramatic improvements in classification accuracies were obtained, no pictorial results are presented. It was noticed however, that for different initial clusterings, it was not until a level of between 8 and 3 groups was reached that the clustered groups were similar. It was shown earlier (6.8) that, at least in theory, similar results would be obtained when the level equalled that of the number of 'natural' clusters. Consideration of the physical significance at this level of clustering showed that they were of the correct order, but as will be shown later on, the number of relevant groups was most easily determined by reference to known terrain features.

7.3 The Computer Processing Used for the Classification of the Photographic Imagery

A slightly modified version of Ward's error sum of squares clustering routine was programmed on the computer. This routine was chosen as it appeared to be most appropriate to the expected data and would search for tight, gaussian-type clusters in measurement space. Later modifications permitted image space clustering to be performed followed by measurement space clustering when 15 groups were reached. The results from these programmes, together with the raw data were written on to magnetic tape. This enabled further processing of the clustered data to be undertaken. Routines for deriving mean densities, r.m.s. deviations, feature space plots and other functions of the data set were written. A programme was also devised and written to enable the results of the clustering to be displayed in a spatial fashion. It was termed a Group Distribution plot and was output on microfilm. The Group Distribution

plots enabled the physical significance of different levels of grouping to be assessed by displaying the classification of the observations in the format of the original scan line. Although the plots are derived by the reduction of the number of classifications by one at each step, it has been found easier to discuss the results by considering the smallest number of groups - two - and then three, four, five and so on.

Figure 7.12 shows the Group Distribution for the measurement space clustering output pertaining to the line delineated by arrows on Figure 7.11. The abscissa, numbered 1 - 128, represents the observation number corresponding to that part of the scan line shown directly above in Figure 7.11. Three of the eight density scans made along the line are shown in Figure 7.10. The G.D. plot ordinate (numbered 1, 3, ..., 25) represents the number of clusters (groups) shown at that ordinate (or level number) on the plot. Thus, for Figure 7.12, at the three group level, observations 1, 2 and 3 (seen by comparison with Figure 7.11 to correlate with a shadow) are classified as similar and are represented by symbol 4. Similarly, observations 15 to 36 belong to the group represented by the symbol 6, and so on. The symbols, which are merely labels and are relevant only to a particular figure, were restricted to 15 in number to avoid confusion.

Although the actual classification of observations was performed with clustering routines, several different forms of data processing were applied to the data prior to, and independent of, the clustering in order to investigate their usefulness in data reduction. The results from these is presented in Section 7.7.

7.4 The Application of Cluster Analysis Routines to the Photographic Imagery

The analysis procedures were initially applied to scans made over the calibration boards. This enabled the computer results to be assessed over an area for which the desired results were known,

i.e. as a result of the digitization of the scanned data over the boards, the cluster analysis routines should provide six clusters corresponding to the six boards. Whilst overall such a result was obtained, it was found that when any two boards were examined, as a result of the finite size of the scanning aperture, there was an inevitable smoothing of the density step at the boundary between the boards. Consequently there were cases when this smoothed region was misclassified. However, in terms of percentages, these errors were less 10% of the total number of observations. The analysis technique was regarded as satisfactory and was subsequently applied to areas of vegetation and soil.

7.4.1 The Analysis of an Area of Banded Vegetation: Figures 7.10 to 7.13

Figure 7.11 shows the area of the Dugald River Lode which was scanned. The scan line ran at right-angles to the banded vegetation, the latter being the result of near surface mineralisation. Symbols a-a, b-b, etc. on Figure 7.11 delineate the boundaries of particular vegetation communities and soil types. The variations within each of the three density scans shown in Figure 7.10 demonstrate the high information content present and the degree of correlation between scans.

Measurement space cluster analysis was applied to the set of observations derived from the eight density scans; the results being presented in the G.D. plot, Figure 7.12. A classification into two groups essentially discriminates between lighter areas, symbol 6, and darker areas, symbol 1. It should be noted that direct visual correlation with the black and white enlargement, Figure 7.11, is not possible as the clustering was applied to eight wavebands. Clustering into three groups corresponds to light colour ground (6), shadows and very dark tones (1), and vegetation (4). Symbol (1) is formed by the merging of (1) and (2) at level four, (1) corresponding to the shadows whilst (2) appears to relate

FIGURES 7.10 to 7.13 -PAGE 167 ;

Figure 7.10 : Three examples of the density scans made along the line delineated by arrows in figure 7.11

Figure 7.11 : The area studied, enlarged to the same scale as the accompanying figures.

Figure 7.12 : The Group Distribution plot relating to the measurement space clustering.

Figure 7.13 : The Group Distribution plot relating to the image space clustering.

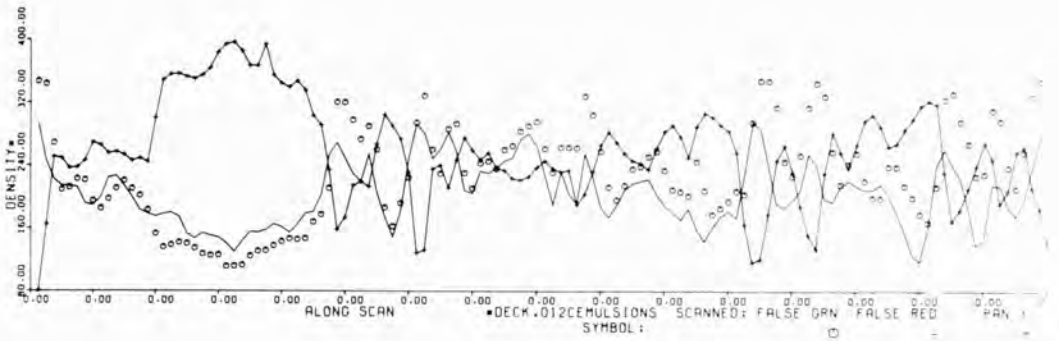

fig 7.10

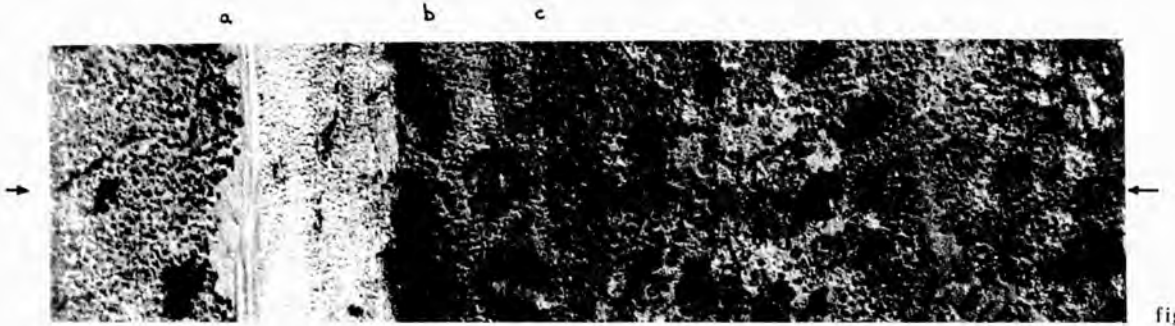

fig 7.11

fig 7.12

fig 7.13

to semi-shaded areas and very dark toned vegetation. Level five represents the stage at which the stretch of bare ground, data points 16 to 36, is differentiated from all other regions, whilst level six appears to separate the heavily shaded areas (8) from the dark toned vegetation (2).

In common with the other examples of terrain classification included within this chapter, the decision as to the appropriate and relevant number of groups requires careful consideration. One approach used was to examine the change in the error term (6.9) which should show the level at which 'natural' clusters were merged together. Whilst this was seen to be valid in the case of the calibration boards, no such effects were seen during the cases of classification of natural environments. Alternatively, the delineations of vegetation communities and soil types by the geography team was used as a template for choosing a particular level. Unfortunately this was not found to be totally satisfactory as the criterion used by the geography team to define homogeneous areas and thence to delineate boundaries included textural and other spatial features which were not used to derive the computed clustering results. The method finally chosen was to examine both the geography team's 'ground truth' data and the colour films of the area in conjunction with the G.D. plots. A level of grouping was then chosen which gave a relevant grouping in terms of observed terrain features. Thus, in the example discussed above, level five was chosen as it separated the bare surface rocks and stony clays (7) from all other areas of sandy soils; the latter being covered with triodia (4), light vegetation - probably sparse triodia and soft grasses - (6), and interspersed with shaded areas (2).

Despite the superficially acceptable correlation of the output with terrain classes, the classification lacked the large uniform areas which are normally associated with the thematic maps derived when, for example, vegetation associations are delineated. This was shown

when the area under study was classified from direct observations made on the true colour film and the results were compared with those from Figure 7.12.

A two group assessment of the colour film associated the following data points:

(i) 1 - 15 and 57 - 128
(ii) 16 - 56

Similarly a four group assessment resulted in the association of:

(i) 1 - 15 and 57 - 90
(ii) 15 - 36
(iii) 36 - 57
(iv) 90 - 128

Some structuring was seen within Figure 7.12 which could have supported such a classification but it was by no means obvious. Consequently it was decided to apply image space classification routines (6.11) in an attempt to encourage the association of spatially neighbouring points with relatively uniform characteristics rather than that of spectrally similar but spatially isolated points.

Figure 7.13 shows the G.D. plot resulting from the hybrid image/measurement space clustering of the observations derived along the line shown in Figure 7.11. As with all other examples of this hybrid clustering routine, the spatial criterion was released at level 15, and measurement space clustering routines applied. Clearly, sequences of observations have been associated within the same group, although at two and three levels of grouping there was a strong degree of correlation between this classification and that shown in Figure 7.12. Even stronger correlation was shown at level five when compared with the four groups derived by observations made on the colour film - the fifth group related to shadows which were not recorded on the four group observations. It was considered

that a classification between five and 13 groups could have been appropriate to this particular scan time. However too detailed a correlation was not attempted in view of the relatively small data sample and the lack of sufficient ground truth.

The dendrogram for the five to two level classification gave:- Symbols are shown as bracketed figures.

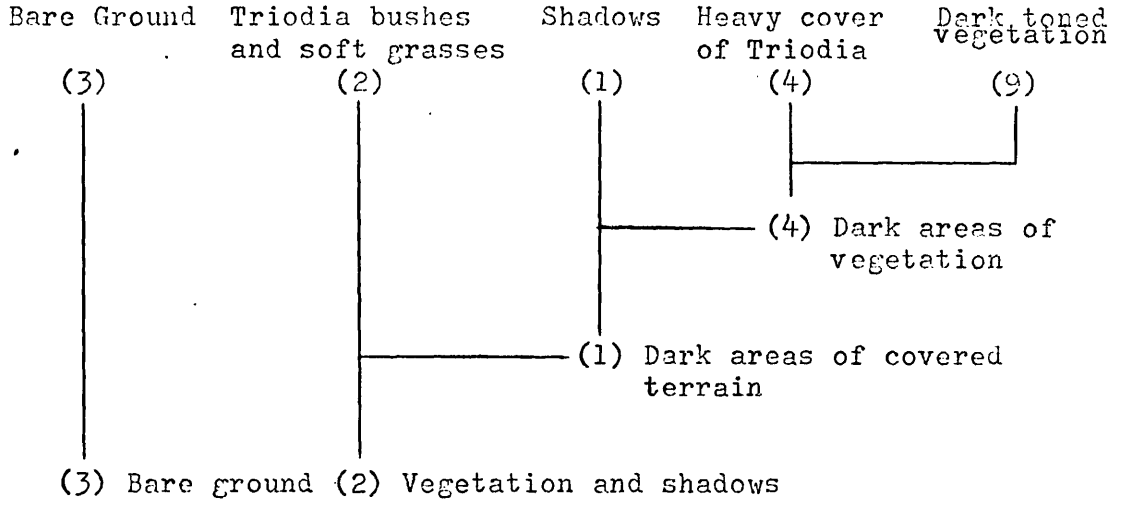

A feature of particular interest, which will be discussed more fully in Section 10 was the presence of trees. It was observed that over the image, distinct correlations were present between the vegetation community/soil type and the number of trees present. Thus along and to either side of the scan line, the area between data points 0 - 15 had few trees; 16 - 56 no trees; and 57 - 128 a significant number of trees. Such a correlation is not unexpected as it forms the basis of geobotanical relationships and arises out of the dependence of the vegetation on its host soil. Information of this type could be used as an additional feature vector. The term 'feature vector' is used rather than 'measurement vector' as the information would be derived from measurements rather than being a measurement vector itself.

7.4.2 Analysis of an Area with Developing Soil Types: Figure 7.14 to 7.17

FIGURES 7.14 to 7.17 - PAGE 172

Figure 7.14 : Three examples of the density scans made along the line delineated in figure 7.15 with arrows.

Figure 7.15 : The area examined, with the scan region indicated by arrows. The scale is the same as that for the accompanying figures.

Figure 7.16 : The Group Distribution plot relating to the measurement space clustering.

Figure 7.17 : The Group Distribution plot relating to the image space clustering.

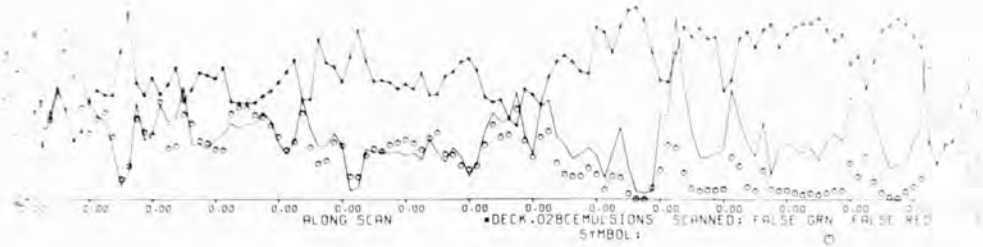

FIG. 7.14

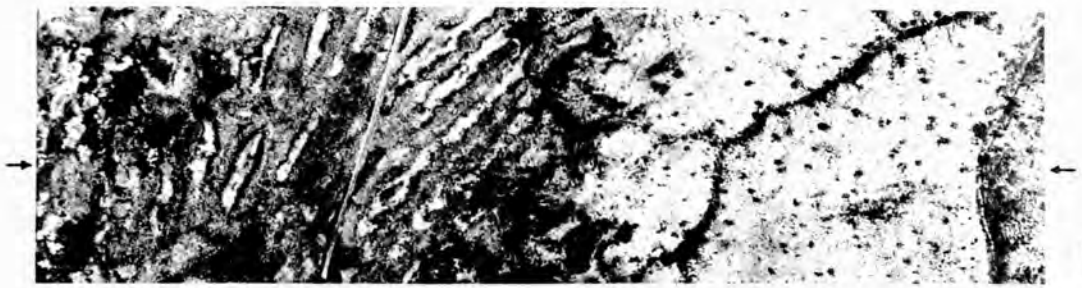

FIG. 7.15

FIG. 7.16

FIG. 7.17

The second area to be presented, see Figure 7.15, was one of flat terrain with skeletal soils and more developed soils in the form of clays. The development of the clays has resulted in an associated overlying vegetation cover seen in the left hand portion of Figure 7.15. The less developed region to the right of centre was seen to be almost devoid of vegetation, except for trees. As with the previous analysis above, there was a marked correlation between the trees and the host soils; few trees occurring to the left of data point 57, but many to the right. A track was observed running almost vertically in Figure 7.15 in the vicinity of data point 30 whilst a dry drainage channel with its associated heavy vegetation cover was seen at 60^{o} to the vertical axis from data point 70.

The G.D. plot relating to the measurement space clustering, Figure 7.16, does not correlate well with Figure 7.15, although, as was mentioned earlier, the clustering results related to the eight spectral wavebands whereas Figure 7.15 shows only the tonal variations from one waveband. At the two level grouping, symbols 1 and 5 appear to differentiate shadows and very dark toned vegetation from medium toned vegetation and bare ground. This was thought to be somewhat surprising as intuitively the classification should have separated the lighter toned region, data points 63 - 113, from the rest of the relatively darker areas. Such a separation occurs at level three where symbol 6 corresponds to the lighter area bare ground, and symbol 5 to the medium toned vegetation. Level 4 corresponds to the point at which the shadows, (1), and the dark vegetation, (2), are isolated. Further division of points classified as symbol 5 at level four appears at five with the new symbol 5 now representing the medium toned vegetation whilst (7) relates to a more sparse vegetation, probably of soft grasses, in an area where proportionately more soil is seen through the vegetation canopy. At level six, the area between data points 90 and 112 became two separate entities. However, such a division does not relate to any particular quantity or quality of the terrain, and although subsequent investigations on the ground could show the divisions to

be relevant, from the point of view of the analysis, level five was considered to be the effective upper limit. Observations made on the true colour transparency of the area showed that four areas were readily distinguishable. These are shown below in conjunction with a summary of the level five measurement space clustering classification.

Data Points	Visual Classification	Measurement Space (level five) Classification
0 - 62	Light grey-green coloured vegetation with grey-brown areas of bare soil	Mainly symbols 5 and 2
63 - 75	Soil similar to above	Mainly symbols 6 and 7
76 - 112	White chalky coloured surface with clumps of vegetation.	Predominently symbol 6
113 - 120	A drainage channel with its associated heavy vegetation.	Symbol 7

Measurement space routines were also applied when image space routines had reduced the 120 original observations to 15 clusters. Such a step was taken in order to attempt to reduce the differences between the visual and computed classifications shown above.

The results of the image space clustering technique are presented in Figure 7.17. The differences between figures 7.16 and 7.17 are considerable and the image space classifications are shown below in the form of a dendrogram. The dendrogram enables the hierarchical nature of the clustering to be presented along with the terrain classification.

Symbols are shown in brackets.

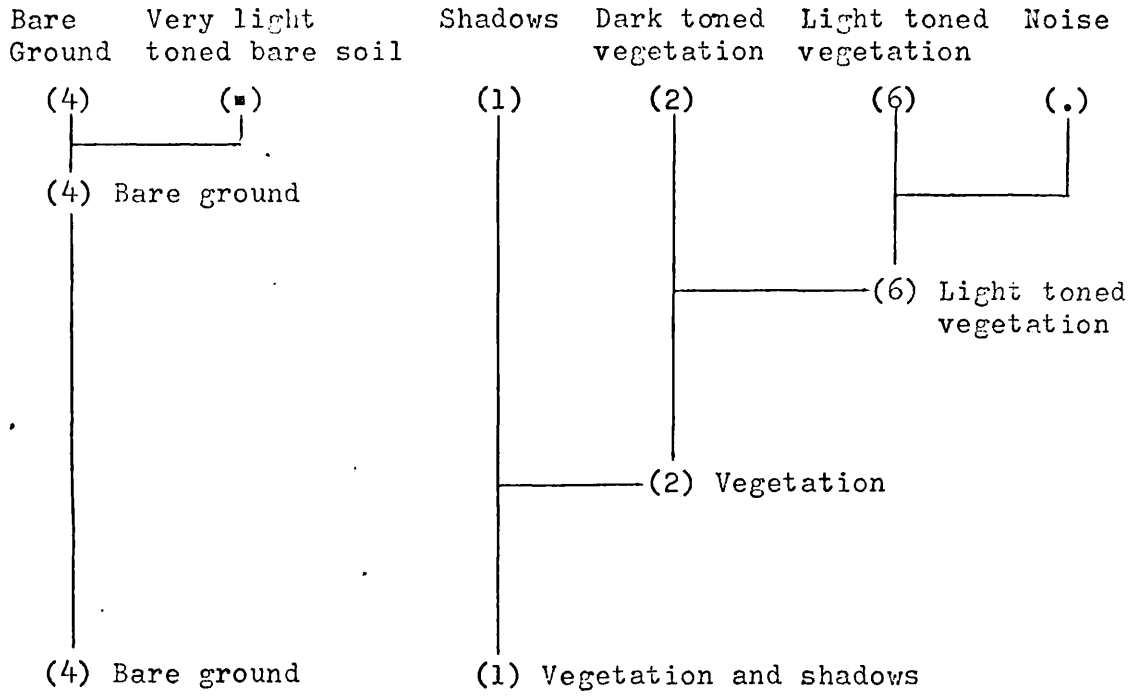

Consequently, in this case, although the number of relevant groups representing the final classification was the same for both methods of clustering, the spatial distribution of the classifications was different. The image space classification was judged to be of more value as its delineations resembled more closely those derived from thematic vegetation and soil maps.

7.4.3 Classification of an Area Affected by Mineralisation: Figures 7.18 to 7.21

In Figure 7.19 a track is shown crossing the scan line at the eighth data point whilst a dry water course is intersected by the scan at the 42nd point. In the vicinity of the 120th. data point the scan cuts across the dark vegetation associated with a small quartz reef. On both sides of the reef, low levels of mineralisation were found as a result of ground surveys.

FIGURES 7.18 to 7.21 - PAGE 177

Figure 7.18 : Three examples of the density scans made on the region delineated in figure 7.19.

Figure 7.19 : The area studied, showing the transect line, delineated witharrows.

Figure 7.20 : The measurement space clustering Group Distribution plot.

Figure 7.21 : The image space clustering Group Distribution plot.

fig 7.18

fig 7.19

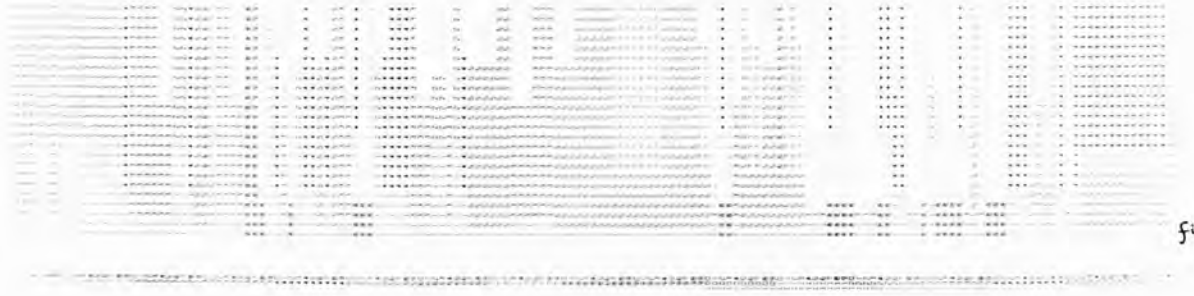

fig 7.20

fig 7.21

Direct observations of the true colour film suggested that eight regions of relative uniform nature could be expected. However, these were derived not only by observing the line of the scan but also by an inevitable awareness of the immediate surroundings. Consequently the observations were the result of both tonal and textural features and, therefore, direct correlations with the cluster analysis - which relied solely on spectral information - was not expected to yield good results. The eight groups are listed below:

Data Points	Characteristic
10 - 18	Green-brown coloured vegetation: Soft grasses.
1 - 9, 19 - 33	Patchy vegetation on clay loam.
34 - 40	Denser vegetation, similar to 10 - 18 and associated with the higher moisture content from the stream bed - data point 41.
42 - 65	Vegetation similar to 34 - 40 but on a different soil.
66 - 75, 146 - 164	Soil as for 42 - 65 but with bright green vegetation - probably triodia.
76 - 88, 99 - 105	Different soil type from above. Vegetation mid-way between 34 - 40 and 66 - 75 in colour. Possible influence of mineralisation on the vegetation.
89 - 93	A band of dark toned vegetation - triodia and grasses.
106 - 145	Dense vegetation, probably triodia, overlying soil type encountered in 42 - 64, 66 - 75.

Figure 7.19 showed that trees did not appear to grow on the very light toned areas of the terrain. This could have been due to the nearness of bedrock to the surface giving the tree roots little opportunity to take hold.

Figure 7.20, the G.D. plot resulting from the measurement space clustering routine , showed that at level two only very dark areas (shadows and dense, dark toned vegetation), denoted by symbol 8 were distinguished from all other observations. At level three the light areas of terrain with sparse vegetation, symbol 5, were resolved. Symbol 3, seen at level four and above, appeared to be associated with medium toned vegetation. At level five the correlation between either the colour film transparency or Figure 7.19 became exceedingly difficult and the level four classification, summarised below, was the highest considered appropriate.

Symbol (Figure 7.20)	Classification
1	Patchy vegetation on a clay loam soil
3	Medium toned vegetation.
8	Shadows and dense patches of triodia bushes.
5	Light areas of terrain with little vegetation.

In an attempt to improve the classification the scan line was examined - although there would not be too high a correlation with the colour film the results were considered disappointing. Upon examination it was noticed that as the result of intensive field work along the transect line, the vegetation had become appreciably disturbed. Consequently, areas of vegetation such as at 90 - 100 had been cleared to such an extent as to alter the colour film interpretation. In particular the area from points 67 to 100, consisting principally of symbol 5, was now seen to be more consistant with Figure 7.19.

Image space techniques were applied to the data: the group distribution plot, Figure 7.21, differed considerably from that derived from

measurement space clustering - Figure 7.20: Nevertheless although there were differences - e.g. data points 1 - 65 - some similar delineations were seen: Symbol 7, Figure 7.21 and Symbol 5, Figure 7.20. The results from the image space clustering supported the premise that such techniques were of more value than a measurement space approach.

7.4.3.1 The Identification of Mineralised Terrain

In the particular series of figures under discussion (7.18 - 7.21) three classifications have been compared: Colour film interpretation, Measurement Space Clustering and Image Space Clustering. The philosophy adopted has been to find that method which gives a classification most like the thematic maps which would be produced as the result of vegetation and soil mapping. The basic assumption has been that the spectral properties of the terrain, as captured by the film emulsion, were related directly to the quantities required for mapping the terrain and that the clustering procedures would extract the appropriate features from the data. However, it is quite conceivable that the spectral characteristics of an area could be changed due to effects not readily obvious either from the direct visual observations of the imagery or from ground truth work. Mineralisation typifies the difficulties encountered in attempting to correlate spectral characteristics with ground phenomena. At the lower levels of concentrations of potentially toxic minerals, the effects are seen as a less mature vegetation throughout the growth cycle and possibly a dying off of the weaker species should the environment become particularly harsh - e.g. a period of prolonged drought. The spectral characteristics of such a scene would differ from the normal. The green vegetation would appear less vivid and the near infra-red reflectance would be lower. Soils with medium levels of toxicity lead to a considerable change in the ecology of the immediate area. Species such as soft grasses no longer appear and even the hardier species appear less frequently. The vigour of trees growing in such soils is also reduced.

Toxic levels of mineralisation, as the name implies, prevent the growth of almost all local vegetation and trees. However, particular species, known as 'indicator' plants thrive under such conditions. As a consequence, the vegetation changes completely when different levels of near surface or surface mineralisation are encountered. Spectral characteristics also change as not only the relative amounts of radiation reflected from the soil and vegetation canopies vary, but also as the vegetation types alter. The effects of mineralisation are therefore not first order effects. They are detected as spectral changes induced by effects which are themselves the result of mineralisation. It is therefore unwise to assign particular effects as being due to mineralisation unless all other variants within the scene have been taken into consideration. Mineralisation, as with many other 'second*order' phenomena will probably be detected by the earth scientist when they examine the thematic maps produced from the imagery and find anomalous features such as unexpected changes of the vegetation and soil types.

The area affected by mineralisation is located on both sides of the quartz reef, $\sim$ data point 120. The minerals have been leeched out of the rocks and transported elsewhere; typically to topographically lower regions such as exist on either side of the reef. Optimistically therefore, some correlation could exist between the terrain classified as Symbol 7 (7.21) and mineralised regions. However, from the point of vegetation mapping, areas such as 28 - 66 would need to be more specifically classified.

The analysis of this particular area was considered sufficiently interesting to warrant further study although the results may prove to be of relevance solely to surface mineralisation rather than general vegetation and soil mapping.

7.4.4 The Results of the Analysis Relating to Figures 7.22 - 7.25: An Area Affected by Mineralisation

FIGURES 7.22 to 7.25 - PAGE 183

Figure 7.22 : Three of the eight density scans made along the transect line shown in figure 7.23.

Figure 7.23 : The area examined, shown at the same scale as the accompanying figures. The transect line is delineated with arrows.

Figure 7.24 : The Group Distibution plot derived from the measurement space clustering.

Figure 7.25 : The image space clustering group distribution plot.

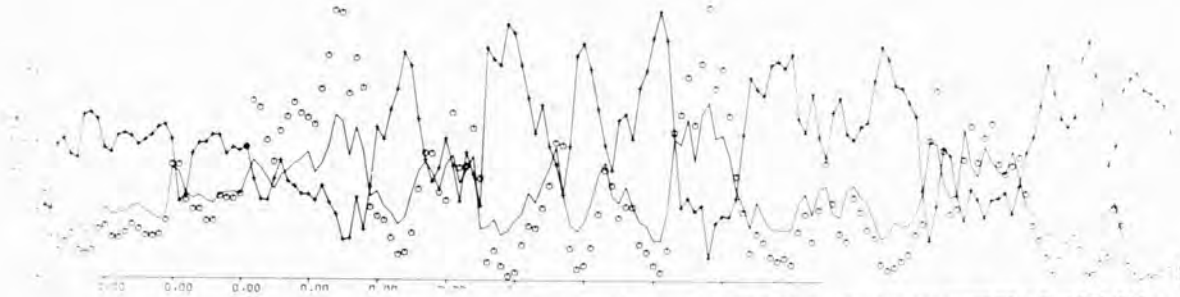

Fig 7.22

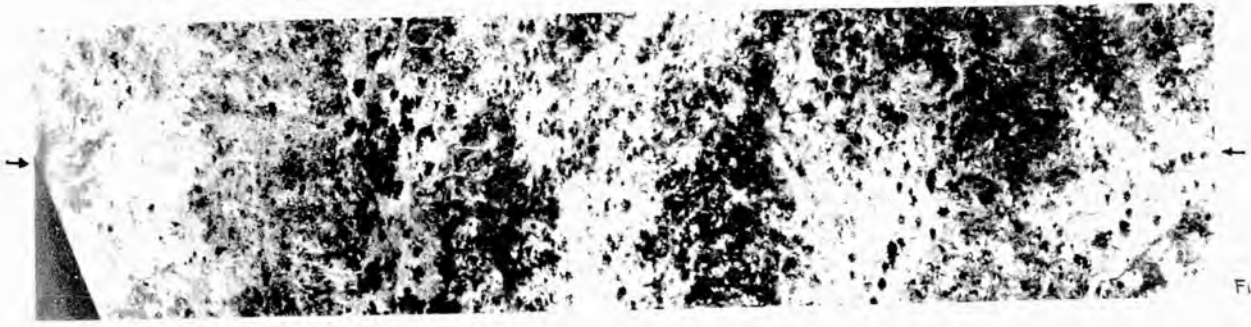

Fig 7.23

Fig 7.24

Fig 7.25

Mineralisation, in the form of copper, occurs within the area shown in Figure 7.23. The region affected is between data points seven and eighteen, the terrain appearing as a uniform grey tone, devoid of trees. The soil, which is red and sandy in appearance, overlies calc-silicate rocks and exists from data point one as far as data point 65 where a distinct change is seen. The lighter toned regions correspond to the sandy clay loams which cover the rest of the scan line.

Measurement space clustering, Figure 7.24, does not classify the terrain to any particular degree at level two. Although symbol 1 corresponded to darker areas than those classified as 2, unlike previous examples, vegetation and bare ground were not distinguished separately. Level three showed the darker vegetation, symbol 5, to be separated from the darker toned ground, symbol 1. The greatest level at which the correlation was evident was four. At level four the very light toned loams were classified as symbol " . " and other medium toned regions with or without some slight vegetation as symbol 2.

Summarising the level four classification:

Symbol	Feature
.	Light toned areas corresponding to loams.
2	Medium toned regions of bare ground or with some vegetation cover.
5	Areas with relatively heavy vegetation cover, probably Enneapogon Polyphyllus.
1	Areas with some vegetation cover. Very similar tone on Figure 7.23 as symbol 2 regions.

The classification appeared to correspond reasonably well with Figure 7.23 except in two areas. These, the sequences from 56 - 64 and 94 - 101 were classified as symbols 1 and 5 respectively. From

the tones on Figure 7.23, points 56 - 64 would be assumed to be more similar to 94 - 101 than 10 - 17. However, examination of the true colour film showed that there were differences between the two areas such that the classification was justifiable. The region associated with mineralisation, points seven to eighteen, was classified as 75% symbol 1, and 25% symbol 2, but if symbol 1 were to have been associated with a mineralised area, other such areas would exist at 22 - 31 and 56 - 64; such a condition was not implied in the ground truth data.

The degree of correlation between the results of the image space clustering, Figure 7.25, and the photograph, Figure 7.23 was very high although, as with the measurement space results, at level two, the discrimination was between very light toned regions and all else. This was most probably due to the differences between the latter regions being greater in the other wavebands than the difference manifested in Figure 7.23.

Levels of particular interest were five and six as they indicated the degree to which the analysis could be taken yet still remain relevant.

Level 5

Symbol	Feature
1	Uniform medium toned region with little vegetation.
3	Soil similar to symbol 1 area, but with vegetation cover.
5	Very light toned areas of terrain, virtually devoid of vegetation.
6	Area of heavy vegetation cover, possibly Enneapogon Polyphyllus.
7	Very similar to symbol 5 areas. No apparent reason for differentiation until the true colour film revealed symbol 7 areas to be free from vegetation.

Level 6

As for level 5 except:

Symbol	Feature
1	Bare ground, sandy in colour.
2	Some ground as symbol 1, but with light green vegetation, probably grasses.

A more detailed classification was shown to be appropriate when the g.d. plot was studied in conjunction with the colour film. The colour film revealed the differences between the vegetation cover along the scan line. Healthy vegetation, possibly the result of high moisture levels, was seen to have been classified as symbol 4 from amongst the observations labelled as symbol 3 at levels five and six.

7.4.5 Classification of Large Scale Imagery: Figures 7.26 - 7.29

Comparison of the track, seen at data point 40 on Figure 7.27 with that shown on Figure 7.19 indicates the degree of magnification at which the area was scanned. Clumps of triodia bushes are shown in the first 20 data points of the scan, and from points 70 to 135 the dark patches of grass are clearly visible. Classification was attempted at this magnification in order to examine the effects of scale changes.

Level six of the measurement space clustering output, Figure 7.28, provided the maximum amount of information which could be related to the imagery, Figure 7.27. The results are tabulated below:-

Level 6

Symbol	Feature
1	Bare ground
2	Ground with triodia bushes

FIGURES 7.26 to 7.29 - PAGE 188 .

Figure 7.26 : Three density scans made along the transect line shown in figure 7.27.

Figure 7.27 : The area studied with the transect line delineated with arrows.

Figure 7.28 : The Group Distribution plot relating to the measurement space clustering.

Figure 7.29 : The image space clustering Group Distribution plot.

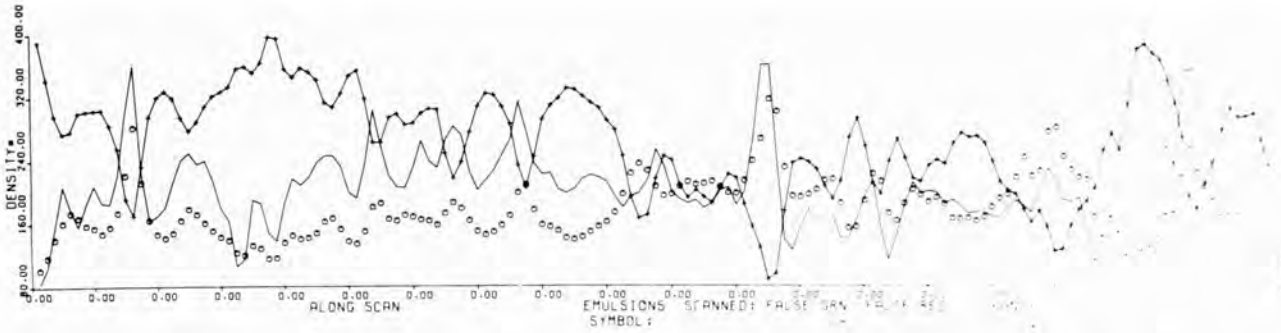

FIG. 7.26

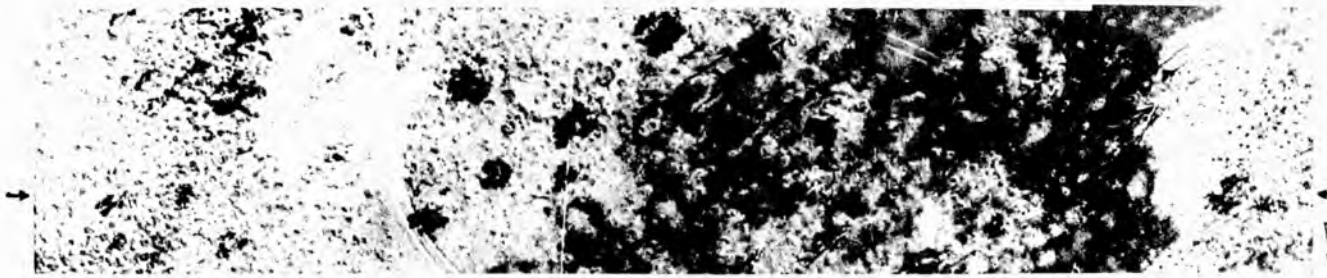

FIG. 7.27

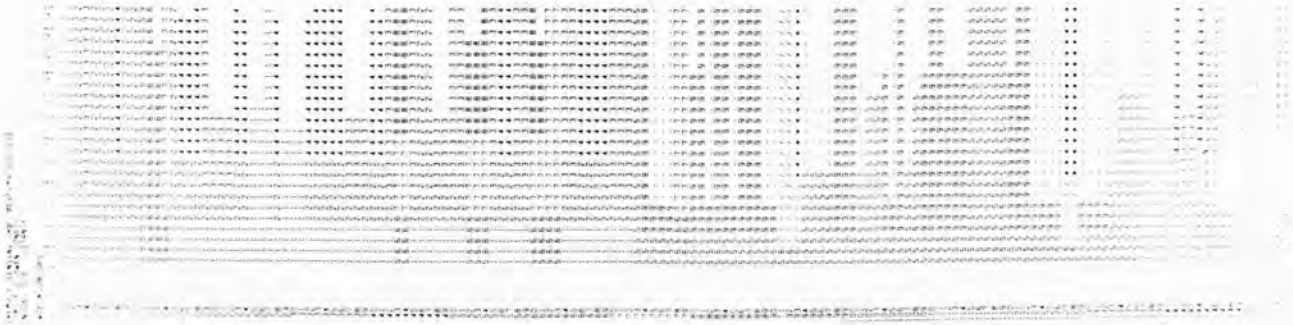

FIG. 7.28

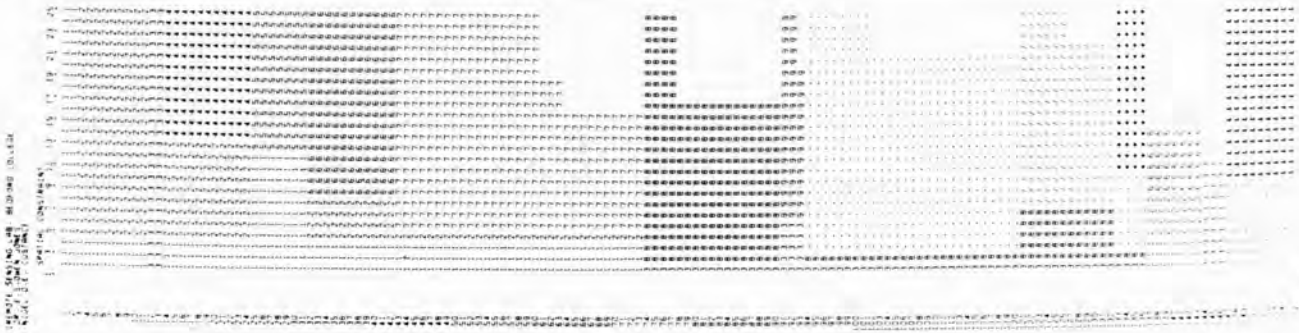

FIG. 7.29

Level 6 (Cont.)

Symbol	Feature
6	Shadows
5	Areas of mixed vegetation, triodia and dark toned grasses.
9	Predominantly grasses
/	'Noise'

The results were considered to be adequate for vegetation mapping, the reason for the improved correlation with the imagery being attributed to the smaller scale.

Figure 7.29, the g.d. plot from the image space clustering showed good agreement with Figure 7.28 up to level three. However, at greater levels the differences became appreciable and at level six the runs listed below were classified as separate entities. A tentative identification of the classes is also given.

Level 6

Data Points	Feature
42 - 73	Medium toned ground with triodia cover
74 - 90	Grass
94 - 120	As for symbol 5 above

This classification is further supported as points 121 - 132 were classified as members of the same group as points 74 - 90; a classification shown to be acceptable on Figure 7.27.

In this particular region of the terrain, and at the scale chosen for scanning the benefits or otherwise of image space clustering

were not so obviously clear in terms of classification improvements. However there was still the advantage of reduced care storage and computation time to be considered.

7.5 Conclusions as to the Usefulness of Cluster Analysis as Applied to the Areas Investigated.

The purpose of the analysis described above was to classify the terrain. However, although the computer programmes functioned correctly, it did not follow that the results were wholly satisfactory. This was because the criterion for assessing performance differed from that applied in measuring the failure or success of the mathematical manipulations. Consequently, as the object of the study was vegetation and soil mapping, the classification accuracy had to be considered in those terms.

Measurement space clustering techniques were found to provide classifications which could, typically, identify four terrain types such as different soils and/or different vegetation. Whilst this was considered reasonably satisfactory it was found that within an area which could normally be considered to be uniform by mapping criteria, the clustering often gave mixed classifications. Although these classifications were mathematically correct (i.e. all identical or nearly identical observations had identical symbols), before the output could be used for mapping, areas of homogeneous classification would be required.

One method of reducing the mixed classifications is to smooth the density scans, typically by averaging the scan over several consecutive data points. Results from such an approach showed it to be effective in reducing the mixed classifications, but unfortunately otherwise distinct boundaries between different classes were also smoothed over. A similar result was seen when the relative geographical positions of the data points were used as a measurement space vector.

Image space clustering routines were also used in an attempt to overcome mixed classifications and, although it was certain that runs of homogeneous classifications would necessarily be derived, the degree of successful correlation of the results with the observations of the areas made on the aerial photographs was encouragingly high.

The flexibility of the computer facilities and of the data storage made it possible to apply single ratio and summed ratio transforms to the data before clustering. Analysis of the output showed there to be inconclusive differences between the measurement space results and negligeable changes with image space routines.

Within the context of the study, image space clustering routines were found to provide a level of classification which would enable a satisfactory degree of vegetation and soil mapping to be carried out.

Although it has been shown theoretically that changes in the error term should provide clues as to the number of 'natural' clusters within the measurement space, in practice this was not found to be the case. The number of relevant clusters was always chosen by comparison of the g.d. plots with the aerial photographs.

7.6 Discussion of the Implications of Using Image Space Clustering Techniques

Image space clustering routines gave results more akin to those desired by mappers because of the spatial constraint placed upon the clustering procedure. Within a given region of terrain there may be, for example, three physically contiguous areas of different terrain type. Experience of working with such a state has shown the three density distributions associated with the areas to have considerable overlap. Consequently it is highly probable that members from each area can be found which have very similar positions in measurement space. Measurement space clustering encourage the merging

together of such members and, as the clustering routines encourage the formation of tight clusters, these initial members' positions in measurement space will form the cores of the final clusters. However, the 'clustering' which mapping requires is the delineation of areas rather than point-to-point associations. Consequently the restraint of allowing only adjacent points or groups of points has two obvious effects. Firstly areas will be gradually assembled as points are inevitably associated with their neighbours and, secondly, the first few points to be associated with one another will, although not being as similar to those associated by measurement space techniques, will certainly be more representative of the region of the terrain from which they emanate and thence be more representative of the desired cluster centre.

For the reasons discussed earlier, 6.11, image space clustering must be ceased before the 'relevant' clusters are forced to associate the unlike neighbours. This necessitates a decision as to the relevant number of groups within an area of terrain and a priori knowledge is therefore necessary. This slightly contradicts the earlier discussions when the advantages put forward for applying unsupervised cluster analysis techniques were that a priori knowledge was, by definition, not required. However, the a priori knowledge required is relatively small and is of a spatial nature. Typically, at the simplest level, the input required could be the size and location of an area which is considered to be uniform - e.g. a field. The changeover from image to measurement space routines could then be initiated automatically. Further inputs could be considered, each input representing a particular terrain feature. Routines would then optimise the changeover so as to delineate the features as separate entities using image space clustering and then to associate the similar features using measurement space routines.

7.7 The structure of Multi-Spectral Data

The theoretical basis on which the cluster analysis routines were based have been discussed in Chapter 6. Of particular importance was the assumption of orthogonality between measurement vectors.

Two aspects of interest arise if all or some of the vectors are not orthogonal. Firstly the mathematical justifications for applying the clustering algorithms may not be totally valid and, secondly, the number of vectors used for the analysis can be reduced mathematically by constructing a new set of vectors which are orthogonal and contain all the information present within the original data.

Cross correlation coefficients were calculated for six sets of scans; each set consisting of approximately 140 observations. The correlation coefficients are presented in Table 7.5 and have been multiplied by 100 for convenience. The distribution of most and least significant waveband correlations appears fairly randomly over the matrix but it was seen that there was a very high degree of correlation in almost all cases. The least significant correlation was found to be True Colour (Red) and Panchromatic (Green filter) whilst the highest correlation existed between True Colour (Green) and True Colour (Blue). Consequently comparisons between the same areas of terrain as recorded on the True Colour (Red Sensitive) layer and the Panchromatic (Green filter) film would reveal the greatest differences.

The different correlations between wavebands arise when different terrain types are encountered. A uniform area of terrain occupying the entire length of the scan results in absolute correlation whilst the presence of different terrain types with different spectral signatures reduces the degree of correlation. For this reason, and because of the many types of terrain encountered, the coefficients shown in Table 7.5 vary from scan to scan and no generalisations could be reliably made except that a high degree of correlation (and therefore redundant information) existed between most wavebands. Reductions in the amount of data derived from multispectral systems are of importance not only at the analysis/data processing stage but also during data transmission and for data storage. Data reductions can be achieved using several techniques, one being a principal components transform.

The application of principal components analysis to a set of observations enables a set of orthogonal vectors to be constructed from the original set. Assuming that none of the original vectors was a linear combination of any or all of the other vectors then the number of orthogonal vectors equals the number of original vectors. However, as the directions of the new vectors in measurement space have been optimised along the axes of maximum variance it has been found that a considerable proportion of the total variance (information content) will be contained in the first few vectors.

Table 7.6 shows the salient features of the results from the principal components analysis to the six data sets. In all cases the first component contained at least 60% of the total variance and was formed from the original vectors in a very similar manner. The first two components accounted for 80% of the total variance, however the second component differed in form from set to set. Similar results have been found when large data sets are examined (2) although it is considered that the information loss associated with a general transformation, rather than one appropriate to the specific area, would be a relatively small percentage.

The data sets to which the correlation and principal components analysis routines were applied were those discussed in Figures 7.10 - 7.20 together with a set containing the calibration boards. Consequently the results were typical of different types of terrain, photographic scales and targets. The high degree of correlation between emulsion layers suggests that the waveband sensitivities of the layers were not optimised with respect to the terrain whilst the principal components analysis results implied that considerable reductions in data flow could be achieved without loss of information.

7.8 The Processing of Large Volumes of Data: Projected Rationale

In February 1973 the Joyce Loebl modifications to the microdensitometer were completed. However, malfunctioning of the instrument - which

TABLE 7.5 SHOWING THE SIX SETS OF CROSS-CORRELATION COEFFICIENTS RELATING TO THE DENSITIES DERIVED FROM EACH EMULSION LAYER SCANNED.

Emulsion Scanned.	FCG	FCB	FCR	TCG	TCB	TCR	PG
FCB	84 79 33 91 87 92						
FCR	77 81 33 83 64 77	78 78 77 75 56 81					
TCG	71 59 41 77 42 83	65 50 86 74 44 87	53 36 62 65 22 86				
TCB	62 55 42 76 78 83	58 39 77 76 68 80	43 27 56 60 50 74	82 91 87 97 22 90			
TCR	50 24 41 81 89 89	36 10 77 78 75 89	33 9 66 73 62 78	41 44 85 97 30 85	41 43 83 93 86 82		
PG	73 64 40 89 90 76	83 61 74 86 90 82	81 49 66 64 64 80	51 66 80 67 36 86	43 65 83 70 77 80	30 21 84 68 85 74	
PY	88 84 41 88 85 81	88 79 54 76 75 77	79 71 45 69 64 71	68 72 57 57 28 81	57 65 55 58 78 87	46 29 65 60 88 80	88 72 54 85 89 84

TABLE 7.6 SHOWING THE RELATIVE EIGEN-VECTORS CORRESPONDING TO THE DIFFERENT EMULSION LAYERS SCANNED TOGETHER WITH THE CUMULATIVE VARIANCE ASSOCIATED WITH THE FIRST THREE COMPONENTS DERIVED USING PRINCIPAL COMPONENTS ANALYSIS.

Eigen-vector No.	1						2						3					
Set No.	1	2	3	4	5	6	1	2	3	4	5	6	1	2	3	4	5	6
Emulsion Layer.																		
False colour green	13	40	36	40	39	38	-76	6	35	-16	8	-24	-60	1	33	-20	26	-3
False colour blue	39	37	36	36	36	37	24	16	49	-34	-1	-13	-8	10	4	-15	55	11
False colour red	31	29	34	34	16	32	39	-39	8	-44	96	-21	-24	78	-64	-29	-8	-83
True colour green	42	17	37	39	38	36	3	89	-9	33	-8	47	0	21	-25	26	-33	2
True colour blue	41	36	35	33	36	35	-6	-13	-34	43	21	45	-7	-53	37	28	-42	19
True colour red	41	39	37	10	37	37	-1	-9	35	60	-13	38	14	-26	16	-75	35	-15
Panchromatic(Green)	-40	-40	-35	-38	-37	-35	-4	-1	39	-8	-2	30	7	-2	37	-37	46	-47
Panchromatic(yellow)	-25	-39	-34	-42	-39	-33	46	11	50	-6	7	47	-74	9	-35	9	-10	-14
Cumulative Variance (x100)	62	72	84	61	81	78	76	84	89	81	92	88	84	91	94	89	97	94

persisted until December 1973 - prevented accurate automatic scanning of images. Consequently the computer generated replays, Figures 7.31, 7.32 and 7.33 of the area shown in Figure 7.30 were such that registration was not practicable and the investigations of the proposed clustering routines, 6.11, could not be carried out. However the replays do serve to illustrate some of the problems discussed earlier and also show the output medium (computer microfilm plotter) that results would have been presented upon.

The replays - which were such as to optimise the available density range using an equi-density quantization routine - show the differences between layers and the loss of spatial information encountered when the image was sampled with a 100 x 100 matrix. Small scale features, such as the two vertical (picture plane) drainage channels in, and to the left of centre as well as the vegetation pattern running horizontally can be detected. However, areas of terrain which could be relatively easily delineated as being uniform on Figure 7.30 were by no means obvious on the replays although the areas themselves - e.g. the horizontal dark toned vegetation band - are large compared to the size of the computer picture point. Image space clustering routines were found to be more appropriate in such situations and it was envisaged that acceptable results would be obtained.

Data reduction studies were considered to be necessary if the processing was to become more rapid. One particular approach considered was to apply factor analysis routines to areas of known terrain types. This approach, in contrast with principal components analysis, enables the regions of terrain considered relevant to be used to derive the new vectors.

7.9 Clustering Routines used in Conjunction with 'Look-up' Classifiers

An alternative which would reduce the computation time associated with the classification is similar to a supervised learning routine.

FIGURES 7.30 to 7.33 - Page 199

Figure 7.30 : Panchromatic photograph of the Dugald River Lode area.

Figure 7.31 : Computer generated reconstruction of density scanned image. False Colour Red layer.

Figure 7.32 : Computer generated replay derived afer scanning the Blue dye layer of the False Colour film.

Figure 7.33 : Computer generated replay derived after scanning the Panchromatic film (Yellow filter).

In all the replays the area concerned is that shown in Figure 7.30. Figure 7.33 was derived after scanning the negative film.

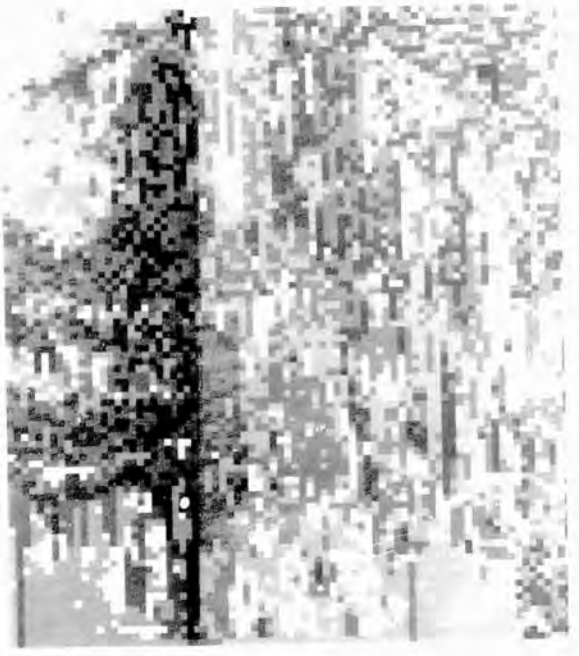

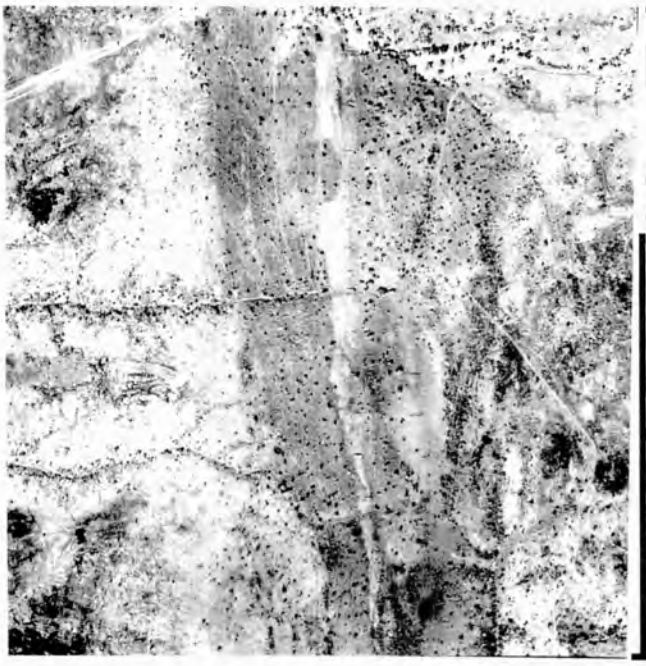

The particular clustering routines, having been applied to relatively small and representative areas of the terrain, would enable the densities associated with each cluster to be determined. Their mean densities, together with their associated deviations could then be used in a look-up mode to classify the remainder of the image. The results of the classification could then be displayed using the replay programme used to produce Figures 7.31 - 7.33 where the particular clusters can be represented by a specific density, or colour by means of multiple exposures on to colour film. However, as with measurement space clustering, the distribution of groups is unlikely to result in homogeneous regions akin to thematic maps. Consequently, although a rapid classification, possibly using analogue circuitry, becomes available some smoothing of the classification before display would be necessary.

7.10 Classification Using Non-Spectral Features

Within the current project, several different features could have been used, either independently or in conjunction with the spectral content of the terrain to improve the classification. Two particular features already mentioned were the presence of trees and the spatial information contained within the imagery.

Trees have been shown to occur only in particular regions where the terrain was conducive to their growth. The detection of the tree canopy was found to be more easily performed on the false colour imagery where the strong infra-red reflection dominated that from all other areas of the terrain. However, a simpler method, applicable to all the photographic imagery, was to detect first the presence of shadows, which, because of the physical nature of the environment, were almost always the shadows from trees. In order to convert the binary presence/absence of trees into a meaningful measurement vector it would be necessary to associate a 'tree' score with every observation in the picture plane. One method of scoring considered was to use the number of trees within a given distance - probably

Manhattan - from the observation concerned. The score would then be treated in the same manner as the spectral features.

Spatial features within the context of picture processing tend to be associated with periodic structures. Sand dunes, waves on water surfaces, plantations and geological formations are examples of periodic structures whilst different amounts of bushes, randomly distributed, represent different textures. Information relating to spatial features has been derived by other researchers using Fast Fourier and Hadamard Transforms which effectively transform the image into the frequency domain.

Clearly defined periodic structure was seen when tree plantations were scanned but too little work was carried out using F.F.Ts. to draw conclusions as to their use in near spatially random environments.

7.11 Overall Conclusions made on the Analysis of the Photographic Imagery.

The results presented in this Chapter demonstrated the following:

(i) Measurement space clustering routines were capable of classifying multi-spectral data to a limited extent.

(ii) A hybrid image and measurement space clustering provided classifications which were more highly correlated with the thematic maps produced and used by earth scientists.

(iii) Corrections, transforms and iterative relocation clustering routines were found to provide only minor changes in the classification performance.

(iv) A considerable proportion of redundant data was gathered using the multi-spectral camera array.

(v) Bulk data processing was envisaged using:
    (a) Hybrid image and measurement space techniques
    (b) Spectral parameters derived from small area classifications, although this would require some spatial filtering.

7.12 References

(1) KODAK : Kodak Wratten Filters, 4th. edition, 1969.

(2) READY, P : IEEE Trans. Comm., COM-21, No.10,1973.

8 TERRAIN CLASSIFICATION USING PHOTOGRAPHIC IMAGERY IN THE VISIBLE AND NEAR INFRA-RED SPECTRUM TOGETHER WITH IMAGERY FROM THE THERMAL INFRA-RED SPECTRUM: CONCLUSIONS

In view of the pseudo-random nature of the environment which was studied and on which classification was attempted the results were regarded as encouraging.

Terrain classification using multi-spectral camera arrays and standard photo-interpretation techniques is already a well practised art. Consequently the aim of the study was biased towards machine classification techniques. It has been shown that without the use of spatial information the classification of the terrain in Western Queensland lacked the uniformity of delineations between terrain types generally associated with the thematic maps used by earth scientists.

The techniques developed were considered to be appropriate for the analysis of small areas, but the processing of bulk data would necessitate a modified approach in order that the time required for computation of the results would not become inordinately large.

Imagery derived from the infra-red linescanner related to the thermal and emissive properties of the terrain. An unfortunate malfunction of the equipment resulted in degraded imagery being produced. However it became apparent that the information derived from this waveband was related to small scale features, typically of a size useful for the geological mapping of structure. The effects of solar radiation on the terrain made quantitative assessment of the imagery exceedingly difficult although it was felt that, in view of the size and scale of the useful features seen on the imagery, direct visual interpretation was the optimum form of processing.

ACKNOWLEDGEMENTS

Very grateful thanks for their advice and help are given to the technicians and staff of the Physics Department at Bedford College who created a stimulating environment in which to work.

Particular thanks go to Dr. Stuart Owen Jones whose supervision enabled the research to be both enjoyable and meaningful.

A.K.P. Thankyou.

APPENDIX A

The report contained in Appendix A was presented to the Forestry Commission at the conclusion of the project.

THE DETECTION OF PHOSPHATE DEFICIENCIES AND TOXICITIES IN SITKA-SPRUCE TRANSPLANTS USING NARROW-BAND PHOTOGRAPHY

By N.D.E. Custance and Dr. E.S. Owen Jones

Phosphate deficiencies and toxicities in Sitka Spruce tend to be different from those of other common elements as there is no noticeable associated change in foliar colour (1). Work, primarily in the U.S.A. on the light reflected by foliage has shown that some stress conditions are manifested by changes in a relatively narrow part of the visible or near infra-red part of the spectrum e.g. the latter is associated with the inner structure of foliage.

The authors' interests are in the factors affecting the reflectance of light by foliage, and a co-operative project using a control at Wareham and a test site at Headley Nursery was carried out in 1972 (June - October).

Six plots, each containing 30 Sitka Spruce transplants and with phosphate doses of 0, 1, 2, 5, 9, 18 gms/sq. yd. were set out in May. These were re-photographed from the ground at monthly intervals until October, when a 40 feet tower was used to obtain vertical photographs. The photographs were taken using six narrow band (20 nm) filters in the visible and near infra-red part of the spectrum. The vertical photographs proved the most rewarding and are discussed below.

In the visible spectrum two of the filters revealed subtle tonal differences between plots which correlated with the phosphate toxicities found later by foliar analysis. An increase in the effective horizontal canopy area with increasing levels of phosphate treatment was seen clearly on the infra-red photographs where the vegetation was in high contrast with the soil backbround.

The work is considered to have been sufficiently promising that a more sophisticated experiment with phosphate levels ranging from

sub-optimum to toxic is being proposed for the coming year (1973). The problems of image fall-off due to the thick filters used and that of varying incident light intensity will be further investigated as will the use of a Spectro-Radiometer for initial small-scale scanning of the canopy's reflective spectrum for induced effects. In the meantime it is hoped to incorporate in an existing aerial photographic sortie a set of narrow-band photographs over an area of known significant phosphate level differences.

Our thanks go to Dr. G. Mayhead of the Forestry Commission for his assistance on the Commission's behalf.

(1) Forestry Commission Bulletin No. 37 p.180

APPENDIX B

The paper reproduced in Appendix B was presented to the British Interplanetary Society at the Symposium on Earth Observation Satellites, 10-12 April, 1973.

Journal of the British Interplanetary Society, Vol. 27, pp. 18-22, 1974.

DIGITISED ANALYSIS OF SKYLARK ROCKET IMAGERY

E. S. OWEN JONES and N. D. E. CUSTANCE
Physics Department, Bedford College, Regent's Park, London, N.W.1., England.

Cluster analysis techniques are applied to rocket imagery of a cultivated area in the Ceduna region of Australia. Considerable improvements in the classification are obtained by the implementation of a hybrid image space/measurement space clustering routine. The technique is seen as a means of creating discriminant criteria for bulk image analysis.

1. INTRODUCTION

IN THIS PAPER we consider the application of cluster analysis techniques to the Skylark rocket imagery obtained over Woomera in March 1972. The area chosen for study is in the Ceduna region where the principal features are cultivated fields. Cluster analysis is an unsupervised learning technique and therefore requires no *a priori* knowledge of the targets between which discrimination is sought – although the overall performance can obviously only be verified by correlation of computed results with ground truth data. The study was relatively short and the area analysed small, as its purpose was to investigate techniques appropriate to an extensive terrain analysis programme currently under development.

2. METHODS OF ANALYSIS

Current machine terrain classification processes depend in the main on supervised learning techniques. These require that training areas be supplied to the computer so as to establish discriminate criteria which classify unknown data. Such a process can be time consuming with digital machines but its main drawback is that the final result is a function of the training sets used whereas the results from cluster analysis (unsupervised learning) are related solely to the raw data input.

Three principal forms of cluster analysis were considered appropriate to the data used; Hierarchical Fusion, Iterative Relocation and Division. Of these only the first two mentioned were applied to the rocket imagery with greater emphasis being placed on the fusion method. Considerable improvements in computer time and results were obtained by imposing spatial criteria on the fusion routine. Iterative Relocation gave similar results to Hierarchical Fusion (without the spatial criteria) and is not discussed in detail.

The area chosen for examination is situated in the cultivated Ceduna region, Fig. 1a and is shown in detail in Fig. 1b, Fig. 1c being a conventional aerial photo taken from 2000 ft. The task for the analyst can be broken down into two parts:

(i) Delineation of field boundaries.
(ii) Identification of field types.

The photographic systems employed in the Skylark SL 1081 package, discussed elsewhere [1] resulted in three photographs of the region each taken through

Fig. 1a. Part of frame 46, SL 1081 imagery showing the Ceduna region at 1:2,000,000 scale.

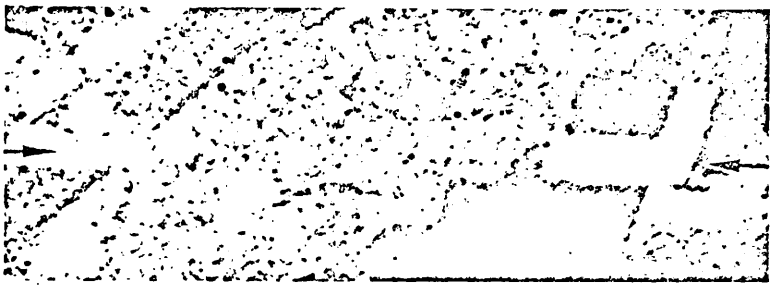

Fig. 1b. Enlargement of the area within the box in Fig. 1a. The start and finish of the scanned line are indicated by arrows.

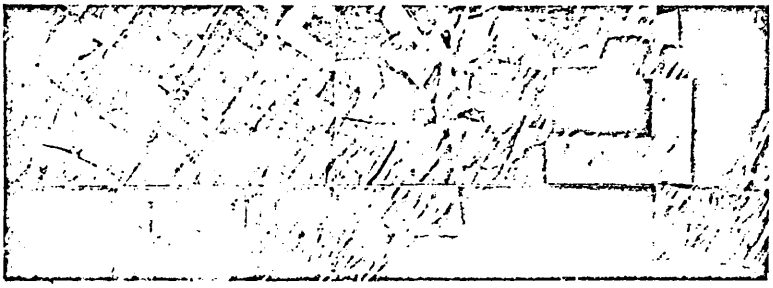

Fig. 1c. Conventional aerial photograph of approximately the same area and scale as Fig. 1b.

a different filter – Frames 45 (Red) 46 (Yellow) and 47 (Green). A small area was chosen in which The University of Reading field party had carried out ground surveys and a single line scan was made through this area on each frame with a Joyce Loebl Microdensitometer. This resulted in three digitised density scans Fig. 2, differing from each other because of the differing reflectance spectra from the fields under examination. The spot size of the light beam in the microdensitometer, which determined the area sampled to give a single density reading, was approximately 40 x 40 microns, equivalent to 80 x 80 metres on the ground.

Examination of the scans showed that apart from the start of the scan where there was bare ground, no other obvious field boundaries could be located. Their inferred location, marked with asterisks, was obtained by extra-polation from the 1:20,000 photograph Fig. 1c.

After calibration and scaling the data was analysed using Ward's Error Sum of Squares Clustering techniques. The three variables represented by the optical densities of the three spectral bands are treated as orthogonal vectors. Each particular element on the ground will have three densities associated with it and thus has a particular position in three dimensional (measurement) space. Similar ground elements – by intuitive definition – will have similar reflectances and thus will

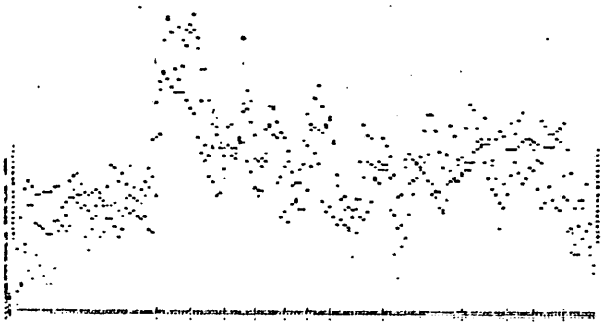

Fig. 2. The three microdensitometer scans along the line delineated in Fig. 1b corresponding to the Red (1), Yellow (2) and Green (3) bands. The asterisks along the abscissa denote the field boundaries determined from Fig. 1c.

be near each other in measurement space. Cluster analysis is used to search through the measurement space and merges together those points which are not only close together but also form a tight cluster. As the clustering is hierarchical, merging of the points, or groups of points, is an irrevocable step and points cannot be transferred to a different group at a later stage, a restriction which is not imposed by Iterative Relocation routines. The process continues merging together points or groups of points until finally all points are a member of the one same group, but the results at any level of grouping can be examined. The relevant level of grouping to be used is determined by ground truth considerations.

3. DISCUSSION OF RESULTS

The results of a given analysis are presented on Group Distribution (G.D.) plots (Figs. 3, 4). The 'X' axis represents distance along the scanned line whilst increas-

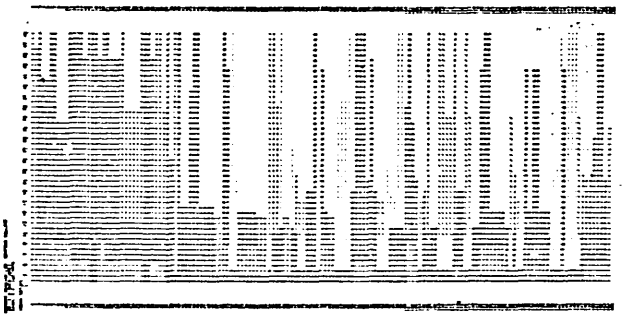

Fig. 3. The Group Distribution Plot resulting from measurement space clustering. The abscissa represents position along the scan line and the ordinate the level of grouping. The lowest level of the block of characters corresponds to two groups, the next line up to three groups, the next to four, etc.

ing levels of grouping are in the 'Y' direction. Each ground element has a symbol associated with it, corresponding to the group to which it is allocated. Thus, the lowest line, corresponding to two groups, has symbols 1 and 5. With the aid of such plots, the interplay between distribution and the choice of levels is readily assimilated, and its significance understood. For example, level two shows the distribution of bare ground, Symbol 1, and all other ground, Symbol 5; at level 3,

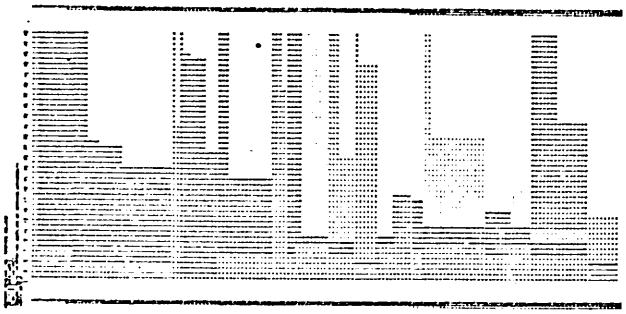

Fig. 4. The Group Distribution Plot resulting from hybrid image/measurement space clustering.

Symbol 5 is subdivided into Symbol 5 and Symbol 8.

The results of Fig. 3 were encouraging, some field boundaries being located, but two problems were seen on the G.D. plots. The first was that the level of grouping which gave good discrimination for some fields was too large or too small for others. The second problem now arises such that when a certain level of grouping was chosen, some fields would consist of a heterogeneous collection of groups. The reason for this is thought to be due to the different within-field and between-field variances and their associated effects on the merging procedures. It was implied earlier that the criterion for points or groups of points to be merged together is a function based on two measurements; the distance in measurement space between them, and the tightness of the clusters formed by the merger (the within-group variance). The function of these two parameters is the merging error. For three fields, A, B, C, with associated within-field variances V_A, V_B, V_C and between-field distances S_{AB}, S_{BC}, S_{AC} the merging errors M_{xy} where

$$M_{xy} = f(V_x, V_x, S_{xy})$$

can be such that

$$M_{A_iA_j} > M_{BC}$$

where i and j are points or groups of points within field A but not of the same cluster. Thus B and C merge before the ith and jth members of field A do, e.g., a field of scrub (A) could have a greater merging error associated with its own points than that between a field of grass (B) and a fallow field (C). To overcome this problem spatial constraints and an iterative clustering routine were tried.

Iterative Relocation is a method of clustering which allows points to change groups. Thus, after a merging of groups, all the points in all the groups can be examined and moved to another group if the individual's merging error would be reduced. This method was used but the results, although slightly different, did not warrant further investigation.

An alternative form of analysis is to cluster together points in image space rather than measurement space. In the present case this meant imposing the restraint whereby merging would only be allowed for points or groups of points that were, or had members, which were adjacent, e.g., for points numbered sequentially along the scan;

41 merging with 43; forbidden
41 merging with 42; allowed
41, 42 merging with 43; allowed

It was hoped that such clustering would overcome the previous problems by encouraging the fields to form as separate entities.

The results of this spatial constraint applied to the Hierarchical Fusion routine were to reduce the computing time by a factor of 4 and to build up homogeneous groups very rapidly (Fig. 4). The disadvantage came when, having grouped the points into fields, the fields were irrespectively merged with their neighbours. This problem was circumvented by releasing the spatial constraint at a level of ~ 20 groups and then allowing hierarchical clustering to continue. Thus similar fields were clustered together on the basis solely of their merging error in measurement space.

4. CONCLUSION

This hybrid clustering will be used as an initial means for determining the combinations of densities required for discriminating between areas of interest on small scale imagery. These densities could then be used in conjunction with an additive viewer where the optimum filters and light levels would be determined automatically rather than by trial and error, whilst the most effective method will be to slice out the appropriate densities from each film and then to recombine them via filters on to colour film, giving a terrain classification-by-colour map.

REFERENCE

1. R. A. G. Savigear, J. R. Hardy, C. W. Mitchell, R. B. Ridgway, A. J. Parsons, Rocket Photography for Earth Resources Surveys.

(Presented at the Symposium of the British Interplanetary Society on 'Earth Observation Satellites' held at University College London, 10-12 April 1973)

T H E E N D .